UMI Number: 9525743

UMI

300 North Zeeb Road
Ann Arbor, MI 48103

ABSTRACT

DESIGN AND MICRO-FABRICATION OF TANTALUM SILICIDE CANTILEVER BEAM THRESHOLD ACCELEROMETERS

by
Chang Joo Kim

Microfabricated threshold accelerometers were successfully designed and fabricated following a careful analysis of the electrical, mechanical, and fabrication issues inherent to micron-sized accelerometers. A uniform cantilever beam was chosen because of the simplicity of design and fabrication. New models for the electrostatic force exerted on the cantilever beam were developed and calculations were made that accurately predicted the electrical characteristics of the accelerometer. The calculations also provided design guidelines for optimizing the accelerometer dimensions. Computer simulation demonstrated that the error of the electrostatic force, calculated using the most accurate model, was within 2% of the actual force which was obtained by integrating the closed formula, through the bent beam curvature, for device parameters designed to detect an acceleration of 50 g. Conversely, it was shown that the widely used conventional parallel plate model had an error of approximately 90%.

Novel surface micromachining process steps were successfully developed to fabricate the cantilever beam accelerometers. Sputter deposited tantalum silicide and commercially available spin-on-glass were used as a structural layer and a sacrificial layer, respectively. The dependence of resistivity, crystalline structure, Young's modulus, and hardness of the tantalum silicide films on the annealing temperatures were measured. These results were employed to design accelerometers that were successfully operated. Excluding the metallization steps, only two masks and four photolithography steps were required. However, both positive and negative photoresists had to be utilized. NJIT's standard

photolithography steps were used for positive photoresist; however for the negative photoresist a specially developed multi-puddle process was used to obtain 4 micron resolution.

Electrostatic attraction tests, of accelerometers, were performed using the Keithley current-voltage measurement system. These tests used deflection voltages ranging from 2.2 to 37.0 volts, corresponding to threshold acceleration levels from 580 to 18,500 g. Nearly 70 percent of the threshold voltage results fell within the expected error limits set by the accuracy of the device dimensions when processing tolerances were taken into account including the thickness variation caused by 8% uncertainty in the buffered HF etch rate of tantalum silicide. Some accelerometers were closed and opened 3 times without failure. The accelerometers tended to break after 3 times of operation and this was attributed to the welding of contacts. Centrifuge acceleration tests of accelerometers were carried out in a specially designed centrifuge in an acceleration range of 282 to 11,200 g. Nearly 80 percent of the threshold acceleration results fell within the expected error limits set by the accuracy of the device dimensions when processing tolerances were taken into account.

DESIGN AND MICRO-FABRICATION OF TANTALUM SILICIDE CANTILEVER BEAM THRESHOLD ACCELEROMETER

by
Chang Joo Kim

A Dissertation
Submitted to the Faculty of
New Jersey Institute of Technology
in Partial Fulfillment of the Requirements for the Degree of
Doctor of Philosophy

Department of Electrical and Computer Engineering

January 1995

APPROVAL PAGE

DESIGN AND MICRO-FABRICATION OF TANTALUM SILICIDE CANTILEVER BEAM THRESHOLD ACCELEROMETERS

Chang Joo Kim

Dr. Kenneth Sohn, Dissertation Advisor — Date
Professor and Acting Chairman of Electrical and Computer Engineering, NJIT

Dr. Roy Cornely, Committee Member — Date
Professor of Electrical and Computer Engineering, NJIT

Dr. James Grow, Committee Member — Date
Associate Professor of Chemistry, NJIT

Dr. Durgamadhab Misra, Committee Member — Date
Associate Professor of Electrical and Computer Engineering, NJIT

Dr. Marek Sosnowski, Committee Member — Date
Associate Professor of Electrical and Computer Engineering, NJIT

BIOGRAPHICAL SKETCH

Author: Chang Joo Kim

Degree: Doctor of Philosophy in Electrical Engineering

Date: January 1995

Undergraduate and Graduate Education:

- Doctor of Philosophy in Electrical Engineering,
  New Jersey Institute of Technology, Newark, NJ, 1995
- Master of Science in Electrical Engineering,
  New Jersey Institute of Technology, Newark, NJ, 1987
- Bachelor of Science in Electrical Engineering,
  Seoul National University, Seoul, Korea, 1975

Major: Electrical Engineering

Presentation and Publication:

Kim, C. J., K. S. Sohn. "Micro Electromechanical Properties of Tantalum Silicide Thin Films." 1995 Spring Meeting of Materials Research Society, San Francisco, CA. April 17-21, 1995.

Kim, C. J., K. S. Sohn. "Electrical and Mechanical Properties of Sputter Deposited Tantalum Silicide Thin Films." 187th Society Meeting of Electrochemical Society. Reno, Nevada, May 21-26, 1995.

Kim, C. J., and K. S. Sohn. "An Axial Gap Micromotor with Electrostatic Levitation." Symposium of the Advanced Technology Center for Surface Engineered Materials (ATCSEM), November, 25, 1991.

BIOGRAPHICAL SKETCH
(Continued)

M. Singh, and C. J. Kim. "Characterization and Optimization of of an NMOS Sense Amplifier" Proceedings of the 31st Midwest Symposium on Circuits and Systems with Coorperation of IEEE Circuits and System Society., St. Louis, Missouri, August 9-12, 1988.

Kim, C. J., and M. Singh. "Comparative Simulation Studies on Two Sense Amplifier Configurations." Proceedings of the 30th Midwest Symposium on Circuits and Systems with Coorperation of IEEE Circuits and System Society., Syracuse, New York, August 17-18, 1987.

This dissertation is dedicated
to my parents and to my family, Hagboon, Jihyun, and Daehyun.

ACKNOWLEDGMENT

The author wishes to express his sincerest appreciation to his advisor, Professor Kenneth S. Sohn, for his invaluable encouragement during the preparation of this dissertation and for allowing him to work freely in the Lab trying out new ideas. His consistent guidance and financial support made it possible for the author to complete this work.

Special thanks to Professors Roy Cornely, James Grow, Durga Misra, and Marek Sosnowski for serving as members of committee.

The author appreciates the timely help and valuable suggestions from the NJIT's Microelectronics Research Center (NJIT MRC) members, including: Mr. Michael Grieco, Mr. Ken O'Brien and Mr. John Koons.

The author is further indebted to Professor Durga Misra for masks to fabricate devices with, and to Professor James Grow for XRD analysis, Nanoindenter analysis, and SEM measurements.

The author also wishes to thank Professor N. M. Ravindra for his help in I-V measurement, to Mr. Robert Okojie for the wafer dicing, to Mr. Ted Park for the wire bonding and packaging, and to Mr. Vitaly Sigal and Dr. Jan Opyrchal for their cooperation during the SEM setup.

Additional thanks go to my colleagues, Mr. Suk Kim, Dr. Won Rim, Dr. Hyun Kim, who have provided their sharing of helpful opinions.

And finally, a thank you to Mr. Tony Lambiase for the editing the manuscript.

TABLE OF CONTENTS

TABLE OF CONTENTS
(Continued)

LIST OF TABLES

LIST OF TABLES
(Continued)

LIST OF FIGURES

LIST OF FIGURES
(Continued)

Figure **Page**

LIST OF FIGURES
(Continued)

Figure **Page**

LIST OF FIGURES
(Continued)

Figure **Page**

CHAPTER 1

INTRODUCTION

Silicon micromachining technology, during the past decade, has allowed the development of microfabricated sensors (microsensors) for a variety of physical and chemical quantities [1, 2, 3]. Many of these microsensors rely on micromechanical structures fabricated by the selective etching of a silicon substrate [1,4] or deposited thin films [5,6]. These special micromachining processes have been merged with modified integrated circuit processes to fabricate smart sensors incorporating on chip readout and signal processing circuitry [7,8,9]. Many high performance sensors such as pressure sensors [10,11,12] and analog accelerometers [9,13,14,15] have been reported on and are commercially available [16,17]. However, there has been very little published literature on threshold accelerometers [18,19].

This thesis presents processing techniques and results, from the design and fabrication of cantilever beam threshold type accelerometers, using surface micromachining technology. Sputter deposited tantalum silicide ($TaSi_2$) is used as beam structural layers as well as contacting electrodes. There were several reasons why tantalum silicide was chosen for this work. First, it is a low resistive material compared to polysilicon (approximately an order of magnitude lower). Second, it has a very high electromigration activation energy, which is 1.7 eV [21] (this is almost three times higher than aluminum of which electromigration activation energy is about 0.6 eV), and this eliminates the reliability problem caused by electromigration found with metals such as aluminum, silver, and gold. Third, tantalum silicide is compatible with standard IC processing techniques. In addition, the microhardness of $TaSi_2$ is significantly higher than that for many other silicides. However, since tantalum silicide is liable to attack by HF, it is necessary to use a sacrificial layer whose etch rate is faster than low temperature oxide

(LTO). By using spin-on glass (SOG), the release etch selectivity of the sacrificial layer to the structural layer was improved more than three times. However, there was a problem associated with SOG such that the maximum thickness for a single coating is typically less than 1 μm. But by using several layers of SOG spun on sequentially, the thickness was increased to the desired value.

In 1972, Frobenius et al. [18] described a threshold accelerometer made from an all metal cantilever type micro electromechanical switch. The cantilever beams were fabricated out of electroplated gold and a maximum threshold level of 8000g was measured by a centrifuge acceleration test. In 1987, Harry Diamond Laboratories (HDL) [19] conducted a review of three different threshold accelerometers fabricated by Honeywell, Motorola and HDL. The Honeywell threshold accelerometer consisted of an along-the-length metallization silicon beam with added mass at the tip of the beam. The Motorola accelerometer utilized a silicon dioxide beam with a gull-wing contact at the tip of the beam for a two-point contact switch. The third device, made by HDL, consisted of a metal tri-layer of nickel-gold-nickel. In 1991, Loke et al. [20] described a threshold accelerometer made of a silicon dioxide cantilever beam with a metal line (gold with chrome as an intermediate layer) running along its length. Under an applied acceleration, the beam deflected upward across a gap and made contact with a second electrode, thus closing a switch.

Chapter 2 describes background on micro electromechanical systems (MEMS). The properties of silicon, as a micromechanical material, are measured and various micromechanical sensors and actuators, which have been reported, are described. Several processing technologies associated with an analog type accelerometer and their advantages and disadvantages are also described. Finally, the background and the advantages of cantilever beam threshold type accelerometers are discussed.

Chapter 3 explains the principle of operation of the cantilever beam threshold type accelerometers, including a derivation of the beam bending equation and the maximum

deflection of the cantilever beam. Electrostatic analysis of the beam is discussed to understand the beam bending characteristics when a voltage is applied between the two electrodes of the accelerometer. Finally, threshold acceleration analysis is done to find the formula for the threshold acceleration by which the beam snaps shut when both a voltage and an acceleration are applied to the accelerometer.

Chapter 4 presents new models that were proposed in this work. These models improve the precision of the electrostatic force calculation. It is assumed in the conventional parallel plate model that the entire beam is moving through the distance of maximum deflection which occurred at the free end tip of the beam (see the beam A'C in Fig. 4.1). The reason, why this model is not suitable for the cantilever beam accelerometer, is described. In section 4.1, a triangle model is introduced. This model assumes that the beam bends not catenary but straight from the fixed end to the free end of the beam. In section 4.2, a more precise model, called a two point piecewise linear model, is suggested. These two models are compared to the parallel plate model and to the actual electrostatic force calculated by integrating the differential electrostatic force through the catenarilly bent beam. A generalized N-point piecewise linear model is also analyzed in this section followed by a threshold acceleration analysis of the triangle model in section 4.3.

Chapter 5 presents the concepts associated with the cantilever beam threshold type accelerometer design. Section 5.1 describes the advantage of the uniform cantilever beam over the double-ended bridge type or weighted cantilever beam. Section 5.2 considers the effects of the accelerometer dimension on the threshold acceleration and device durability. Section 5.3 describes the surface micromachining technique by which the accelerometers in this research have been fabricated. The two primary techniques, surface micromachining and bulk micromachining, are briefly compared and the reason why tantalum silicide and spin-on-glass (SOG) were chosen is explained.

Chapter 6 explains tantalum silicide as a micromechanical material in this work. Section 6.1 describes an overview of metal silicides including the reason why the metal silicides have been getting attention by scientists for both VLSI and micromechanical applications. Section 6.2 illustrates the preparation and annealing condition of the tantalum silicide films which were used to examine the electrical and mechanical properties. Section 6.3 presents the properties of tantalum silicide as a micromechanical material. The results of the investigating resistivity versus annealing temperature are presented. The results of the dependence of the crystalline structure of tantalum silicide on annealing temperature are also presented and discussed. The measured values for Young's modulus and microhardness of the sputter deposited tantalum silicide are also presented.

In chapter 7, the fabrication process developed for making a robust cantilever beam threshold type accelerometer is described in detail. Practical issues that had to be considered are discussed. All of the fabrication work was performed at the NJIT Microelectronics Research Center (NJIT MRC) except wafer dicing, wire bonding and packaging. A detailed process sequence is illustrated in Appendix A.

Chapter 8 describes the measured operational characteristics for the tantalum silicide cantilever beam accelerometer, including the electrostatic attraction test and the centrifuge acceleration test. The experimental apparatus for both tests are also described. Comparisons between experimental data and theoretical data (based on the triangle model with the processing tolerances taken into account) for both electrostatic attraction test and centrifuge acceleration test are presented.

Finally, chapter 9 gives the summary and conclusion of the thesis.

CHAPTER 2

BACKGROUND OF MICRO ELECTROMECHANICAL SYSTEM

2.1 Properties of Silicon as a Micromechanical Material

Single crystal silicon is increasingly being employed in a variety of new commercial products not because of its well-established electronic properties, but rather because of its excellent mechanical properties. Micromechanics as a silicon-based device technology was actually initiated by H.C. Nathanson et. al [2] at Westinghouse Research Laboratories in 1965 when he and R.A. Wickstrom introduced the resonant gate transistor (RGT). This device consisted of a plated-metal cantilever beam, suspended over the channel region of an MOS transistor. It was essentially an electrostatically excited tuning fork employing field effect transistor readout. They showed that this device permitted high-Q frequency selection to be incorporated into silicon integrated circuits.

The basis of micromechanics is that silicon, in conjunction with its conventional role as an electronic material, and taking advantage of an already advanced microfabrication technology, can also be exploited as a high precision high-strength mechanical material. This is especially applicable wherever miniaturized mechanical devices and components must be integrated or interfaced with electronics. Any consideration of mechanical devices made from silicon must certainly take into account the mechanical behavior and properties of single-crystal silicon (SCS). Table 2.1 presents a comparative list of its mechanical characteristics with other materials. Although SCS is a brittle material, yielding catastrophically (not unlike most oxide-based glasses) rather than deforming plastically (like most metals), it certainly is not as fragile as is often believed. The Young's modulus of silicon (1.9×10^{11} Pa or 27×10^{6} psi) [22], for example, has a value approaching that of stainless steel, nickel, and well above that of quartz and most other borosilicate, soda-lime, and lead-alkali silicate glasses [23]. The hardness of silicon (850) is close to quartz, just

Table 2.1 Mechanical characteristics of silicon compared to other materials [1]

	Yield Strength (10^9 Pa)	Knoop Hardness (kg/mm^2)	Young's Modulus (10^{11} Pa)	Density (gr/cm^3)	Thermal Conductiviy (W/cm°C)	Thermal Expansion (10^{-6}/°C)
Diamond	53	7000	10.35	3.5	20	1.0
SiC	21	2480	7.0	3.2	3.5	3.3
TiC	20	2470	4.97	4.9	3.3	6.4
Al_2O_3	15.4	2100	5.3	4.0	0.5	5.4
Si_3N_4	14	3486	3.85	3.1	0.19	0.8
Iron	12.6	400	1.96	7.8	0.803	12
SiO_2	8.4	820	0.73	2.5	0.014	0.55
Si	7.0	850	1.9	2.3	1.57	2.33
Steel	4.2	1500	2.1	7.9	0.97	12
W	4.0	485	4.1	19.3	1.78	4.5
Stainless steel	2.1	660	2.0	7.9	0.329	17.3
Mo	2.1	275	3.43	10.3	1.38	5.0
Al	0.17	130	0.70	2.7	2.36	25

below chromium (935), and almost twice as high as nickel (557), iron (400), and most common glasses (530) [24]. Silicon single crystals have a tensile yield strength (6.9×10^{10} dyne/cm^2 or 10^6 psi) which is at least 3 times higher than stainless steel wire [22,25]. In practice, tensile stress routinely encountered in seed crystals during the growth of large SCS boules, for example, can be over 18000 psi. The primary difference, between SCS and metals, is that silicon will yield by fracturing (at room temperature) while metals usually yield by deforming inelastically. Despite this quantitative evidence, we might have trouble intuitively justifying the conclusion that silicon is a strong mechanical material when compared with everyday laboratory and manufacturing experience. Sometimes wafers do break without apparent provocation; silicon wafers and parts of wafers may also easily chip. These occurrences are due to several factors which have contributed to the misconception that silicon is mechanically fragile. First, single-crystal silicon is normally obtained in large (5-13 cm diameter) wafers, typically only 10 - 20 mils (250 to 500 μm) thick. Even stainless steel of these dimensions is very easy to deform inelastically. Silicon chips with dimensions on the order of 0.6 cm x 0.6 cm, on the other hand, are relatively rugged under normal handling conditions unless scribed. As a single-crystal material, silicon has a tendency to cleave along crystallographic planes, especially if edge, surface, or bulk imperfections cause stresses to concentrate and orient along cleavage planes. Slip lines and other flaws at the edges of wafers, in fact, are usually responsible for wafer breakage. In recent years, however, the semiconductor industry has attacked this problem by contouring the edges of wafers and by regularly using wafer edge inspection instruments. These instruments are specifically designed to detect mechanical damage on wafer edges and also to assure that edges are properly contoured to avoid the effects of stress concentration. Wafer breakage, as a result of these quality control improvements, has been greatly reduced and the intrinsic strength of silicon is closer to being realized in practice during wafer handling. Chipping is also a potential problem with brittle materials such as SCS. On whole wafers, chipping occurs for the same reasons as breaking and the

solutions are identical. Individual die, however, are subject to chipping as a result of saw- or scribe-induced edge damage and defects. In extreme cases, or during rough handling, such damage can also cause breakage of or cracks in individual die. The high temperature processing and multiple thin-film depositions commonly encountered in the fabrication of IC devices unavoidably results in internal stresses which, when coupled with edge, surface, or bulk imperfections, can cause concentrated stresses and eventual fracture along cleavage planes. These factors make it clear that although high-quality SCS is intrinsically strong, the apparent strength of a particular mechanical component or device will depend on its crystallographic orientation and geometry, the number and size of surface, edge, and bulk imperfections, and the stresses induced and accumulated during growth, polishing, and subsequent processing. When these considerations have been properly accounted for, we can hope to obtain mechanical components with strengths exceeding that of the highest strength alloy steels.

Even though new techniques and novel applications of old techniques are continually being developed for use in micromechanical structures, the most powerful and versatile processing tool continues to be an etching. Chemical etchants for silicon are numerous. They can be isotropic or anisotropic, dopant dependent or not, and have varying degrees of selectivity to silicon, which determines the appropriate masking material(s). Table 2.2 gives a brief summary of the characteristics of a number of common wet silicon etches. In addition to wet chemical etches, plasma etching, reactive ion etching and sputter etching for silicon are also available.

2.2 Micromechanical Sensors and Actuators

Silicon micromachining exploits the unique structural qualities of silicon, and has been making a significant impact on the miniaturization and cost reduction of microscale sensors and actuators. Sensors and actuators are based on the transfer of a physical quantity from one energy domain into another. These are the well-known radiant,

Table 2.2 Characteristics of silicon wet etchants [1]

Etchant (Diluent)	Typical Composition	Temp (°C)	Etch Rate (μm/min.)	Dopant Dependency
HF HNO_3 (water, CH_3COOH)	10 ml 30 ml 80 ml	22	0.7 - 3.0	$< 10^{17} cm^{-3}$ n or p reduces etch rate by about 150
	25 ml 50 ml 25 ml	22	40	no dependency
	9 ml 75 ml 30 ml	22	7.0	
Ethylene-diamine Pyrocatechol (water)	750 ml 120 gr 100 ml	115	0.75	$> 7x10^{19} cm^{-3}$ boron reduces etch rate by about 50
	750 ml 120 gr 240 ml	115	1.25	
KOH (water, isopropyl)	44 gr 100 ml	85	1.4	$>10^{20} cm^{-3}$ boron reduces etch rate by about 20
	50 gr 100 ml	50	1.0	
H_2OH (water)	10 gr 100 ml	65	0.25 - 1.0	$> 3x10^{20} cm^{-3}$ boron reduces etch rate by about 10

mechanical, electrical, magnetic, thermal and chemical domains. The application of an electric, magnetic or other field on a piece of material will cause an effect in this material. It is well known that a mechanical stress evokes a strain, an electrical voltage on a conductor an electric current, a temperature gradient a heat flow, etc. These are the well-known effects described by Hooke's, Ohm's and Fick's law, respectively. These effects are characterized by the fact that cause and effect are in the same energy domain, mechanical, electrical and thermal, respectively. We also know that an electric field does not exclusively evoke an electric current and a temperature gradient does not exclusively evoke a heat current, but that these effects are often coupled. Thus the thermoelectric effects, are a subgroup of the cross effects, in which energy is generally transferred from one energy domain into another. These cross effects form the basis for the design of sensors and actuators. By using these cross effects and micromachining techniques, many high performance sensors and actuators have been reported and are listed below.

(1) Physical sensors : Pressure sensors [10,11,12], Accelerometers [9,13,14,15], Gas flow meter [26], Position sensor [27,28], Strain gauge [29], Linear variable differential transformer (LVDT) [30], Resonant sensor [31,32], Displacement sensor [33,34]

(2) Optical Sensors : Infrared sensor [35], Fiber-optic pH sensor [36], Optical torque sensor [37] Color Sensor [38]

(3) Acoustic Sensors : Acoustic gas sensor [39], Acoustic object recognition sensor [40] Ultrasonic transducer for flow measurement [41], Subminiature microphone [42]

(4) Magnetic Sensors : Fluxgate sensor [43], Magnetometer [44], Hall sensor [45], Thermal fluxmeter [46]

(5) Optical Fiber Sensors : Optical fiber flow meter [47], Optical fiber refractometer [48], Optical fiber gas sensor [49]

(6) Infrared and Radiation Sensors : Infrared gas analyzer [50] Thermovoltaic IR detector [51], Ultraviolet sensitive CCD detector [52]

(7) Thermal and Humidity Sensors : Thermopile sensor [53], Temperature sensor [54], Humidity sensor [55]

(8) Chemical and Biomedical Sensors : Liquor sensor [56], Gas sensor [57], Ion detector [58]

(9) Actuators : Micromotors [59,60], Microengines [61], Microgripper [62], Microhinges [63], Micropump [64], Microvalve [65] Micro flow control system [66], Shape memory alloy [67,68]

2.3 Accelerometers

The forces arising from acceleration can be determined by inferring it from the displacement of a sprung mass or the stress/strain in the spring mounting. There are largely two types of accelerometers, one is an analog type the other is a threshold type. For the analog type, several technologies have been developed and they are as follows.

(1) Silicon piezoresistive [13,15]

Silicon exhibits the piezoresistive effect, can be chemically micromachined with great precision, is very strong and is mechanically stable as described in section 2.1. Large volumes of sensors can be manufactured at low cost (because of small size and batch processing), and the conditioning electronics can be integrated with the sensors. Piezoresistive accelerometers are normally either single-ended cantilever or of a double-ended bridge design. The former have the advantage in that a smaller area of silicon is used to achieve a given sensitivity, but the latter are stronger and, using a multitude of piezoresistors, can be made less sensitive to cross-axis accelerations. Schematic representations of each type are given in Fig. 2.1(a) and (b) showing the provision for over-range protection and air damping. The main disadvantages of these are that piezoresistive characteristics are quite temperature sensitive, and they are very sensitive to mounting and other induced stresses.

(2) Silicon Capacitive [69]

facing 12

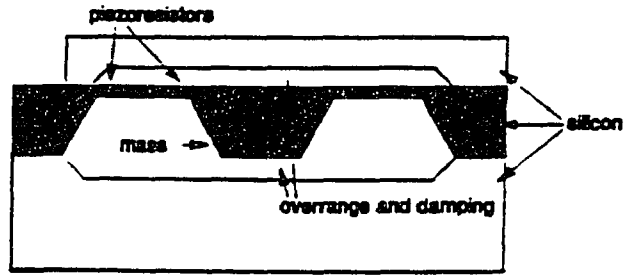

(a)

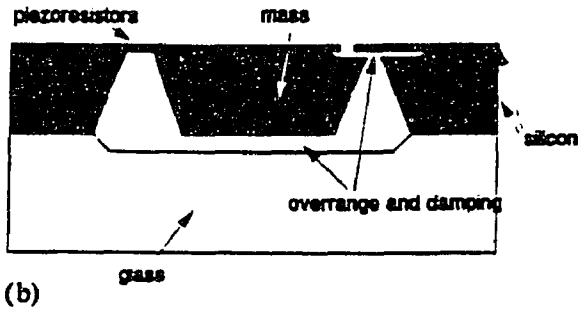

(b)

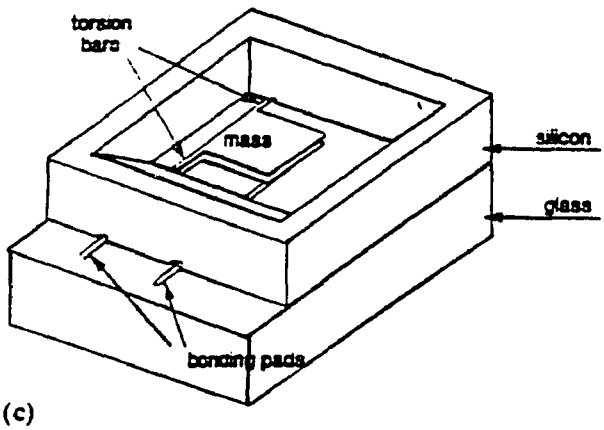

(c)

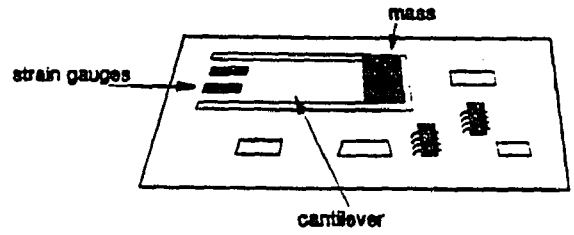

(d)

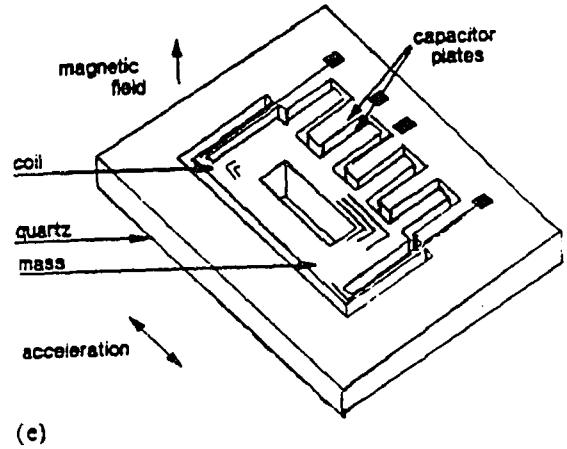

(e)

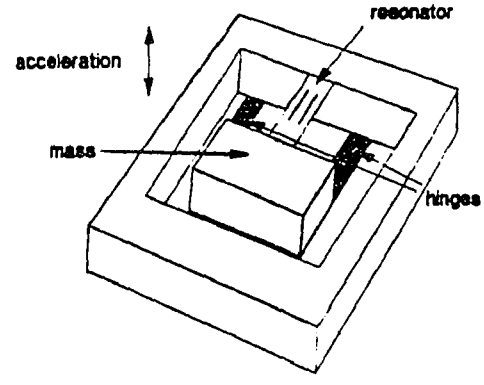

(f)

Figure 2.1 Accelerometers using various measurement techniques: (a) and (b) silicon piezoresistive; (c) silicon capacitive; (d) strain gauge; (e) force balance; (f) micromachined

The problems outlined in the silicon piezoresistive type accelerometers are substantially overcome by using a capacitive measurement method, however, there are the disadvantages that electromagnetic interference is a greater problem, the output is inherently non-linear and the conditioning electronics is more complex. Fig. 2.1(c) shows a design using a torsional mounting arrangement, but the design could be similar to the two piezoresistor designs.

(3) Thick-film Strain Gauge [70]

Sensors exploiting the substantial strain sensitivity of a typical thick film can be produced at very low cost in both medium and large production volumes. Fig. 2.1(d) outlines one possible cantilever accelerometer design. The main problem here is that standard substrate materials (e.g. alumina) are very stiff and so it is difficult to design a structure which offers high strains (and therefore high sensitivity) and at the same time achieve both a reasonable robustness and acceptable bandwidth.

(4) Piezoelectric

Piezoelectric materials can be used for sensing stress arising from acceleration in either single crystal, polymer film or piezoceramic form. Polymer film may be the most cost effective in large volumes but it has a more limited operating temperature range. These materials, due to charge leakage and pyroelectric effects, cannot be used for measuring static forces and hence static accelerations. However, with careful design, responses approaching near DC level can be achieved, as demonstrated by a micromachined silicon accelerometer incorporating a thin piezoelectric ZnO film feeding directly into an integrated MOSFET [71].

(5) Force Balance [72]

An electromagnetic or electrostatic force is generated which opposes the acceleration forces, thus the mass maintains an equilibrium position and the energy required is a measure of the applied acceleration. The control or error signal is generated by a position sensor, often using a capacitive measurement principle. Micromachined silicon and quartz

force balances are described [73,74] in which the force is applied by Lorentz force coupling and the error signal is the capacitance between the fixed and moving electrodes. The quartz device is shown schematically in Fig. 2.1(e). In general, force balance devices offer good performance because a wide bandwidth and high sensitivity can be achieved, but normally they are more complex and expensive than other non-feedback methods.

(6) Micromachined Resonator [75]

When the tension in a guitar string is changed there is a corresponding change in the resonant frequencies which create its characteristic timber. Similarly, the resonant frequencies, for example, of the bridge structure shown in Fig. 2.1(f) are also changed. The resonator becomes a stress sensitive element capable of detecting acceleration forces, where the output is in the pseudo-digital form of a frequency. The structure can readily be fabricated by the micromachining of silicon. The excitation is normally electrostatic or either photothermal (using incident light from an optical fiber) or electrothermal (using joule heating in a diffused resistor). A very high resolution can be achieved but the thermal excitation can cause undesirable thermal stresses. Also, the complexity deems them very expensive at present. Single crystal quartz resonators can also be made which utilize the inherent piezoelectric effect, although there is some difficulty in micromachining the appropriate structures.

2.4 Threshold Accelerometers

2.4.1 Background

The rapidly advancing techniques for the micromachining of silicon allow for the fabrication of a multitude of miniaturized sensors and actuators. Among these, sensors for pressure and acceleration have attained the highest degree of industrial development. Most silicon accelerometers published to date use the piezoresistive principle to measure the mechanical strain in a cantilever beam, deflected by a seismic mass under acceleration.

In 1972, Frobenius et al. [18] described microminiature ganged threshold

accelerometers made from an all-metal cantilever beam micromechanical switch. The cantilever beams were fabricated out of electroplated gold on a substrate of either a glass slice or an oxidized silicon wafer. They reported that each beam had been closed and opened repeatedly, while the speed of the centrifuge had been alternatively increased and decreased. In 1987, Harry Diamond Laboratories (HDL) [19] conducted a review of three different threshold accelerometers made by Honeywell, Motorola, and HDL. Honeywell's design for a multiple g-switch chip had cantilever beams which were 15 μm thick by 250 μm wide epitaxial silicon with an integral silicon end mass and along-the-beam contact metallization. Centrifuge testing of prototype g-switches indicated two problems: only about 50 percent of the contacts were functional, and the closure acceleration levels of those that functioned were much higher than expected (nearly an order of magnitude for the lowest range beam). The Motorola accelerometer utilized a silicon dioxide beam with a gull wing contact at the tip of the beam for a two-point contact switch. The beams were made from thermally grown 3 μm thick SiO_2 on a silicon substrate. They were 30 μm wide with lengths ranging from 150 to 435 μm. Under acceleration, each beam deflected through a gap of 1 μm until a deposited metal contact at the tip of the beam touched and bridged across two metal trace patterns located on the substrate. This contact configuration did not require metallization along the beam's surface. Preliminary screening of the fabricated devices was attempted by the use of electrostatic attraction to deflect the beams until the switches closed. Voltages in the range of 30 to 100V (with current limited to 0.1 μA) closed the switches but they would not open because the pure gold contacts welded. Tests of other units on a centrifuge showed that some switches would close, but at accelerations many times the design level. The third device, by HDL, consisted of a silicon die supporting three all-metal, gold-nickel-gold sandwich beams. Under acceleration, each beam deflected across a 1 μm gap to close the switch in single-point contact against metallization on the chip surface. The beams had a single 0.1 μm layer of nickel sandwiched between two 0.9 μm layers of evaporated gold. This structure increased

stiffness, strength, and elasticity and attempted to compensate for warping due to differential thermal expansion. The beams were 50 μm wide and 100 to 235 μm long to provide switch closures in the acceleration range of 380 to 9600 g. Centrifuge tests of sample beams at acceleration levels over three times the expected closure level did not give any switch closures. This was probably due, in large part, to the excessive contact gap. Other beam samples were found to be stuck closed before testing and the contacts could not be opened under reverse acceleration on the centrifuge. In 1991, Loke et al. [20] described a threshold accelerometer made of silicon dioxide cantilever beam with a metal line (gold with chrome as an intermediate layer) running along its length. Under an applied acceleration, the beam deflected upward across a gap and made contact with a second electrode, thus closing a switch. They reported that the switches (beams 120 to 400μm long and 80μm wide and 2.5μm gap) closed electrostatically with voltages in the 10 to 70 volts region. All the above mentioned devices (except that of Frobenius which involved metal deposition by evaporation and electroplating) were fabricated by exploiting the bulk micromachining process and they had two metal contacts for the switch closure.

2.4.2 Advantages of cantilever beam threshold accelerometers

In analog type accelerometers, electronic circuitry is needed close to the sensor for amplifying the signal, compensating for temperature effects and non-linearity, and device-to-device variations in offset and sensitivities. In the case of threshold type accelerometers, the accelerometer generates a signal when the acceleration is greater than the predetermined value. Therefore, analog readout of acceleration is not needed. A threshold accelerometer is much simpler in design and is cost effective because no additional readout circuit is necessary. The threshold accelerometer itself acts as a switch which generates a signal when the acceleration is greater than the predetermined value, and it also has an extremely high on-to-off resistance ratio.

The cantilever has several attractive features as an accelerometer design. Its deflection is a linear function of acceleration, eliminating the need for calibration curves, and it is inherently sensitive to accelerations in only one direction. Further, the response per unit acceleration is a function of the dimensions of the beam and the mass loading it. The sensitivity and range can be varied over a wide range yet, given good control over beam dimensions, devices with the same nominal sensitivity will be reasonably well matched. The other advantage of the cantilever beam involves fabrication considerations. The most important of which are the cantilever's simplicity and attendant adaptability to the constraints of techniques available for shaping silicon on such a small scale.

CHAPTER 3

PRINCIPLE OF OPERATION

3.1 Geometry

In order to understand how the threshold accelerometers work, it is first necessary to understand their construction. Fig. 3.1(a) and Fig. 3.2(b) show a planar view and a cross-section view of a typical threshold accelerometer.

The threshold accelerometer in this thesis is a microfabricated cantilever beam having two electrically separated electrodes. One electrode is free to move while the other is fixed on the top of a substrate. It is analogous to a mechanical single-pole-single-throw (SPST) switch. An acceleration a produces a force F to the cantilever, whose mass is m, according to Newton's second law.

$$F = ma \tag{3.1}$$

The cantilever bends with the force in the direction of the force applied, and the deflection of an uniform cantilever beam is given by [77]

$$y = \frac{wx^2}{24EI}(x^2 + 6L^2 - 4Lx) \tag{3.2}$$

where w is a uniformly distributed load per unit length, E is Young's modulus of the material, I is a moment of inertia of plane area with respect to an axis in its plane, L is the length of the beam and x is the distance from the fixed end of the beam. The moment of inertia for a rectangular cross section of a beam is [78]

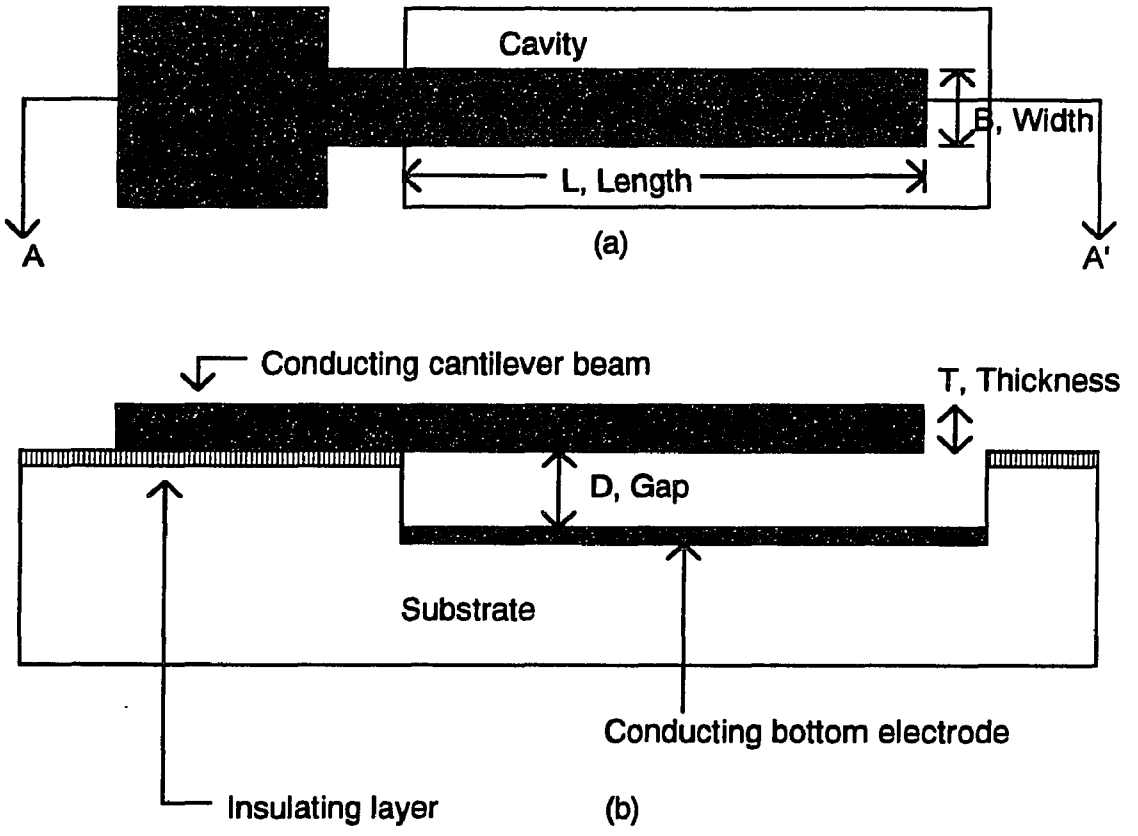

Figure 3.1 Geometry and description of parameters of a typical threshold accelerometer: (a) plannar view; (b) cross-section A-A'

$$I = \frac{WT^3}{12} \tag{3.3}$$

where W and T are the width and the thickness of the beam, respectively, and the uniformly distributed load w can be rewritten as

$$w = \rho WTa \tag{3.4}$$

where ρ is a density of the material.

From equations (3.2) through (3.4), the beam deflection can be formulated as a function of an applied acceleration as

$$y = a\frac{\rho x^2}{2ET^2}(x^2 + 6L^2 - 4Lx) \tag{3.5}$$

Eqn. (3.5) tells two interesting facts, one of which is that the deflection is a linear function of the applied acceleration and the other is, it is not a function of the beam width.

The maximum deflection occurs at the tip of the beam and it can be obtained by substituting x by L in Eqn. (3.5) as

$$y_{Tip} = a\frac{3\rho L^4}{2ET^2} \tag{3.6}$$

Fig. 3.2 shows an example graph of beam deflection versus distance x from the fixed end of the beam using typical device parameters and material values given in table 3.1. Material values are based on tantalum silicide ($TaSi_2$).

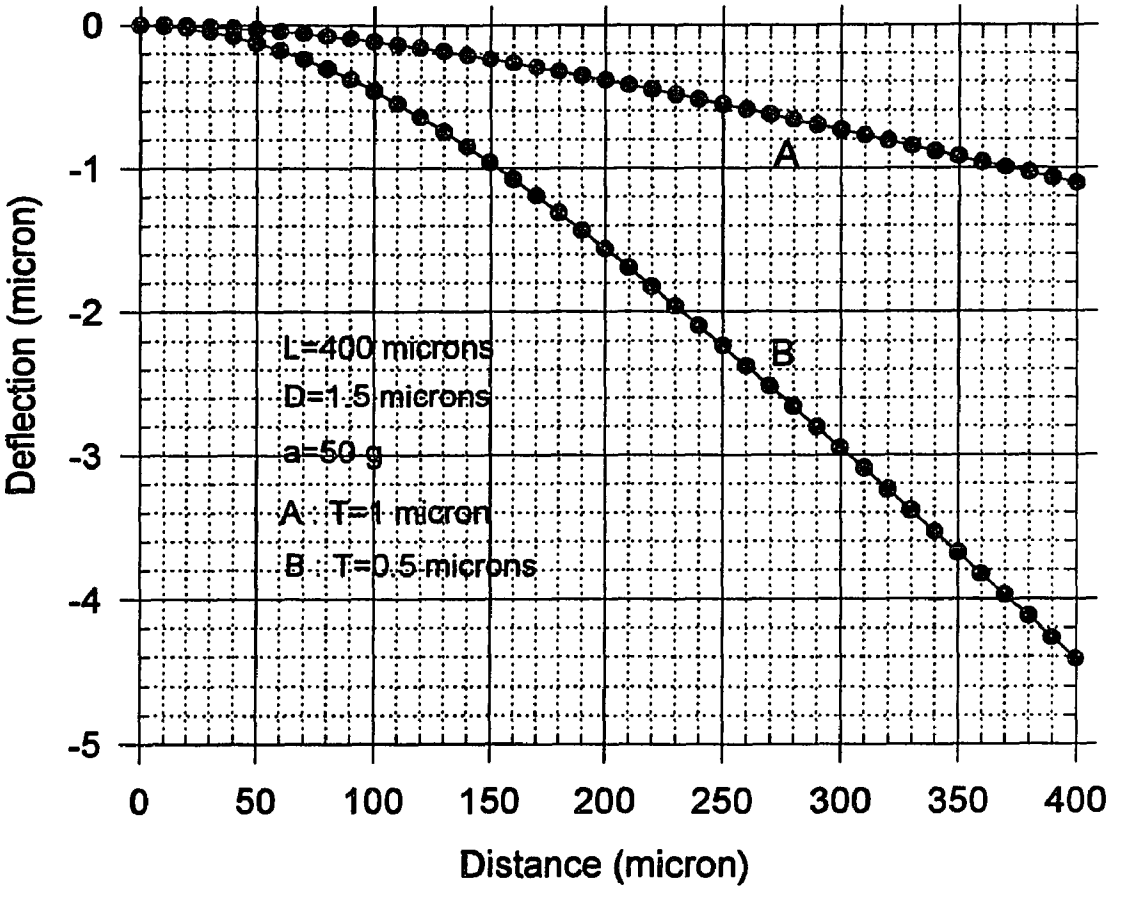

Figure 3.2 Beam deflection versus distance x from the fixed end of the beam

Table 3.1 Dimension and material parameters of an accelerometer to calculate the deflection with respect to the distance x in figure 3.2

Parameter	**Symbol**	**Typical value**
Density ($TaSi_2$)	ρ	9.08×10^3 (kg/m^3)
Young's Modulus ($TaSi_2$)	E	158×10^9 (Pascal)
Length	L	400 (μm)
Thickness	T	0.5 and 1 (μm)
Gap between Electrodes	D	1.5 (μm)
Acceleration	a	50 (g)

3.2 Electrostatic Analysis

An application of a voltage between the conducting contact pad on the beam and the button electrode will result in an attractive electrostatic force. The electrostatic force F_e between two parallel plate is [79]

$$F_e = \frac{\varepsilon_o A V^2}{2(D - y_{Tip})^2} \tag{3.7}$$

for $y_{Tip} << D$

where ε_o = permittivity of air

V = applied voltage

D = original distance between plates.

$A = WL$ = effective parallel plate area

(where W and L are width and length of the beam, respectively)

This force is not constant but changes with the deflection of the beam; i.e., F_e increases with increasing deflection y_{Tip}. The expression for voltage is found by equating the electrostatic force to the restoring force which tries to restore the beam to the original position. The restoring force is equal to the force applied to the beam, which is

$$F_r = wL = \rho WTLa \tag{3.8}$$

From the Eqns. (3.6) and (3.8)

$$F_r = \frac{2EWT^3}{3L^3} y_{Tip} \tag{3.9}$$

Now from Eqns. (3.7) and (3.9)

$$V = \Gamma\sqrt{y_{Tip}}(D - y_{Tip}) \tag{3.10}$$

where $\Gamma = \frac{4ET^3}{3\varepsilon_o L^3}$ which is a constant determined by the material and device dimension. This equation relates the deflection y_{Tip} and the voltage required to hold the beam at the deflection y_{Tip}.

Fig. 3.3(a) shows that the required voltage rises until the deflection reaches $D/3$ and falls down afterward. Fig. 3.3(b) shows the restoring force and electrostatic force with applied voltage V as a parameter. If V is smaller than the threshold voltage V_{th} (see graph A in Fig 3.3(b)), the beam begins to bend because, the electrostatic attractive force is greater than the restoring force ($F_e > F_r$) until it reaches the point ① where two forces are equal ($F_e = F_r$). As V increases the equivalent point moves toward the point ② where the threshold occurs. If V is greater than the threshold voltage (see graph C in Fig. 3.3(b)), the electrostatic force is greater than the restoring force whatever the deflection y_{Tip} is and the beam will snap shut.

This threshold voltage can be obtained by taking the derivative of V with respect to y_{Tip}. From Eqn. (3.10),

$$\frac{dV}{d(y_{Tip})} = \frac{\Gamma}{2}\left(\frac{D}{\sqrt{y_{Tip}}} - 3\sqrt{y_{Tip}}\right) \tag{3.11}$$

By letting $\frac{dV}{d(y_{Tip})} = 0$, the resulting expression has a maximum value at $y_{Tip} = \frac{D}{3}$, which checks Fig. 3.3(a), and is given by

$$V_{th} = \frac{4}{9}\sqrt{\frac{ET^3D^3}{\varepsilon_o L^4}} \tag{3.12}$$

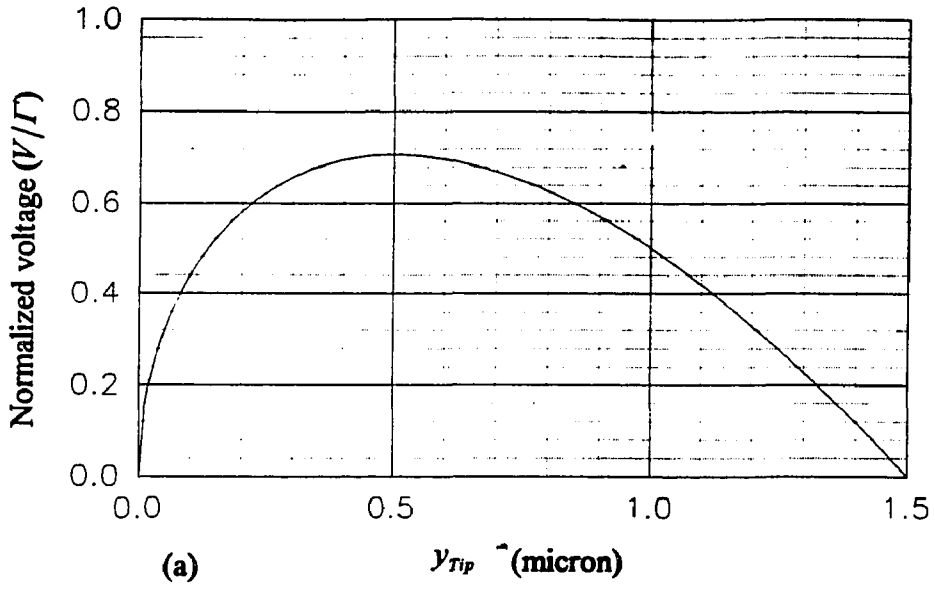

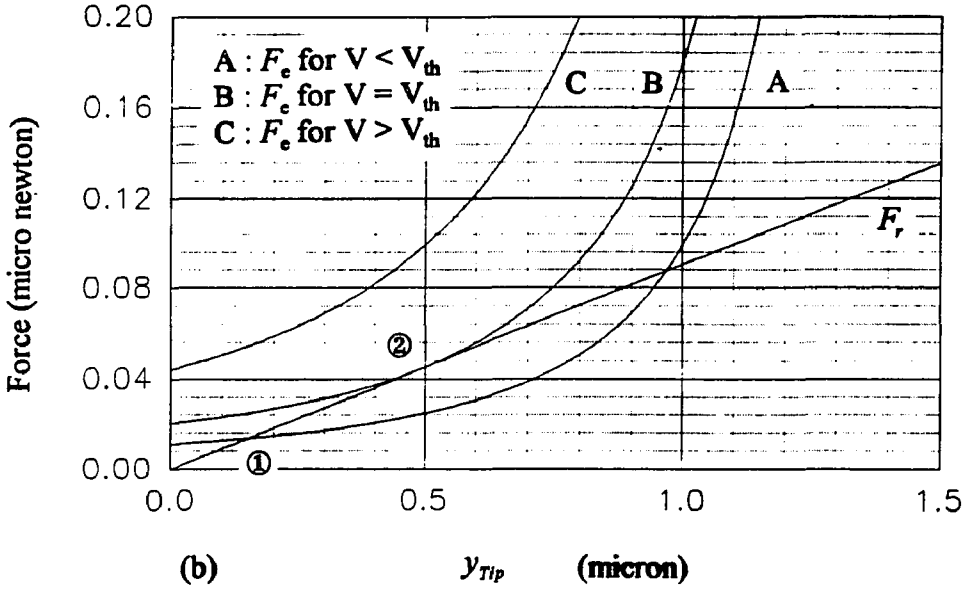

Figure 3.3 (a) Normalized voltage (V/Γ) versus y_{Tip}; (b) Electrostatic force (F_e) and restoring force (F_r) versus y_{Tip}

This parallel plate model ignores the fact that the electrostatic force varies as the gap between electrodes varies along the beam length L. In chapter 4, more precise models than parallel plate model compensating the above fact are suggested for electrostatic force calculation.

3.3 Threshold Acceleration Analysis

The deflection y due to its inertial mass under an applied acceleration a is given by Eqn. (3.5) and the maximum deflection occurs at a tip of the beam as given by Eqn.(3.6) as $y_{Tip} = 3\rho L^4 a / 2ET^2$. However, a threshold accelerometer in operation will require a voltage to be placed across the electrodes. This applied voltage will contribute an electrostatic attraction that will affect the threshold acceleration level of the device.

The beam will deflect under an applied acceleration , if it is large enough, until it reaches a threshold distance whereby the electrostatic attraction will snap it shut. From Eqn. (3.12) the threshold distance for an applied voltage V is given by

$$D_{th} = \left(\frac{9V}{4}\right)^{2/3}\left(\frac{\varepsilon_o L^4}{ET^3}\right)^{1/3} \tag{3.13}$$

With an original beam spacing D and beam deflection y_{Tip}, the threshold distance can be rewritten as

$$\left(D - y_{Tip}\right) = \left(\frac{9V}{4}\right)^{2/3}\left(\frac{\varepsilon_o L^4}{ET^3}\right)^{1/3} \tag{3.14}$$

Substituting Eqn. (3.6) into Eqn.(3.14) results in the threshold acceleration required to close a beam under an applied voltage is

$$a_{th} = \frac{D - \left(\frac{9V}{4}\right)^{2/3}\left(\frac{\varepsilon_o L^4}{ET^3}\right)^{1/3}}{\left(3\rho L^4 / ET^2\right)} \tag{3.15}$$

Fig. 3.4 shows graphs relating threshold acceleration versus applied voltage. Graph B is obtained by using the parameter values given in table 3.1. The threshold acceleration decreases as the beam length increases. Graph A shows the threshold acceleration using the same parameter values as graph B except the beam length is 20 percent longer than that of graph B. Conversely, the threshold acceleration increases as either the beam thickness or the gap distance between electrodes (or both) increases. Graphs C and D show the threshold accelerations with the same parameter values in table 3.1 except the beam thickness is 50 percent thicker and the gap distance 50 percent wider than that of graph B, respectively. Chapter 5 describes more detail about the dimensional consideration for accelerometer design.

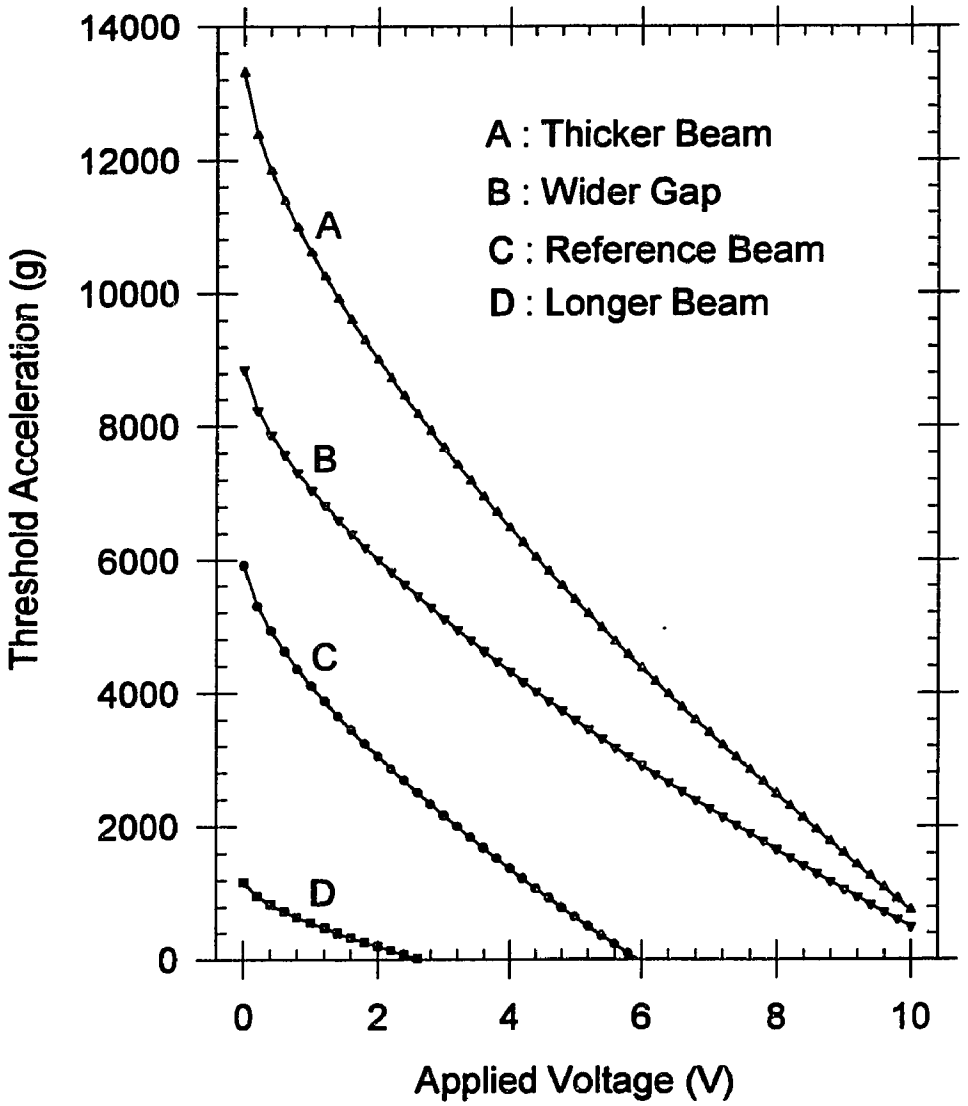

Figure 3.4 Threshold acceleration versus applied voltage

CHAPTER 4

NEW MODELS FOR ELECTROSTATIC FORCE

Precise calculation of an electrostatic force acting on a cantilever beam is very important in the design of threshold accelerometers. In the conventional parallel plate model, they assume that the entire beam is moving by the distance of y_{Tip} (see line $\overline{A'C}$ in Fig. 4.1) but, the beam bends according to the Eqn. (3.5). The typical shape of this bending is illustrated in Fig. 3.2 (see catenary shape AC in Fig. (4.1)). In the parallel plate model, the electrostatic force is obtained by the formula

$$F_{pp} = \frac{\varepsilon_o A V^2}{2(D - y_{Tip})^2} \tag{4.1}$$

where ε_o = permittivity of air

V = applied voltage

D = original distance between plates

$A = WL$ = effective parallel plate area

where W and L are width and length of the beam, respectively

This model is good as far as $D >> y_{Tip}$ but, in the threshold type accelerometer, the beam is supposed to make a contact with the bottom electrode traveling all the way across the gap D. Now the condition $D >> y_{Tip}$ does not hold and the above formula is no longer valid to calculate reasonably acceptable electrostatic force.

Several models are suggested to improve the precision of the electrostatic force calculation. In Sect. 4.1, a triangle model is introduced. This model assumes that the beam bends not catenary, but straight from the fixed end to the free end of the beam (see Fig. 4.2). In Sect. 4.2, a more precise model called a two point piecewise linear model is

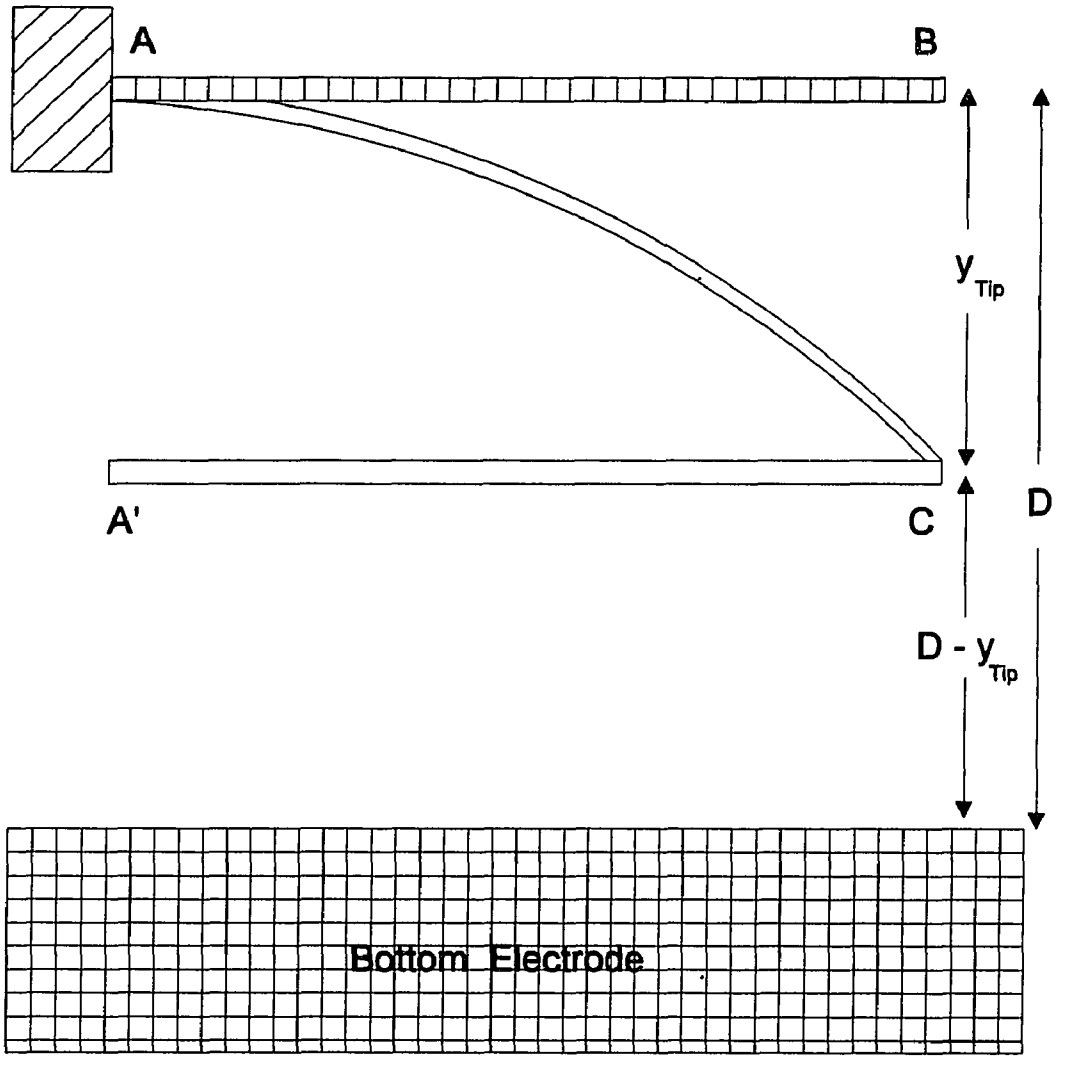

Figure 4.1 Beam bending assumed for the parallel plate model

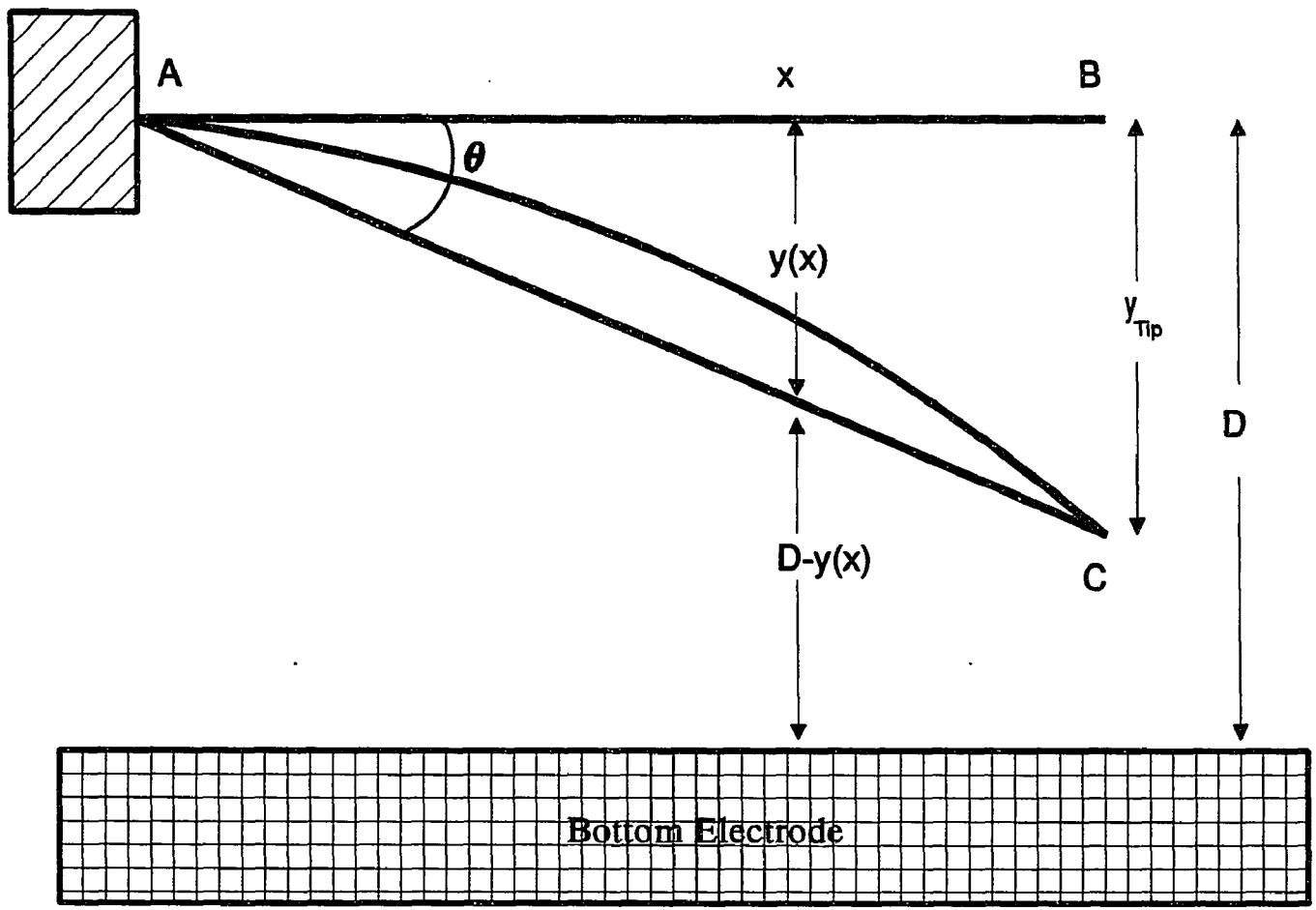

Figure 4.2 Beam bending assumed for the triangle model

described, and generalized N-point piecewise linear model is also analyzed. In Sect. 4.3 threshold acceleration analysis on the triangle model is considered.

4.1 Triangle Model

In this model the beam is assumed to bend not catenary but straight (line $\overline{AC}$) as shown in Fig. 4.2. Since line $\overline{AC}$ is closer to the actual beam bending than line $\overline{A'C}$ of Fig. 4.1, and thus it gives more precise electrostatic force. Here, lines $\overline{AB}$ and $\overline{AC}$ are equal to the beam length L.

$$\overline{AB} = \overline{AC} = L \tag{4.2}$$

Line $\overline{BC}$ is equal to the beam deflection at the free end tip and from Eqn.(3.6), it is given as

$$\overline{BC} = y_{Tip} = \frac{3\rho L^4 a}{2ET^2} \tag{4.3}$$

The angle θ between lines $\overline{AB}$ and $\overline{AC}$ is obtained by dividing the arc BC by L. Since θ is very small, $arc(BC) = \overline{BC} = y_{Tip}$, we have

$$\theta = \frac{y_{Tip}}{L} = \frac{3\rho L^3 a}{2ET^2} \tag{4.4}$$

The deflection at arbitrary point x along the beam is

$$y(x) = \theta x = \frac{3\rho L^3 a}{2ET^2} x \tag{4.5}$$

Differential electrostatic force $\Delta F_e(x)$ due to differential area $\Delta A = W \Delta L$ at point x is

$$\Delta F_e(x) = \frac{\varepsilon_o V^2 W \Delta L}{2[D - y(x)]^2} \tag{4.6}$$

where W is a width of the beam which is constant in uniform cantilever beams.

The total electrostatic force is obtained by integrating $\Delta F_e(x)$ from $x = 0$ to $X = L$

$$F_e = \int_o^L \Delta F_e(x)dx = \frac{\varepsilon_o V^2 W}{2}\int_o^L \frac{dx}{(D - \theta x)^2}$$

$$= \frac{\varepsilon_o V^2 W}{2}\left[\frac{1}{\theta(D - \theta x)}\right]_o^L = \frac{\varepsilon_o V^2 W}{2}\frac{L}{D(D - \theta L)}$$

$$= \frac{\varepsilon_o A V^2}{2D(D - y_{Tip})} \tag{4.7}$$

It is worth comparing Eqns. (4.1) and (4.7). The denominator of Eqn.(4.7) has D instead of $(D - y_{Tip})$. This means that the denominator has factors which consist of the gap distances of both end tips of a cantilever beam, i.e., $(D - y_{Tip})$ for both ends for parallel plate model while D and $(D - y_{Tip})$ for triangle model.

4.2 Two Point Piecewise Linear Model

In this model the beam is assumed to bend along two piecewise linear lines $\overline{AH}$ and $\overline{HC}$ (see Fig. 4.3). Point I is set so as to bisect the beam length L.

$$\overline{AI} = \overline{BI} = \frac{L}{2} \tag{4.8}$$

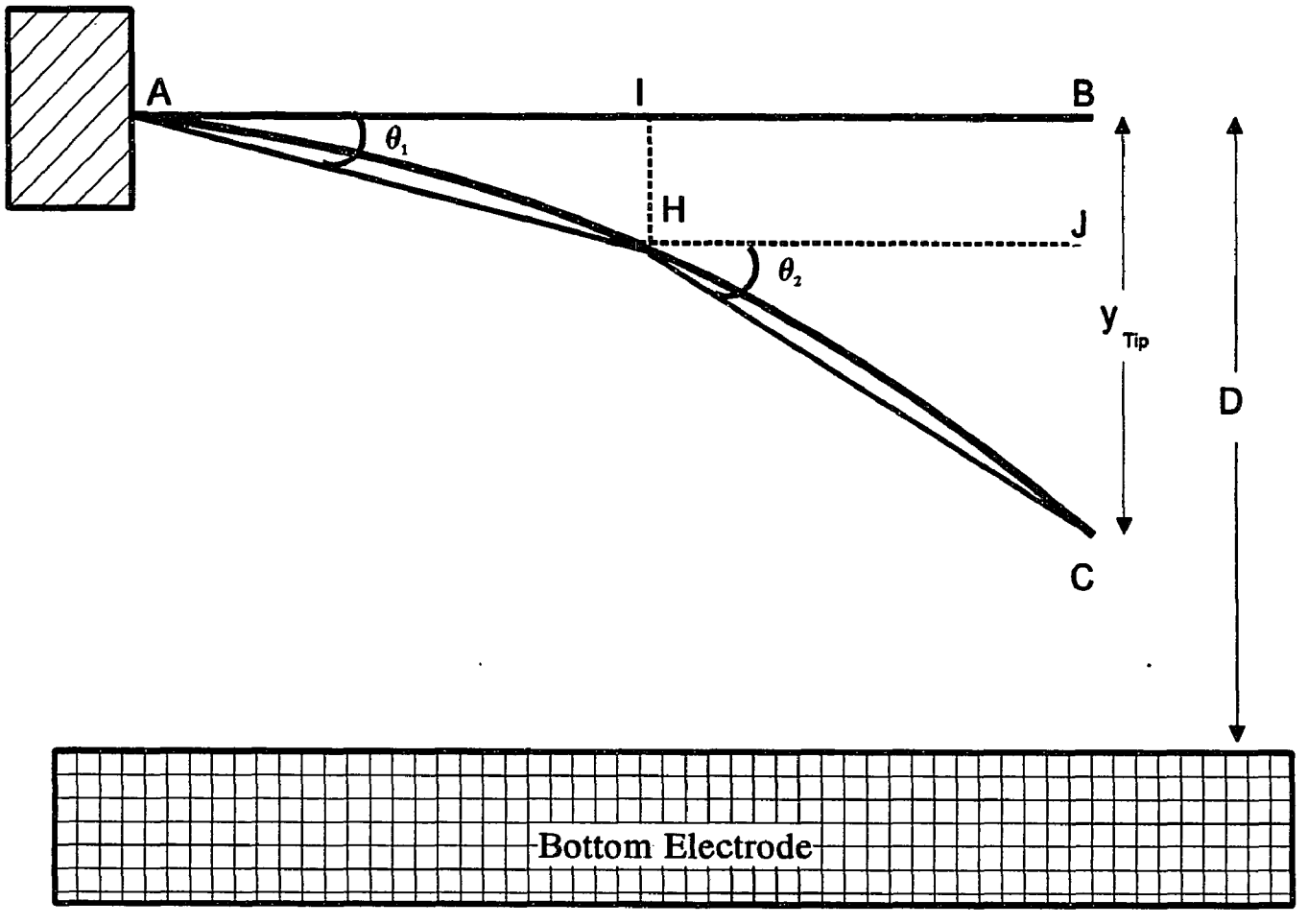

Figure 4.3 Beam bending assumed for the 2 point piecewise linear model

H is a point on the beam at $x = \frac{L}{2}$, and deflection at this point is obtained from Eqn. (3.5) with $x = \frac{L}{2}$,

$$\overline{IH} = y_{x=L/2} = \frac{17\rho L^4 a}{32ET^2} = \frac{17}{48} y_{Tip} \tag{4.9}$$

Angles θ_1 (between lines $\overline{AI}$ and $\overline{AH}$) and θ_2 (between lines $\overline{HJ}$ and $\overline{HC}$) are

$$\theta_1 = \overline{IH}\frac{2}{L} = \frac{17 y_{Tip}}{24L} \tag{4.10}$$

$$\theta_2 = \frac{y_{Tip} - \overline{IH}}{L/2} = \frac{31 y_{Tip}}{24L} \tag{4.11}$$

The electrostatic force acting on the beam is a sum of two electrostatic forces F_{AH} and F_{HC} exerting on beam segments AH and HC

$$F_e = F_{AH} + F_{HC} = \int_o^{L/2}\left(\frac{\varepsilon_o V^2 W}{2(D-\theta_1 x)^2}\right)dx + \int_o^{L/2}\left(\frac{\varepsilon_o V^2 W}{2\left(D - \frac{17 y_{Tip}}{48} - \theta_2 x\right)^2}\right)dx$$

$$= \frac{\varepsilon_o A V^2}{4}\left[\frac{1}{D\left(D - \frac{17 y_{Tip}}{48}\right)} + \frac{1}{\left(D - \frac{17 y_{Tip}}{48}\right)(D - y_{Tip})}\right]$$

$$= \frac{\varepsilon_o A V^2}{4}\frac{2D - y_{Tip}}{D\left(D - \frac{17 y_{Tip}}{48}\right)(D - y_{Tip})} \tag{4.12}$$

The electrostatic force is obtained by integrating the differential electrostatic force $\Delta F_e(x)$ in Eqn. (4.6) and $y(x)$ in this equation is taken from Eqn. (3.5). Eqn. (3.5) represents actual beam bending instead of Eqn. (4.5) which is for the straight beam bending assumed in the triangle model.

$$F_e = \frac{\varepsilon_o A V^2}{2} \int_0^L \frac{dx}{[D - y(x)]^2}$$

$$= \frac{\varepsilon_o A V^2}{2} \int_0^L \frac{dx}{\left[D - \frac{a\rho}{2ET^2}\left(x^4 + 6L^2x^2 - 4Lx^3\right)\right]^2} \tag{4.13}$$

There is no analytic solution for this equation. Using numerical method, the actual electrostatic force is calculated. Comparisons of electrostatic force calculated with different models are shown in Fig. 4.4, and the errors of the linear models with respect to the integration (Eqn. 4.13) are shown in Fig. 4.5. The errors, for 50 g acceleration, are respectively about 2 % and 10 % for the 2 point piecewise linear model and the triangle model, while the error of the parallel plate model is more than 90 %.

In generalized N-point piecewise linear model, the catenarily bent beam $arc(AC)$ is divided equally into N piecewise linear lines ($\overline{AA_1}$, $\overline{A_1A_2}$, ... $\overline{A_{k-1}A_k}$, ... $\overline{A_{N-1}C}$) as shown in Fig. 4.6. Their lengths are

$$\overline{AA_1} = \overline{A_1A_2} = \ldots\ldots = \overline{A_{k-1}A_k} = \ldots\ldots = \overline{A_{N-1}C} = \frac{L}{N} \tag{4.14}$$

Angle θ_k (between lines $\overline{A_kA_{k+1}}$ and $\overline{A_kC_{k+1}}$) can be obtained by

$$\theta_k = \frac{\overline{C_{k+1}A_{k+1}}}{\overline{A_kA_{k+1}}} = \frac{y_{k+1} - y_k}{L/N} \tag{4.15}$$

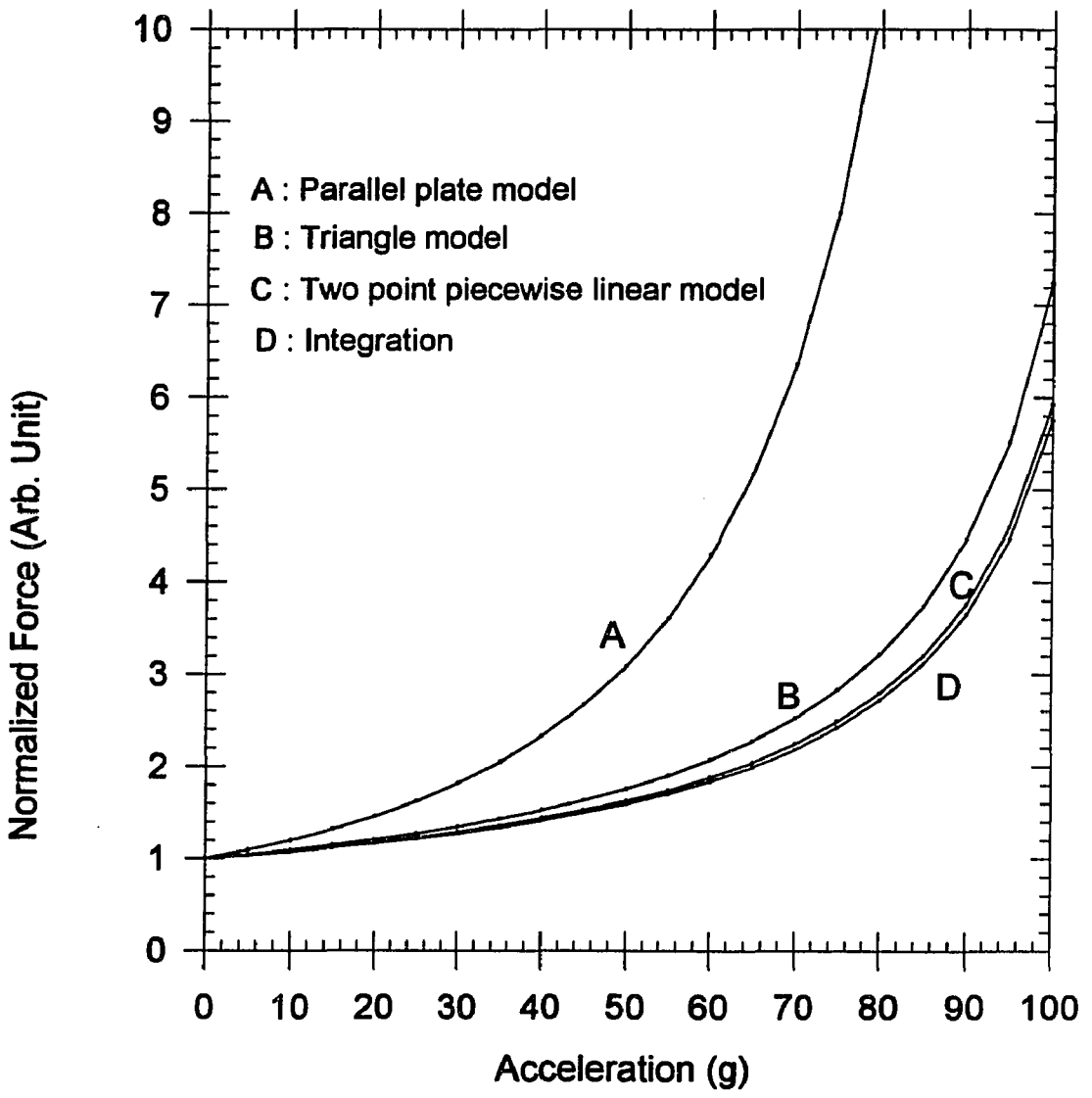

Figure 4.4 Electrostatic force versus acceleration for 4 different models: (A) Parallel plate model; (B) Triangle model; (C) Two-point piecewise linear model; (D) Integration (using Eqn. 4.13)

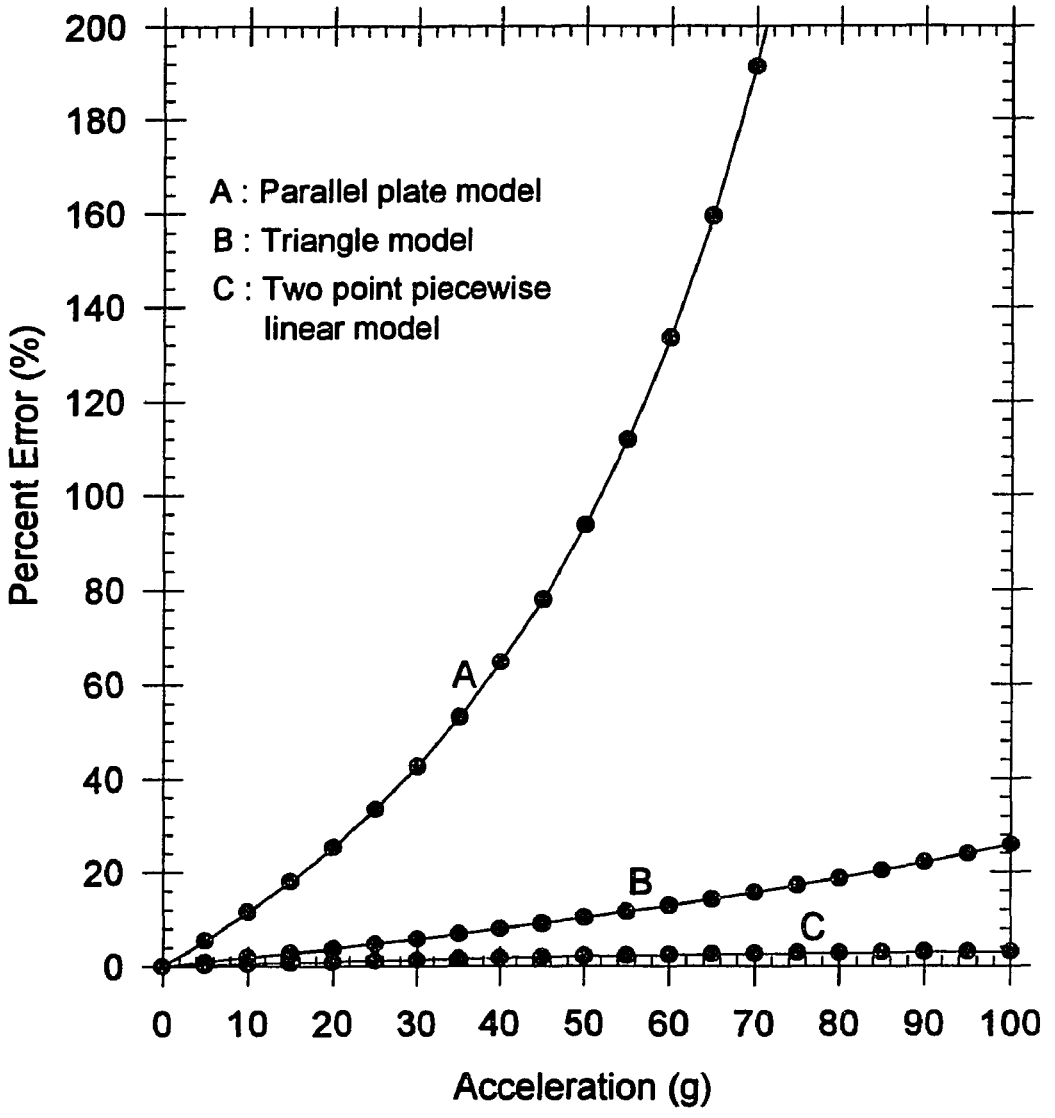

Figure 4.5 Percent error in comparison with integration (Eqn. 4.13) versus acceleration for 3 linear models: (A) Parallel plate model; (B) Triangle model; (C) Two-point piecewise linear model

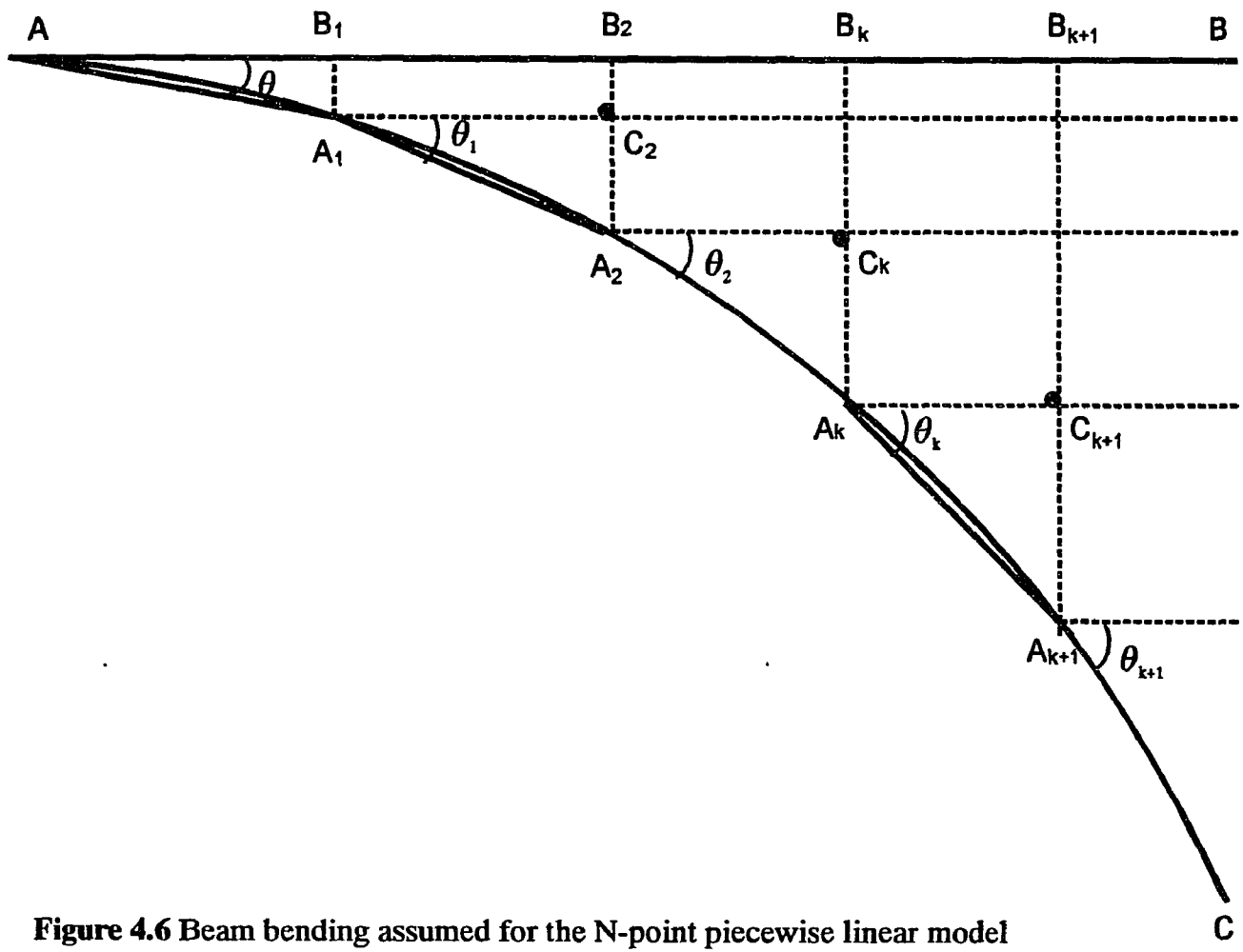

Figure 4.6 Beam bending assumed for the N-point piecewise linear model

where y_k is the beam bending at $x = kL/N$ and it is given by

$$y_k = \overline{B_k A_k} = y(x)\big]_{x=kL/N} \tag{4.16}$$

where $y(x)$ is given in Eqn. (3.5).

For the k_{th} line segment $\overline{A_{k-1}A_k}$, the electrostatic force is obtained by integrating the differential electrostatic force $\Delta F_e(x)$ for $x = 0$ to $x = L/N$

$$F_k = \int_o^{L/N} \frac{\varepsilon_o V^2 W}{2\left(D - \overline{B_{k-1}C_{k-1}}\right)^2} dx\, y_k$$

$$= \frac{\varepsilon_o A V^2}{2N} \frac{1}{(D - y_{k-1})(D - y_k)} \tag{4.17}$$

Total electrostatic force is the sum of those acting on all N beam segments

$$F_{NP} = \sum_{k=1}^{N} F_k = \frac{\varepsilon_o A V^2}{2N}\left[\frac{1}{D(D-y_1)} + \frac{1}{(D-y_1)(D-y_2)} + \ldots + \frac{1}{(D-y_{N-1})(D-y_{Tip})}\right] \tag{4.18}$$

where y_k's are given in Eqn. (4.16)

However, the triangle model was found adequate for the accelerometer design and was used in this work.

4.3 Threshold Acceleration Analysis of Triangle Model

In the triangle model, the electrostatic force given in Eqn. (4.7) is not constant but changes with the deflection of the beam. By equating this electrostatic force to the restoring force given in Eqn. (3.9), voltage expression which relates the deflection y_{Tip} and the voltage required to hold the beam at the deflection y_{Tip}, can be obtained.

$$V = \sqrt{\frac{4ET^3D}{3\varepsilon_o L^4} y_{Tip}(D - y_{Tip})} \tag{4.19}$$

The threshold voltage is obtained by taking the derivative of V with respect to y_{Tip}. From Eqn. (4.19),

$$\frac{dV}{d(y_{Tip})} = \sqrt{\frac{ET^3D}{3\varepsilon_o L^4}}\left[\sqrt{\frac{(D - y_{Tip})}{y_{Tip}}} - \sqrt{\frac{y_{Tip}}{(D - y_{Tip})}}\right] \tag{4.20}$$

By letting $\frac{dV}{d(y_{Tip})} = 0$, the resulting expression has a maximum value at $y_{Tip} = D/2$, and is given by

$$V_{th} = \sqrt{\frac{ET^3D^3}{3\varepsilon_o L^4}} \tag{4.21}$$

It is worth comparing the threshold voltages of parallel plate model and triangle model in Eqns. (3.12) and (4.21). The parallel plate model requires less voltage than the triangle model to reach the threshold by the factor of $4\sqrt{3}/9$. This is because the parallel plate model overestimates the electrostatic force exerted on the beam and hence requires less voltage than the triangle model.

The threshold distance for an applied voltage V can be obtained from Eqn. (4.21)

$$D_{th} = \left(\frac{3\varepsilon_o L^4 V^2}{ET^3}\right)^{1/3} \tag{4.22}$$

With an original beam spacing D and beam deflection y_{Tip}, the threshold distance can be rewritten as

$$(D - y_{Tip}) = \left(\frac{3\varepsilon_o L^4 V^2}{ET^3} \right)^{1/3} \tag{4.23}$$

Substituting Eqn. (3.6) into (4.23) gives the threshold acceleration needed to make the beam close under an applied voltage

$$a_{th} = \frac{D - \left(\frac{3\varepsilon_o L^4 V^2}{ET^3} \right)^{1/3}}{\left(3\rho L^4 / 2ET^2 \right)} \tag{4.24}$$

Analogous to the triangle model, threshold voltage and threshold acceleration for the 2-point piecewise linear model can be obtained.

CHAPTER 5

ACCELEROMETER DESIGN

5.1 Accelerometer Geometry

The basic design of the accelerometer is dictated primarily by two facts: functionality and compatibility with standard IC processing techniques. Functionally, the beam must be free to bend all the way across the gap between two electrodes and make a contact with the bottom electrode.

Compatibility with standard IC processing techniques can be maintained by selecting materials which are themselves compatible, and also by designing the accelerometer in such a way as to ensure that standard processes can be used with little or no modification. The latter of these conditions dictates that the accelerometer be relatively planar in design, and that the dimensions of the device be within the limits imposed by current photolithographic and etching techniques. Since IC processing does not allow for movable structures, the accelerometer must be fabricated with the beams attached to the substrate, and the beams subsequently released. These constraints dictate that the beam must be fabricated on a sacrificial layer, which must then be dissolved away in a wet chemical etch process. In order for the beams of the accelerometers to be free to bend and make contacts with the bottom electrodes, the design of the beams must be considered carefully.

The cantilever has several attractive features as a threshold accelerometer design. Its output is a linear function of acceleration, eliminating the need for calibration curves, and it is inherently sensitive to accelerations in only one direction. Further, the response per unit acceleration is a function of the dimensions of the beam and the mass loading it.

Three distinct designs for the beams are possible to satisfy the above requirements: double-ended bridge type, weighted cantilever beam, and uniform cantilever beam (See Fig. 5.1). The bridge type is more robust than a cantilever beam while it needs a larger

area to achieve a given sensitivity. Table 5.1 shows the deflections of these three types of beams. In order to obtain the same deflection, the bridge type needs a beam length of $(48/5)^{1/4}$ times longer than that of the uniform cantilever beam (UCLB). It also requires additional space for the other anchor.

The weighted cantilever beam (WCLB) requires an additional mask to define thicker proof mass area while it shows better sensitivity than the UCLB. Another difficulty, associated with this design, is that the sacrificial layer is much thicker than that of UCLB. WCLB can be built with a wider proof mass rather than a thicker one. It requires etch holes to release the beam, and the beam of this design tends to move tortionally, i.e., one side along its width bends down while the opposite side bends up

5.2 Consideration of Dimension and Material

As given in Eqn. (4.22), the threshold acceleration for a given device is a function of variable parameters. These parameters are largely categorized into three groups: material property, device dimension and external excitation. Typical values of these parameters are illustrated in table 5.2.

Once the beam material is determined, the material properties such as Young's modulus and density are fixed. The tantalum silicide used as beam material in this research has a Young's modulus and density of 155 GPa and 9080 kg/m^3, respectively. Among device dimensions, beam width does not play any role in determining threshold acceleration, but the beam must be wide enough to stand against the external excitation. When the beam becomes wider, a longer etch time for the sacrificial layer underneath is required, possibly damaging the beam structure. If there is no etch hole on the beam structure, a width of less than 10 μm is preferable. The reason for this is that the etch rate, of $TaSi_2$ and spin on glass (SOG) in the 7:1 buffered oxide etch (BOE), is approximately 200 Å/min. and 12000 Å/min., respectively. It takes 5 minutes to release etch the SOG layer underneath a 10 μm wide beam, and during this length of time $TaSi_2$ beam will also

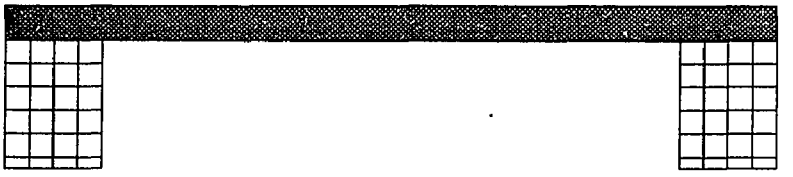

(a) Double-ended bridge

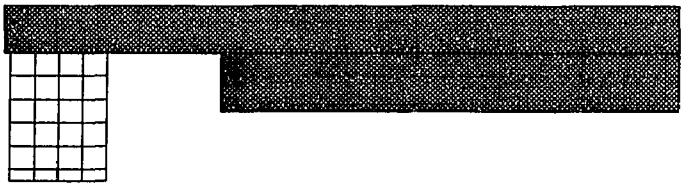

(b) Weighted cantilever beam

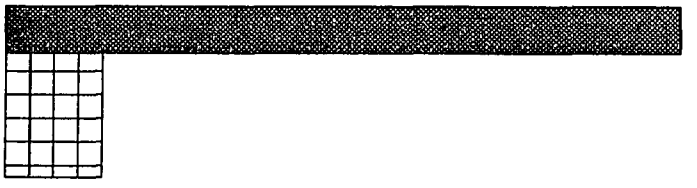

(c) Uniform cantilever beam

Figure 5.1 Three distinct beam designs for accelerometers: (a) Double-ended bridge; (b) Weighted cantilever beam; (c) Uniform cantilever beam

Table 5.1 Deflections of beams

Beam Type	**Deflection of Beams**
Cantilever Beam 	$y = \frac{qx^2}{24EI}(6L^2 - 4Lx + x^2)$ $y_{Tip} = \frac{qL^4}{8EI}$
Weighted Cantilever Beam 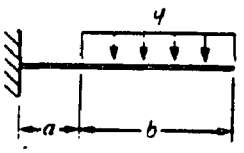	For $0 \le x \le a$ $y = \frac{qbx^2}{12EI}(3L + 3a - 2x)$ For $a \le x \le L$ $y = \frac{q}{24EI}(x^4 - 4Lx^3 + 6L^2x^2 - 4a^3x +$ $y_{Tip} = \frac{q}{24EI}(3L^4 - 4a^3L + a^4)$
Double-ended Bridge 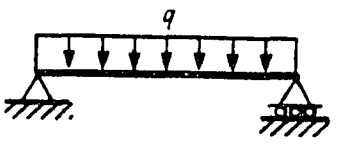	$y = \frac{qx}{24EI}(L^3 - 2Lx^2 + x^3)$ $y_{Mid.} = \frac{5qL^4}{384EI}$

where q is a uniformly distributed load per unit length

Table 5.2 Parameters which determine the threshold acceleration and their typical values

Group	Parameter	Symbol	Typical Value
Material property	Young's Modulus Density	E ρ	155×10^9 (Pascal) 9.08×10^3 (kg/m^3)
Device dimension	Gap distance Beam thicknesws Beam length Beam width	D T L W	0.5, 1.0, 1.5 μm 4000, 5000, 6000 Å 30 - 126 μm ~ 10 μm
External excitation	Applied voltage Acceleration	V a	Less than 10 V 50 - 100 g
Environment	Dielectric constant	ε_o	8.8542×10^{-12} (F/m)

be etched about 1000 Å. The gap between the two electrodes is determined by the thickness of the sacrificial layer. In this research, commercially available SOG is chosen as a sacrificial layer material, because it dissolves much faster than low pressure chemical vapor deposition (LPCVD) oxides in solutions containing hydrofluoric acid (HF), the primary wet etchant of silicon dioxide. It gives a film thickness of 5000 Å per coating. Up to three coatings (1.5 μm) gives a fairly good thickness uniformity across the wafer. Details on SOG are described in section 5.3. The thickness of the beam is determined by the deposition time of $TaSi_2$. In this research, accelerometers of 4000 Å, 5000 Å and 6000 Å thick were fabricated. The length of the beam is decided by the mask pattern, and 30 μm to 126 μm were chosen as beam length. Fig. 5.2 shows graphs of threshold accelerometer versus beam length calculated using the triangle model when the applied voltage is 1.5 volts for the typical material parameter values of table 5.2. Curve A represents the beam of $T = 0.4\mu m$ and $D = 0.5\mu m$, while curve B is for $T = 0.6\mu m$ and $D = 1.5\mu m$. The x-interception is about 59 μm for an accelerometer of the curve A. This means that the accelerometer of curve A is ready to snap shut with no acceleration when the beam length reaches 59 μm, provided the applied voltage is 1.5 volts. The y-intercept of the curve B is about 414g. This means the device of curve B would not snap shut with an acceleration less than 414g when 1.5 volts is applied across the gap. The area between curves A and B represents the threshold acceleration which can be obtained by the devices with parameters in table 5.2 when the applied voltage is 1.5 volts. Fig. 5.3 shows graphs of threshold acceleration versus beam length with applied voltage as a parameter. The device dimension in this graph is fixed as $T = 0.5\mu m$ and $D = 1\mu m$. Curves A and B represent the device operations with the applied voltages of 5 volts and 1 volt, respectively. The x-interception of curve A is 65 μm, which means that this device is ready to snap shut when it has a length of 65 μm, even though there is no acceleration imposed on it, provided that the applied voltage is more than 5 volts. The y-interception of curve B

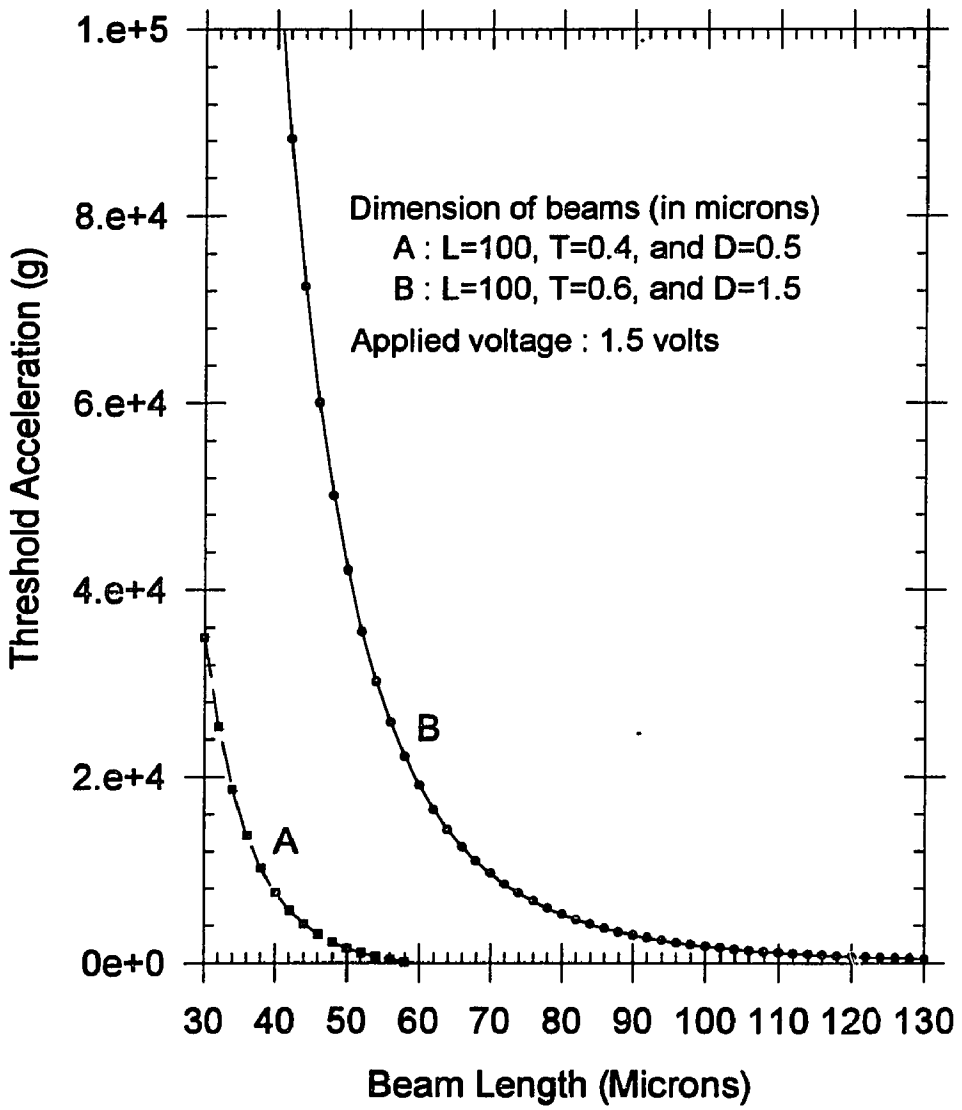

Figure 5.2 Threshold acceleration versus beam length: (A) For T=0.4 microns and D=0.5 microns; (B) For T=0.5 microns and D=1.5 microns

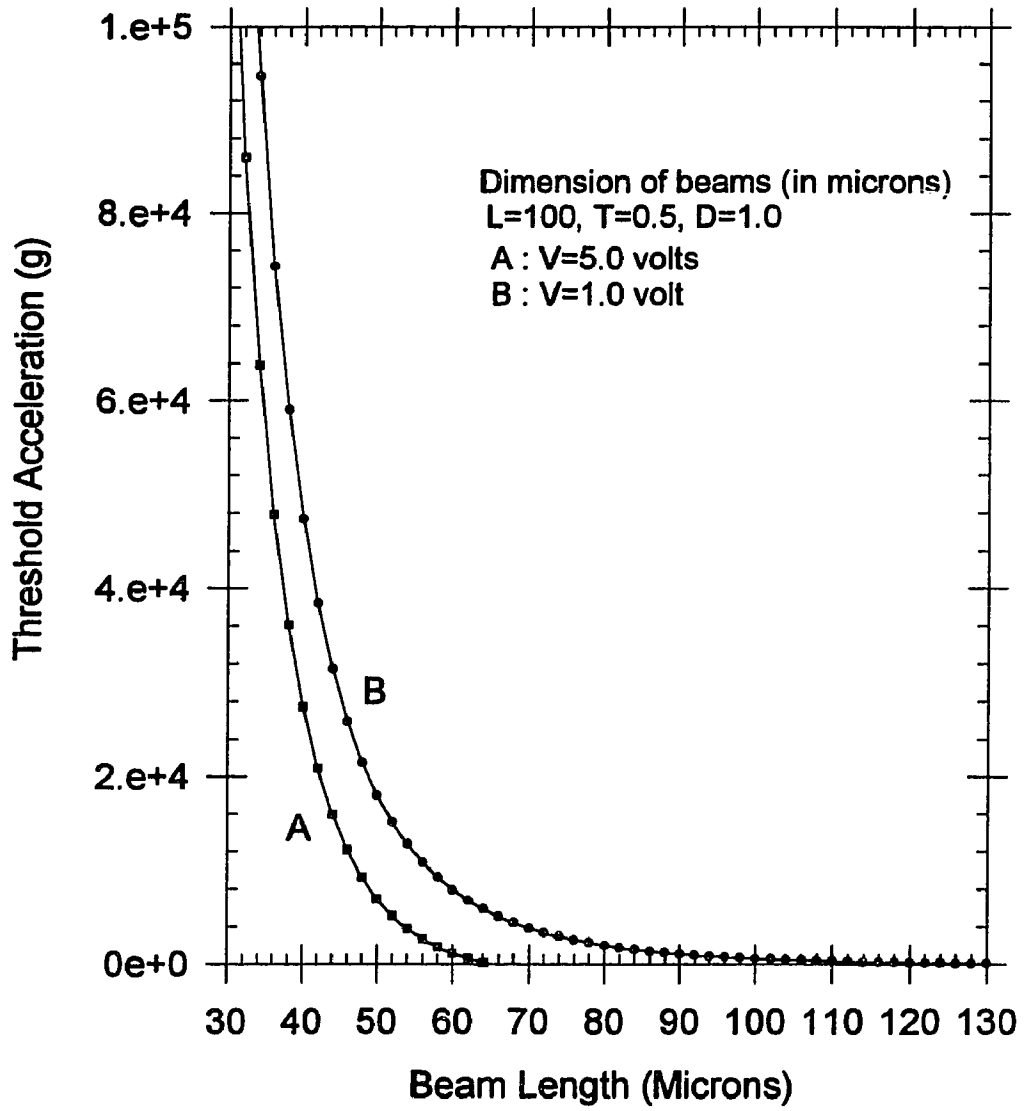

Figure 5.3 Threshold acceleration versus beam length with applied voltage as a parameter: (A) For V=5 volts; (B) For V=1 volt

is 70g, which means this device, with an applied voltage of 1 volt, would not snap shut with an acceleration less than 70g.

5.3 Surface Micromachining

The two primary techniques for fabricating microstructures, which employ essentially standard IC technologies, are surface micromachining and bulk micromachining, which now often incorporates wafer-to-wafer silicon fusion bonding. Surface micromachined structures utilize only deposited and patterned thin films while bulk micromachined structures also exploit the substrate mechanically, beyond its obvious use as a support. In both techniques, the silicon substrate is available for device integration but rarely used as such because of fabrication complexity, thermal and passivation requirements, and low yields.

A primary ingredient of surface micromachining involves the selective removal of a sacrificial layer near the completion of the process, i.e. the release, to produce free-standing or, in the case of cantilever beam, freely moving beam structures. Ideally, the removal of this sacrificial layer would not affect the other layers in the structure either by etching them, leaving a residue on them that might promote sticking, or pulling them together during the etching or drying process. Surface micromachined structures, and in particular the present cantilever beam accelerometers, do not require substrates. For convenience, silicon is used because it is a cheap, readily available, clean, mechanically stable support for the microfabricated structures. For cantilever beam accelerometer fabrication, the semiconducting nature of the silicon is even disadvantageous, requiring the formation of a sophisticated dielectric layer to separate devices from one another.

5.3.1 Sacrificial Layer Technique

Sacrificial layer techniques have been used in surface micromachining to fabricate free standing structures such as cantilevers, bridges and membranes. Fan [80] showed an

example to demonstrate the sacrificial layer technique. Fig. 5.4 shows the process sequence of fabricating a microbridge using the surface micromachining technique. First, a sacrificial layer is deposited on top of isolation layers. A structural layer is deposited and patterned. Finally, the sacrificial layer is removed by a selective etchant, and the bridge becomes free standing. The etchant used must have a high selectivity between the structural and the sacrificial layer, and between the isolation and the sacrificial layers. If the substrate can resist the etchant during sacrificial layer etching, no isolation layers will be needed. To shorten the undercut etch time for large structures, apertures can be used to provide etchant access [81]. The sacrificial layer technique is a single-sided process that obtains precise dimensional control by controlling deposition and lithography. Also, it provides many possible choices for material/etchant combinations as long as the selectivity requirements given in Eqn. 2.1 are fulfilled, as shown in Fig. 5.5. The following section refers to the possible material combinations and their characteristics for building free standing structures using the surface micromachining technique.

5.3.2 Material

The sacrificial layer technique of surface micromachining requires a materials system composed of films with compatible, yet complementary characteristics. The surface micromachining materials system described by Howe [82] relies on the excellent etch resistance of silicon to hydrofluoric acid (HF), the primary wet etchant of silicon dioxide. Electrically insulating and resistant to HF attack, silicon nitride was subsequently introduced to complement the electrical conductivity of the polysilicon. Silicon nitride is also standard to the IC fabrication process because of its oxygen diffusion resistance and hence its use in local oxidation of silicon (LOCOS) processes and, to a lesser extent, its passivation qualities [83]. Stoichiometric silicon nitride (Si_3N_4) has been used for passivating silicon devices because it serves as an extremely good barrier to the diffusion of water and sodium. The purpose of nitride films, in the fabrication and structure of

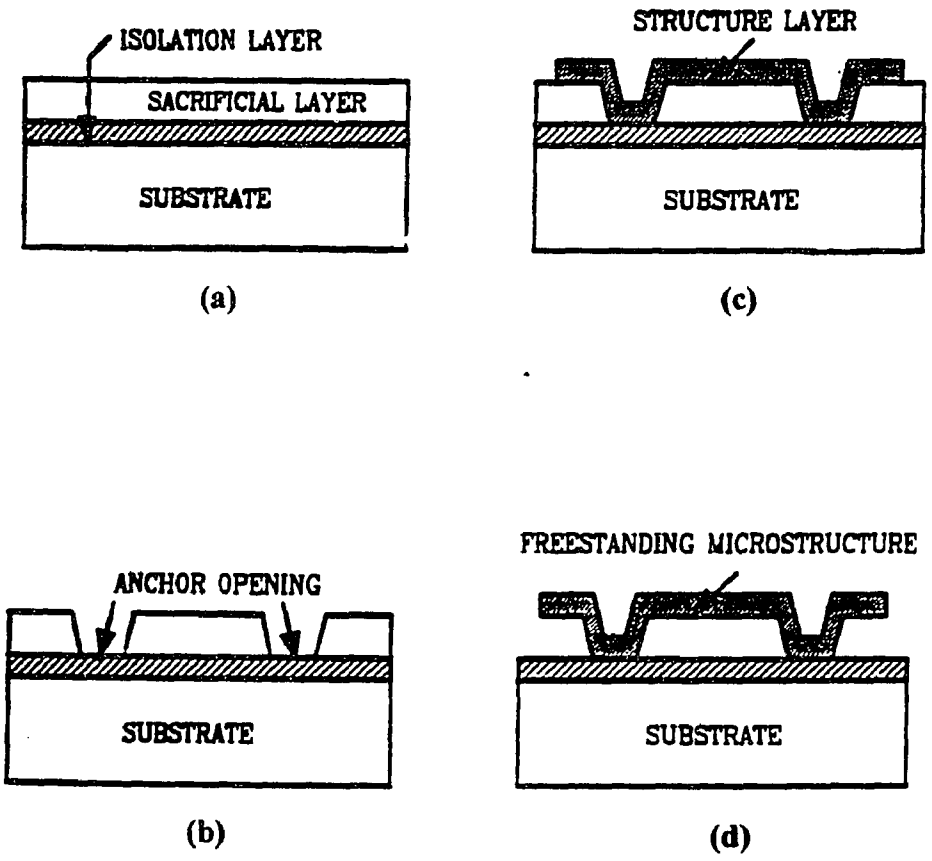

Figure 5.4 Sacrificial layer techniques used in the surface micromachining to fabricate a microbridge: (a) Deposition of sacrificial layer; (b) Etch of sacrificial layer; (c) Deposit structural layer; (d) Sacrificial layer release etch [80]

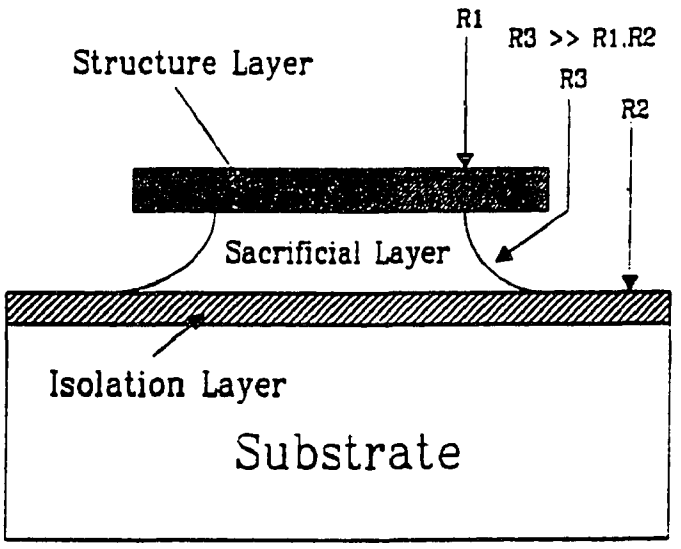

Figure 5.5 Etch rate selectivity requirements for the sacrificial layer micromachining technique [80]

cantilever beam accelerometers, differs entirely from that of ICs. Nitride, in IC processes, provides the oxygen diffusion barrier necessary for LOCOS and is subsequently stripped, usually in a wet, boiling phosphoric acid/water solution [84]. Nitride, in the cantilever beam accelerometers, is the primary insulation layer which isolates the stators from the substrate. Additional compliments of materials could have been similarly chosen, such as, tungsten and oxide [85], molybdenum and aluminum [86] and even epitaxial layers of GaAs and AlGaAs [87], although they are less understood, often uncharacterized, and frequently have worse characteristics than the polysilicon/nitride/oxide system.

In this research, tantalum silicide ($TaSi_2$) rather than polysilicon was chosen as a structural material for several reasons. It is a low resistive material compared with polysilicon (approximately an order of magnitude lower); it is compatible with standard IC processing technique; and most importantly, it has very high electromigration activation energy [88] which can prevent a possible welding problem associated with the metal cantilever beam mechanical switch. If tantalum silicide is to be pursued as a micro electromechanical material, it is necessary that the release etch selectivity of oxide to tantalum silicide be increased. This can be done by increasing the etch rate of the oxide. A spin-on-glass (SOG) has an etch rate significantly higher than that of thermal oxides. The problems of SOG are that the maximum thickness for a single coating is typically less than 1μm, and that the SOG tends to planarize. It makes sharp corners become rounded off very much like photoresist. The cantilever beam accelerometers, in this research, have beam lengths much longer than the thickness and width of the beam, and the problems associated with round-off are not critical. The thickness could be increased to the desired value by using several layers of SOG spun on sequentially, and the planarity of the substrate could be maintained by subsequently etching back the SOG.

Because of the specialized use of the three layers, tantalum silicide, nitride, and SOG, in the surface micromachining process, these materials should be optimized differently for the sensor/actuator devices than for the integrated circuits. The mechanical properties of

IC materials are of secondary concern to IC performance. Consequently, the development and characterization of specialized forms of these materials - tantalum silicide as a substitute for polysilicon, SOG as a substitute for undoped oxide or phosphosilicate glass (PSG) and silicon nitride are important for microstructure development.

CHAPTER 6

TANTALUM SILICIDE AS A MICROMECHANICAL MATERIAL

6.1 Background of Silicides

The recent interests in micro electromechanical systems necessitated a closer look at the transition-metal silicides due to their thermodynamics, electrical and mechanical properties, and their stability at very high temperatures. Silicides are used to integrate the micromechanical structures and the interfacing electronic circuits in the same chip. Metal silicides have attracted scientific curiosity and attention since Moissan developed the electric furnace [89]. He was possibly the first to systematically prepare various silicides near the turn of the century. Investigations concerning silicides [90,91] can be grouped into the following major categories: (1) studies stimulated by the high temperature stability of many refractory silicides, (2) studies aimed at understanding the physical properties of silicides in terms of the electronic and crystal structure of the elements and compounds, (3) studies of silicides as Shottky barriers and ohmic contacts in the integrated circuit technology, and finally, and more recently, (4) studies of silicides as the low resistivity metallization for gates and interconnects.

The primary thrust of very large scale integration (VLSI) has resulted in devices that are smaller (large packing density and hence increased complexity on the chip), faster, and consume less power. The continued evolution of smaller and smaller devices has aroused a renewed interest in the development of new metallization schemes for low resistive gates, interconnections, and ohmic contacts. This interest in new metallization arouses because as the device sizes are scaled down, the linewidth gets narrower and the sheet resistance contribution to the RC delay increases. The averages of future scaling are offset by the interconnect resistance at the gate level with the currently available polysilicon sheet

resistance of 30 to 60 Ω/□. Aluminum, tungsten and molybdenum are notable among the metals proposed for gate and interconnect metallization. The use of aluminum, however, requires all postgate processing of the devices be limited to very low temperatures, preferably below 500°C. The use of the refractory metals tungsten and molybdenum requires complete passivation of these metals from oxidizing ambients, deposition by means that will not lead to unwanted traps in the gate oxide, and reliable etching of the metals for pattern generation. The uncertainties associated with the stability of these metal films have led to a search for alternatives.

The silicides have attracted attention because of their low and metal-like resistivities and their high temperature stability. The use of silicides, with resistivity about one-tenth (or lower) of the polysilicon, will certainly improve the speed of the circuits. Silicides are also attractive for gate and interconnection metallization for the following reasons: expected higher electromigration resistance, and the possibility of forming silicides directly on the polysilicon, thus preserving the basic polysilicon MOS gate, while decreasing the resistance.

6.2 Preparation of Tantalum Silicide

Silicide films can be deposited by cosputtering, coevaporation, and CVD techniques. Deposition of silicide films by sputtering from a composite target has the advantage of producing high quality films with high throughput. It has been extensively used in molybdenum silicide and tungsten silicide polycide gates in very large scale integrations. The reason for this is that high quality films can be deposited with high throughput. In this research, tantalum silicide films were deposited by Varian 3125 magnetron sputtering system from a composite target of $TaSi_{2.4}$.

All substrates were scrubbed in a substrate cleaner (Ultra t Equipment Co. Model 602) to remove any particle bonded on the surface of the wafers and piranha cleaned (P-clean, 5:1 H_2SO_4:H_2O_2) for 10 minutes at 110°C to remove any organic residues on the

wafers. Then the wafers were rinsed in hot deionized (DI) water for 10 minutes followed by cold DI water rinse for 5 minutes In addition, the silicon wafers were dipped into a 100:1 H_2O:HF mixture immediately before they were loaded into the sputtering chamber to etch off the native oxide after the acid cleaning. The sputter chamber was pumped to a vacuum of less than 8 x 10^{-7} Torr before being back filled with argon gas. The sputtering was done at an argon pressure of 3 mTorr. The deposition parameters are given in table 7.7. The thickness of the silicide film was measured by a surface profilometer over a step etched in the film deposited on a silicon wafer.

After deposition, the silicide films were annealed at rapid thermal process system (RTM 2016) for 30 seconds at the temperatures of 500, 600, 700, 800 and 950°C. These annealed films were then used to measure the resistivity in a four-point probe system and also to measure Young's modulus and hardness in a Nanoindenter.

6.3 Properties of Tantalum Silicide

The recent interests in micro electromechanical systems necessitated a closer look at the transition-metal silicides due to their thermodynamics, electrical and mechanical properties, and their stability at very high temperatures. Among the transition-metal silicides, tantalum silicide has very attractive electrical and micromechanical characteristics. It is a low resistive material compared with polysilicon (approximately an order of magnitude lower). It has a very high electromigration activation energy which is 1.7 eV [88] (this is almost three times higher than aluminum of which electromigration activation energy is about 0.6 eV), and this eliminates the reliability problem caused by electromigration. The hardness of $TaSi_2$ is significantly higher than that for many other silicides. It is compatible with standard IC processing techniques, and has become a standard material in MOS processing technology [92]. Listed below are some of the characteristics of the tantalum silicide which make it favorable for the micro sensors and actuators applications.

(1) Good adhesion on silicon, silicon nitride and oxide

(2) Low resistivity : 35 - 55 μΩ-cm

(3) No reaction with aluminum up to 500 °C

(4) As hard as steel : hardness = 1407 kg/mm^2 (cf : steel = 1500 kg/mm^2)

(5) Thermally stable : TCE = 8.8 ppm/°C

(6) Insoluble in $H_2SO_4 + H_2O_2$ mixture

(7) Good etch resistance in HF, primary wet etchant of SiO_2 (i.e. sacrificial layer)

(8) Very high electromigration activation energy : 1.7 eV (cf : Al ~ 0.6 eV) [88]

(9) Hard to form a native oxide layer [93]

6.3.1 Resistivity

The resistivity of silicides is the single most important criterion in considering them for metallization in integrated circuits. Investigations of various metal - silicon systems have resulted in silicide resistivities that are routinely obtainable [94]. Table 6.1 lists the resistivities of various silicides [95] formed by reacting this metal film with mono- or polycrystalline silicon or by cosputtering and sintering a mixture of metal and silicon. Tantalum silicide, as shown in table 6.1, has a very low resistivity, just slightly higher than the lowest resistivity of titanium silicide ($TiSi_2$). Even molybdenum silicide ($MoSi_2$) and tungsten silicide (WSi_2) have higher resistivities than tantalum silicide.

Resistivities of tantalum silicide films deposited from a $TaSi_{2.4}$ composite target were measured. Films of 6000Å thick were deposited by sputtering, from a composite target, in a Varian 3125 magnetron sputtering system. The deposition parameters are given in table 7.7. Film resistivities were measured by the 4 point probe method using FPP-5000 of Veeco Instruments Inc. Resistivity of the as-deposited films at 300°C in the sputtering chamber was 272.6 μΩ cm. Films were annealed at RTP for 30 seconds for temperatures of 500, 600, 700 800 and 950°C. The variation of film resistivity with annealing

Table 6.1 Resistivities of various silicides [95]

Silicide	Formed by starting from	Sintering Temperature (°C)	Resultant resistivity (μΩ-cm)
$TiSi_2$	Metal on polysilicon	900	13-16
	Cosputtered	900	25
$TaSi_2$	Metal on polysilicon	1000	35-45
	Cosputtered alloy	1000	50-55
$MoSi_2$	Metal on polysilicon	1100	~90
	Cosputtered alloy	1000	~100
WSi_2	Cosputtered alloy	1000	~70

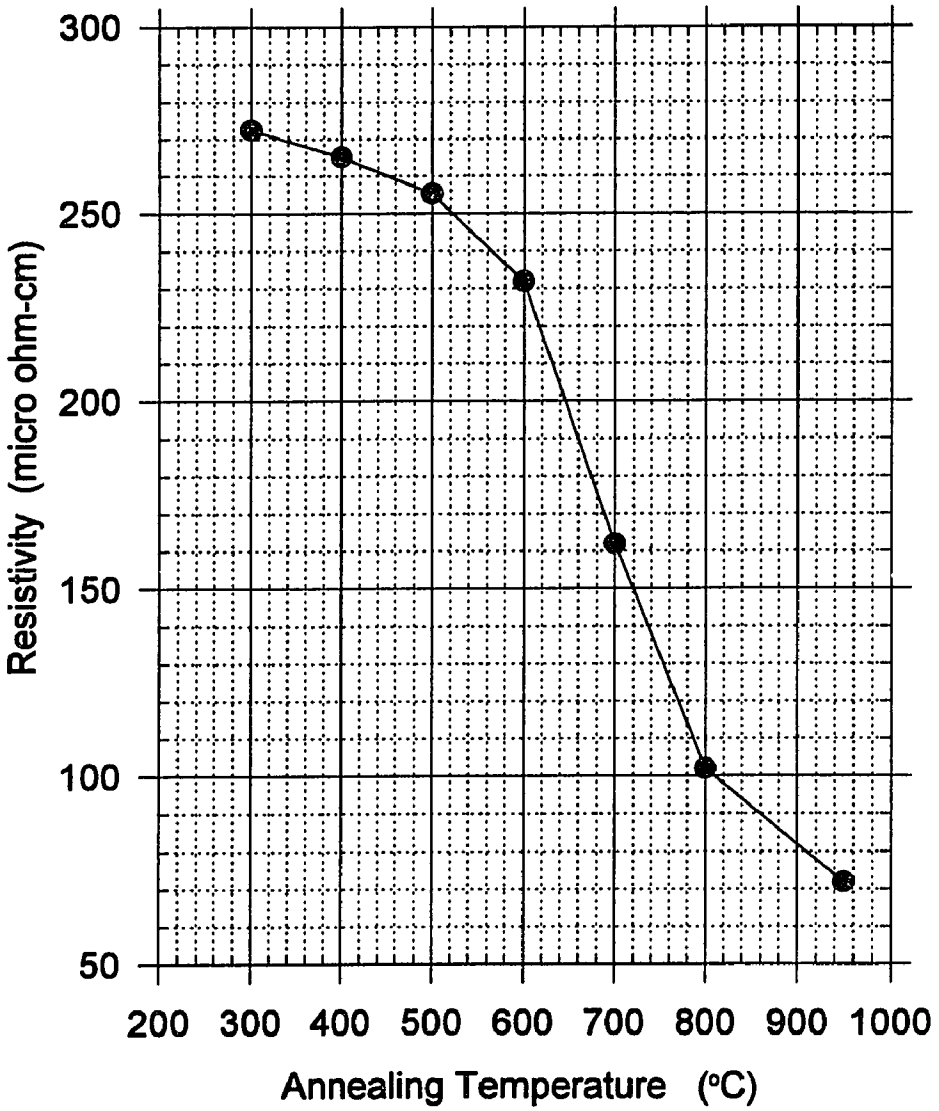

Figure 6.1 Resistivity of tantalum silicide thin film versus annealing temperature, where annealing was performed in RTP for 30 seconds

temperature is shown in Fig. 6.1. Resistivity decreased rapidly at 600°C and slowly above 800°C. A resistivity of 72 μΩ cm at 950°C is very close to the reported value [96].

6.3.2 Crystalline Structure Analysis

The crystalline structure of the films was examined by X-ray diffractometer (XRD; 30 KV, 20 mA) using Cu K_α radiation. The effect of post-annealing treatment on XRD patterns of tantalum silicide thin film is presented in Fig. 6.2. The films were of the same thickness (6000Å) and were annealed in a rapid thermal process (RTP) at the temperatures of 500, 600, 700, 800, and 950°C for 30 seconds. As-deposited tantalum silicide films produced X-ray diffraction spectra showing no evident $TaSi_2$ or other peaks as shown in Fig. 6.2 (a). The formation of a broad peak in the films annealed at temperature of 500°C shows that 2θ is around 25° as shown in Fig. 6.2 (b). Films annealed at temperatures above 500° C exhibit the crystalline hexagonal $TaSi_2$ had formed as shown in Figs. 6.3 (a), (b) and (c). Typical diffraction peaks of hexagonal structure such as (101), (102), (111), (200), and (112) orientation arise completely in all $TaSi_2$ films. It seems that the intensity of each peak in XRD patterns increases as the annealing temperature increases. It is known [97] that the density of hexagonal $TaSi_2$ is 9.08 g/cm^3. Table 6.2 shows the crystal structure of the tantalum silicide family.

6.3.3 Measurement of Young's Modulus and Hardness

Great strides have been made over the past few years in the development of techniques for probing the mechanical properties of materials on the submicron scale [98]. The advances have been made possible by the development of instruments that continuously measure force and displacement as an indentation is made [99]. The indentation of load-displacement data thus derived can be used to determine mechanical properties even when the indentations are too small to be imaged conveniently. The two mechanical properties measured most frequently, using load and depth sensing indentation techniques, are the

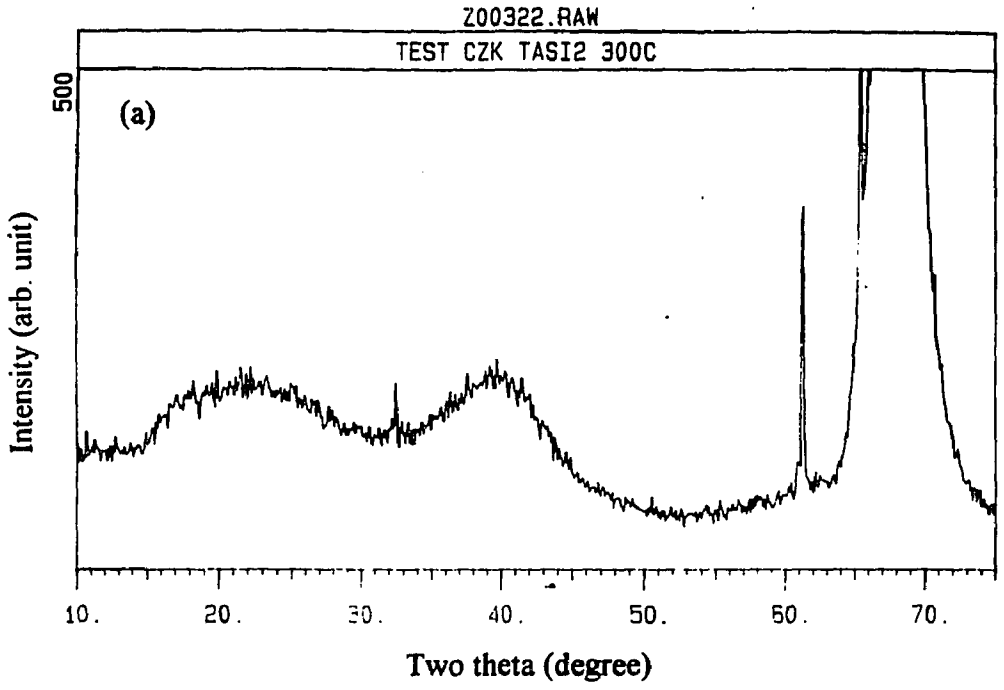

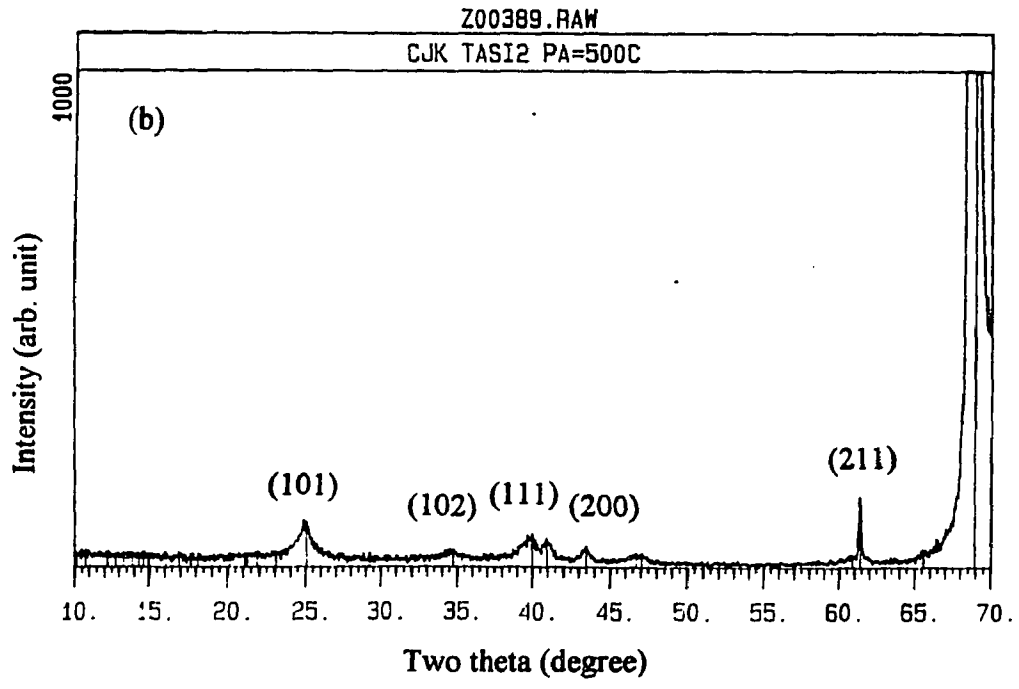

Figure 6.2 XRD patterns of $TaSi_2$ thin films: (a) As-deposited film at 300°C; (b) Film annealed at 500°C for 30 seconds in RTP

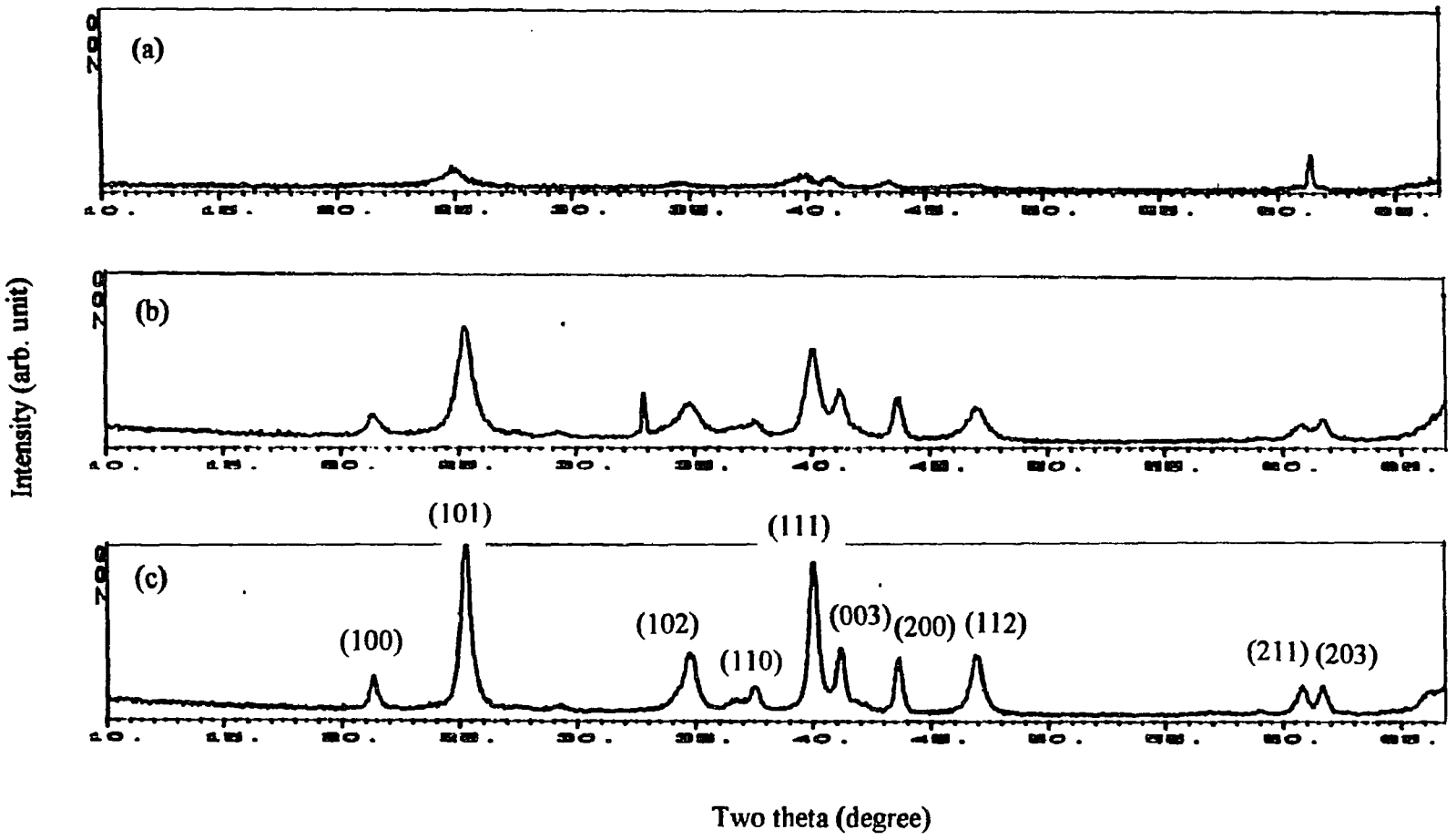

Figure 6.3 XRD patterns of $TaSi_2$ thin films as a function of annealing temperature, where annealing was performed in RTA for 30 seconds; (a) Annealed at 500°C; (b) Annealed at 700°C; (c) Annealed at 950°C.

Young's modulus E and the hardness H. A schematic representation of load versus indenter displacement curve is shown in Fig. 6.4. The initial increase in this curve represents the observed displacement due to an increased loading at a constant rate from 0 to the maximum loading P_{max}. The second segment of the curve represents the unloading at the same constant rate down to 20% of maximum load. From that latter segment, the deformation contact depth h_p and elastic recovery depth h_e can be measured. A linear least square fit of the upper segment extrapolated down to 0 load yields the value of h_p. The difference between the maximum displacement and h_p yields the value of h_e. The hardness is obtained at the maximum displacement using the formula

$$H = P / A \tag{6.1}$$

where P is the applied load and A is the contact area calculated from the known geometry of the indenter.

$$A = 24.56h_p^2 + 225.94h_p^{3/2} + 519.61h_p \tag{6.2}$$

Table 6.2 Crystal structure of the tantalum silicide family [21]

Silicide	Structure	Lattice constant (Å)	Density (g/cm^3)
$TaSi_2$	Hexagonal	a=4.7821 c=6.5695	9.08
Ta_2Si	Tetragonal	a=6.175 c=5.039	13.544
Ta_5Si_3	Tetragonal	a=9.88 c=5.06	13.401

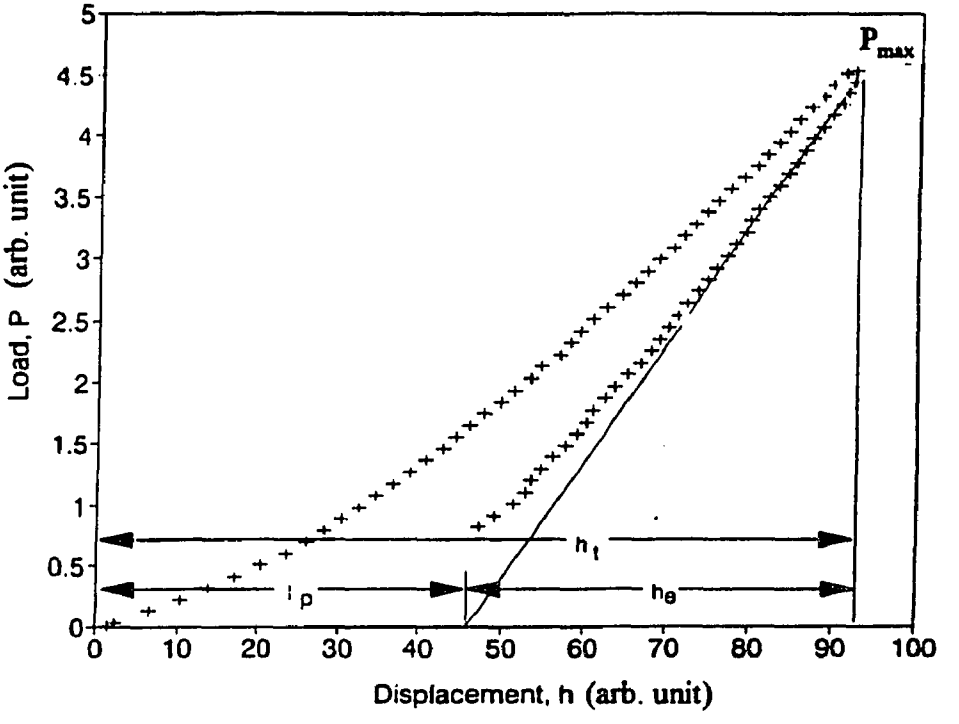

Figure 6.4 A schematic representation of load versus indenter displacement data for an indenter experiment. The quantities shown are P_{max} : the peak indentation load, h_f : the indenter displacement at peak load, h_p : the deformation contact depth, h_e : elastic recovery depth

Assuming that the area in contact remain constant during initial unloading and adopting Sneddon's solution [100] for the elastic deformation of an isotropic elastic material, the elastic modulus is obtained from the contact stiffness S, the slope of the unloading curve, given by

$$S = dP/dh = 2E_r\sqrt{A/\pi} \tag{6.3}$$

where h is the displacement of the indenter, and E_r is the composite modulus for the indenter/sample combination

$$E_r = \left[\frac{1-\nu_f^2}{E_f} + \frac{1-\nu_i^2}{E_i}\right]^{-1} \tag{6.4}$$

where E_f and E_i are Young's moduli for film and indenter, respectively, and ν_f and ν_i are Poisson's ratio for the film and the indenter, respectively. Since ν appears as a quadratic term and therefore represents only a small correction, we took $\nu_f = 0.3$, while the values for the diamond indenter E_i and ν_i were taken to be 1010 GPa and 0.213, respectively.

Figures 6.5 and 6.6 represent plots of hardness and Young's modulus, with error bars, as a function of annealing temperature. In both cases, no significant annealing temperature dependency are observed. The measured values for hardness and Young's modulus are 8 ± 1 GPa and 158 ± 17 GPa, respectively. All measurements were performed using a Nanoindenter (Nanoindenter is a registered trademark of Nano Instruments, Inc., Knoxville, TN) at NJIT's Thin Film Characterization Lab., a schematic illustration of which is shown in Fig. 6.7.

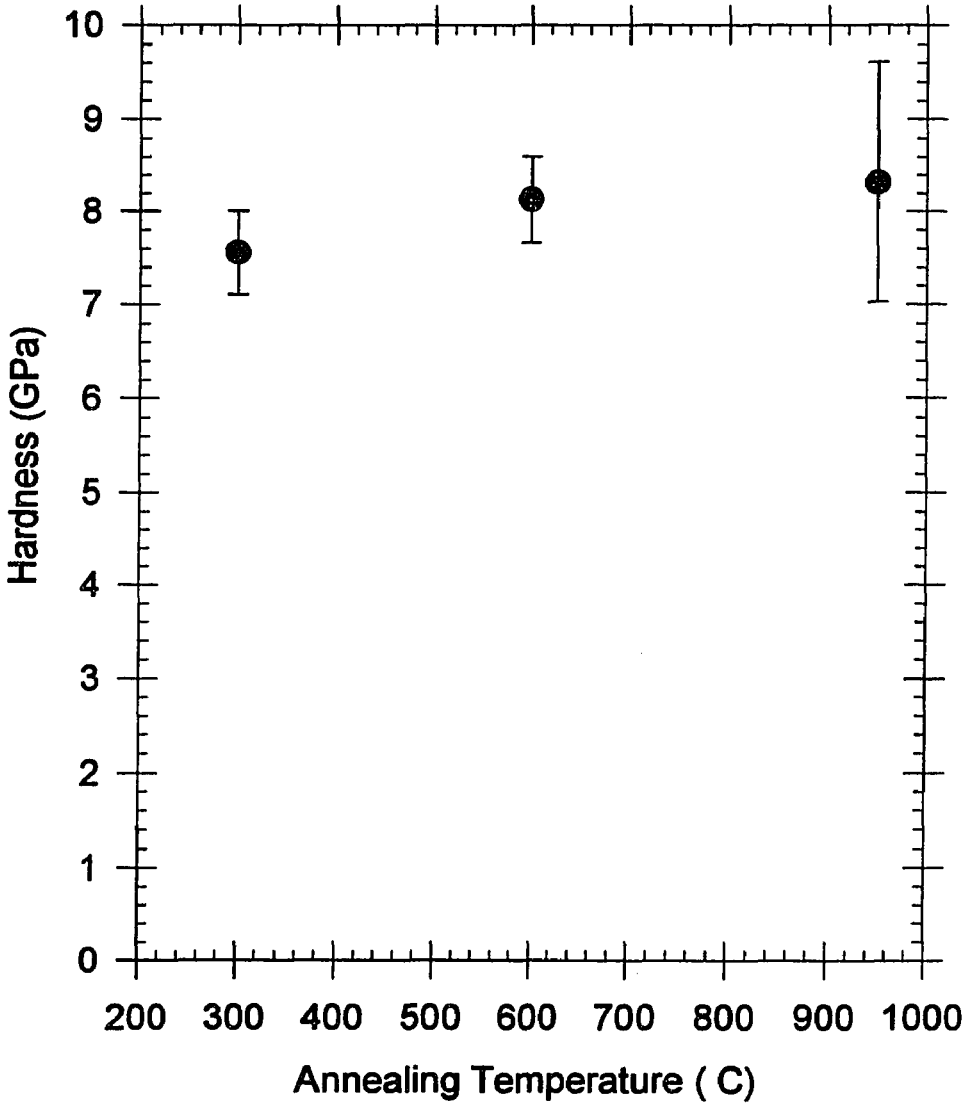

Figure 6.5 Hardness of tantalum silicide films as a function of annealing temperature, where annealing was performed in RTP for 30 seconds

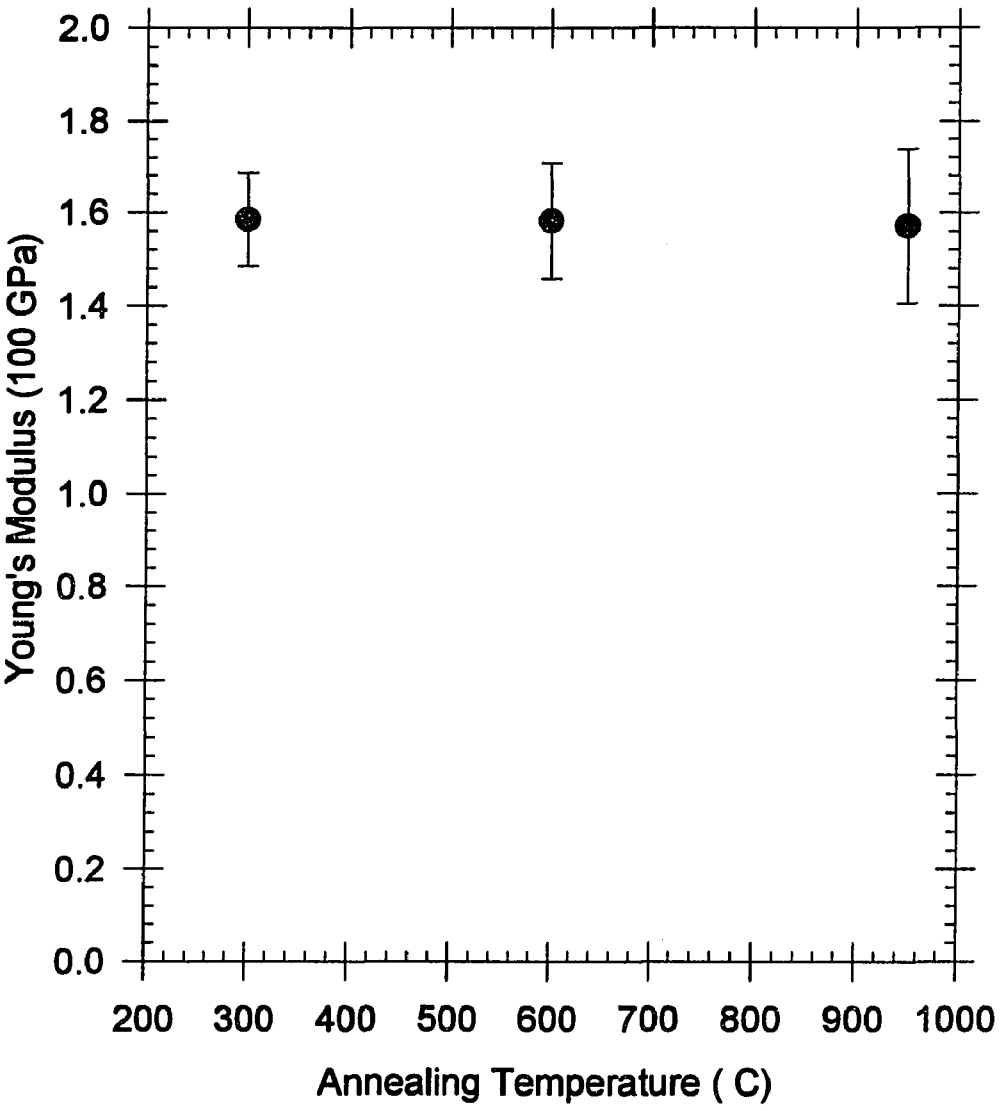

Figure 6.6 Young's modulus of tantalum silicide films as a function of annealing temperature, where annealing was performed in RTP for 30 seconds

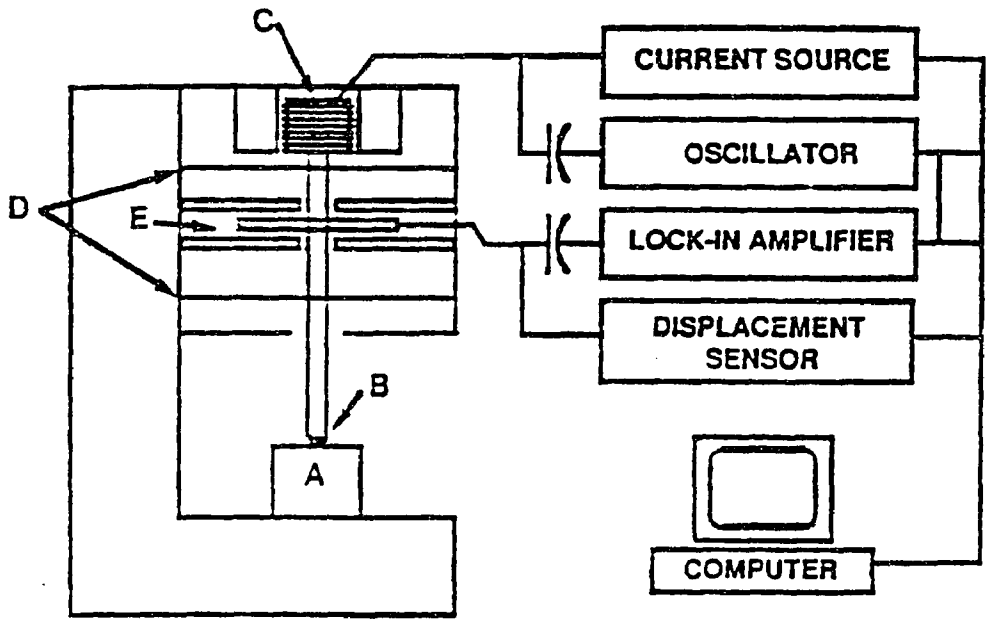

Figure 6.7 A typical schematic representation of the experimental apparatus used to perform the indentation experiments: (A) sample; (B) indenter; (C) load application coil; (D) indentation column guide spring; (E) capacitive displacement sensor [101]

CHAPTER 7

FABRICATION

The fabrication process, for the cantilever beam threshold type accelerometer, is described here with detail of the practical issues that need to be considered in the development of a robust tantalum silicide surface micromachined accelerometer fabrication process. All of the fabrication work was performed at the NJIT Microelectronics Research Center (NJIT MRC). The starting wafers were 5", <100>, n-type silicon wafers. A detailed process sequence is illustrated in Appendix A.

The process was a two-level tantalum silicide ($TaSi_2$) process, with silicon nitride used for the insulation between two electrodes, and spin on glass (SOG) as a sacrificial layer material. Excluding the metallization steps, only 2 masks and 4 photolithography steps were required: however both positive and negative photoresists must be utilized.

7.1 Isolation and Cavity Definition

Wafers were scrubbed in a substrate cleaner (Ultra t Equipment Co. Model 602) to remove any particle bonded on the surface of the wafers and then P-cleaned (piranha clean, H_2SO_4:H_2O_2=5:1) for 10 minutes at the temperature of 110°C to remove organic residues on the wafers. Then the wafers were hot (60-70°C) DI (deionized) water rinsed for 10 minutes, cold DI water rinsed for 5 minutes and spin dried.

Then a substrate isolation was performed and this was required to survive the final hydrofluoric acid (HF) release step of cantilever beams and to give the electrical insulation between the two electrodes of the accelerometer. This process uses approximately 300Å thick dry oxide and on the top of approximately 1700Å thick stoichiometric low pressure chemical vapor deposition (LPCVD) silicon nitride (Si_3N_4). After the furnace pre-clean in H_2O:HF=100:1 solution for 60 seconds (to remove about 70Å of native oxide layer

formed after P-clean) followed by hot DI water and cold DI water rinses and spin dry, wafers were put in the furnace at 950°C with 530 sccm of O_2 bubbler for 28 minutes. The process parameters of dry oxidation is given in table 7.1. The reasons for this dry oxide layer are first for use as an etch stop for the silicon nitride layer on the top of the oxide and second to release high residual tensile stress of the silicon nitride. Besides dry oxide is purer than thermal oxide and shows good adhesion on the silicon substrate. After oxidation, thickness was measured at 13 points on a wafer using the Leitz MPVSP film thickness measurement system. The average thickness and the standard deviation are 312Å and 22Å, respectively. Before deciding the thickness of silicon nitride, two important characteristics needed to be determined. First, the etch rate of the silicon nitride in 7:1 buffered oxide etch (BOE), also referred to as buffered hydrofluoric acid (BHF) was measured to determine the ability of silicon nitride to withstand the release etch. Next, the dielectric breakdown strength was measured to determine the thickness necessary for isolation between two electrodes. The etch rate of the LPCVD silicon nitride in 7:1 static BHF was approximately 6Å/min. Assuming a release time of 20 minutes, the amount of silicon nitride consumed would be about 120Å.

Dielectric breakdown strength was measured by patterning a 200×200 μm^2 aluminum pad on the silicon nitride film 500Å thick, and applying a positive voltage to the pad with the substrate ground. The average breakdown voltage for 5 points on the wafer was 48.7 V. This translates to a dielectric breakdown strength of 9.74×10^6 V/cm, which is very close to the 10^7V/cm given for stoichiometric LPCVD silicon nitride [102]. The thickness of as deposited silicon nitride is 1700Å and after 20 minutes etch in 7:1 BHF, the thickness of remaining silicon nitride is 1580Å. This means that the maximum voltage which can be applied across 1580Å thick silicon nitride is more than 150 V. In addition to the silicon nitride, there is dry oxide layer underneath it of which the dielectric breakdown strength is 10^7V/cm [103]. It is also known that silicon nitride of less than 2000Å thick

Table 7.1 Parameters for dry oxidation

Parameter	Value
Tube Temperature	950 °C
Bubbler Temperature	98 °C
O_2 Bubbler Flow	530 sccm
O_2 Main Flow	7.5 SLM[1]
Deposition Rate	11Å/minute

[1] standard litters per minute

Table 7.2 Deposition parameters for LPCVD silicon nitride

Parameter	Value
DCS[1] Flow	50 sccm
NH_3 Flow	120 sccm
Pressure	400 mTorr
Temperature	775 °C
Deposition Rate	52 Å/minute

[1] Dichlorosilane (SiH_2Cl_2)

shows no serious stress which leads to film cracking [104]. The deposition parameters are shown in table 7.2.

The next step is photolithography for the first mask level (mask #1) to define a cavity into the substrate. The purpose of this cavity is two fold. One is to enhance the planarity of the finished accelerometer as well as each processing step. Fig. 7.1 shows the difference in topography of two possible accelerometer designs. Fig. 7.1(a) shows a design with cavity which has planar topography compared to the other shown in Fig. 7.1(b) which has no cavity. The other purpose of this cavity is to use the backside of the substrate as an electrode of the accelerometer. NJIT's standard photolithography process was used. A summary of the coat, bake and develop conditions is given in table 7.3. Positive photoresist is coated and patterned to form a cavity into the substrate. This step consists of a positive resist masked plasma etch of silicon nitride layer in a sulfur hexafluoride (SF_6) based chemistry (the etch rate of silicon nitride is about 388Å/min.), another plasma etch of dry oxide in fluoroform (CHF_3 or Freon 23) and hexafluoroethane (C_2F_6 or Freon 116) based chemistry (the etch rate is about 487Å/min.) followed by the other plasma etch of silicon substrate in a SF_6 and monochloropentafluoroethane (C_2ClF_5 or Freon 115) based chemistry (the etch rate of silicon substrate is about 1572Å/min.). Silicon nitride and silicon substrate etches were done in a Drytek DRIE-100 plasma etcher, while dry oxide etch was done in a Drytek DRIE-102 plasma etcher. The geometry of the plasma etchers is such that 6 wafers can be etched simultaneously between 6 pairs of parallel plate electrodes. The difference between these two etchers is that DRIE-102 has much narrower gap between parallel plate electrodes than DRIE-100. Silicon nitride and dry oxide were time etched for 4.5 minutes and one minute, respectively. Silicon substrates were etched for 2 minutes to make the etched depth of silicon substrate approximately 3000Å. Tables 7.4, 7.5 and 7.6 show process parameters for silicon nitride plasma etch, dry oxide plasma etch, and silicon substrate plasma etch, respectively.

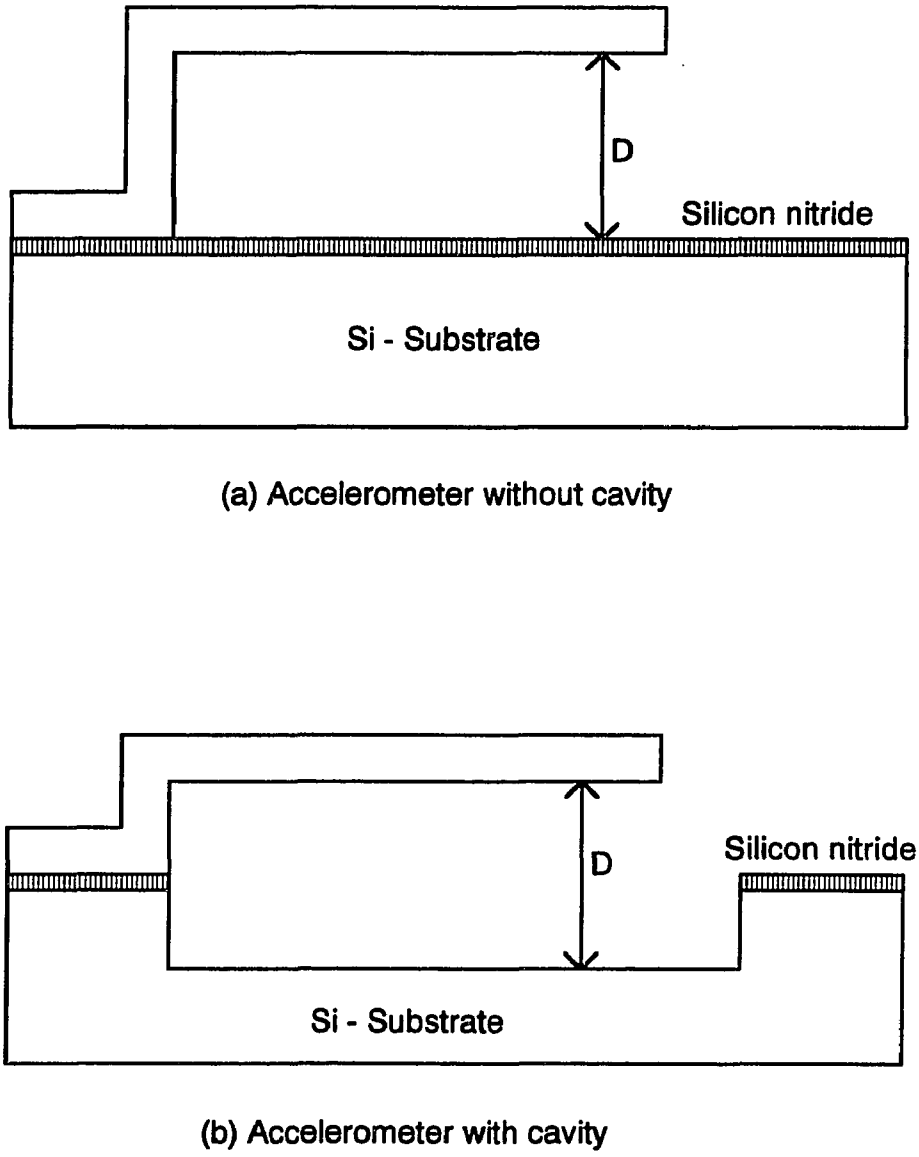

Figure 7.1 Differences in topography of two possible accelerometer designs: (a) Accelerometer without cavity; (b) Accelerometer with cavity

Table 7.3 Standard photolithography process parameters in NJIT

Parameter	Value
Vapor HMDS[1] Temperature	135 °C
Photoresist	Shipley 3813
Spin Speed	4500 RPM
Spin Time	25 seconds
Soft Bake Time / Temperature	60 seconds / 110 °C
Exposure Power Density	25 mW/cm^2
Developer	Shipley MF 319
Develop Time	45 seconds
Hard Bake Time / Temperature	60 seconds / 115 °C

[1] Hexamethyldisilazane or $(CH_3)_3Si\text{-}NH\text{-}Si(CH_3)_3$

After the completion of plasma etches of silicon nitride, dry oxide and silicon substrate, wafers were piranha striped (to remove photoresist) in 5:1 H_2SO_4:H_2O_2 solution at 110°C for 10 minutes followed by a hot deionized (DI) water rinse at 110°C for 10 minutes and a cold DI water rinse for 5 minutes. Wafers were then spin dried. Cavity depth, for 5 points on the wafer, was measured with a step profiler (Dektac IIA). For a lot of 5 wafers, the mean depth of the cavity was 5087Å, with a range of 4976Å to 5232Å.

Table 7.4 Plasma etch parameters for silicon nitride

Parameter	Value
SF_6 Flow	50 sccm
Pressure	150 mTorr
Power	400 Watts
Temperature	25 °C
Etch Rate	388 Å/minute

7.2 First Tantalum Silicide Deposition - Defining Bottom Electrode

Tantalum silicide was used for the bottom electrode of accelerometers, and was deposited by sputtering from a composite target in a Varian 3125 magnetron sputtering system. In order to determine the thickness of the first tantalum silicide layer, two factors should be considered. First, it must survive the final release etch. For 5 minutes of 7:1 BHF release

Table 7.5 Plasma etch parameters for dry oxide

Parameter	Value
CHF_3 (Freon 23) Flow	50 sccm
C_2F_6 (Freon 116) Flow	100 sccm
Pressure	150 mTorr
Power	400 Watts
Temperature	25 °C
Etch Rate	512 Å/minute

Table 7.6 Plasma etch parameters for silicon substrate

Parameter	Value
SF_6 Flow	50 sccm
C_2ClF_5 (Freon 115) Flow	50 sccm
Pressure	150 mTorr
Power	400 Watts
Temperature	25 °C
Etch Rate	1572 Å/minute

etch, the tantalum silicide bottom electrode would be consumed approximately 1000Å. This is because of the etch rate of tantalum silicide in the 7:1 BHF is approximately 186±15 Å/minute. Next, the thickness of tantalum silicide after release etch should not exceed 3000Å (which is the etched depth of the silicon substrate) to ensure the electrical insulation between the two electrodes. The effective thickness of the insulation layer becomes thinner as the thickness of the first tantalum silicide layer becomes thicker than 3000Å as illustrated in Fig. 7.2(a). If the thickness of the $TaSi_2$ layer is more than 5000Å (which is the actual depth of the cavity obtained by summing up of three layers which consisted of 1700Å of silicon nitride, 300Å of dry oxide and 3000Å of silicon substrate), there is a good possibility of the two electrodes making a short circuit . The reason for this is that there is a possible connection between the bottom electrode and cantilever beam anchor as shown in Fig. 7. 2(b). When we considered these factors, we decided on the bottom electrode thickness of 2800Å.

Wafers were furnace pre-cleaned in H_2O:HF=100:1 solution for 60 seconds to remove any native oxide layer. Wafers were then rinsed in hot DI water and cold DI water and then spin dried. Immediately following the spin dry, the wafers were loaded into the chamber of the sputtering system. The parameters for tantalum silicide deposition are given in table 7.7. The one difficulty observed during the deposition of tantalum silicide was that the stress built in the deposited tantalum silicide film would cause small pieces to occasionally flake off of the S-gun in the sputtering system. It was also noted that the tiny flakes often disrupted the plasma over the target. The flakes would sometimes cause a shorting of the anode to the target which was grounded, and this caused the plasma to be lost for a while. Since the power applied to the plasma is controlled through a feedback loop with a deposition rate monitor, the power called for by the deposition controller would begin to increase, because when the plasma was disrupted, the deposition rate began to drop off toward zero. When this occurred, the increased power was enough to quickly melt the small flake of tantalum silicide which caused the short in the first place.

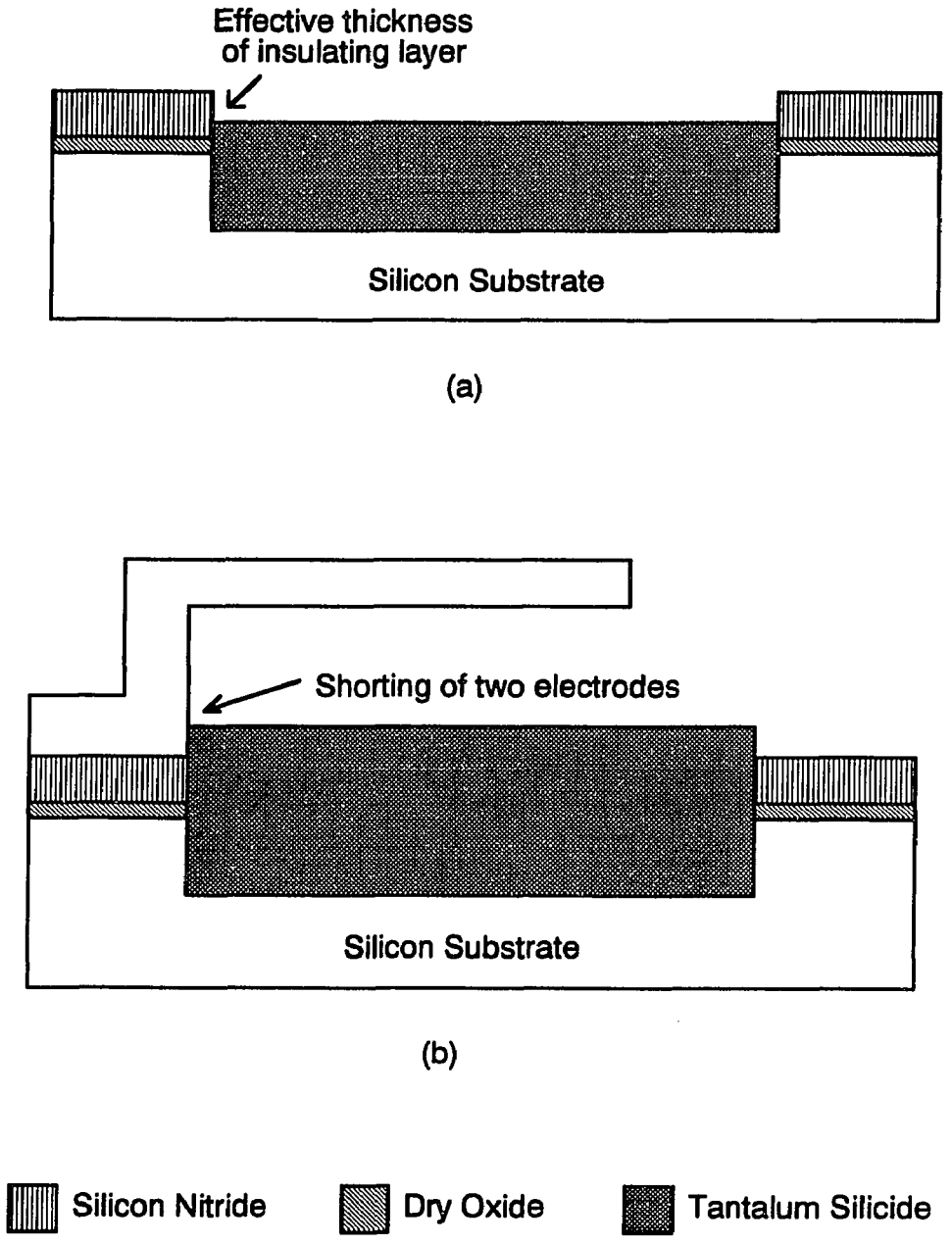

Figure 7.2 The effective thickness of the insulation layer: (a) When the tantalum silicide bottom layer is thicker than 3000Å; (b) When the tantalum silicide bottom layer is thicker than 5000Å

The plasma would be restored when the flake melted, but at a significantly higher power than desired. The sudden increase of power would usually result in a loss of the plasma again. After this cycle was repeated 2 or 3 times, the sputtering system would abort the deposition process completely. Two things were ultimately implemented to solve this flaking phenomenon. First, the maximum power for which the deposition controller could call was limited to 1-2% higher than that required to maintain the desired deposition rate. This meant that if there was a short in the plasma, the power level at which it came back on when the flake finally burned up was not significantly higher than where it should have been to maintain the desired deposition rate. The second, was that the deposition rate was lowered from 10 Å/second to 3 Å/second. This seemed to reduce the amount of flaking that occurred in the deposition chamber.

Table 7.7 Deposition parameters for tantalum silicide

Parameter	Value
Deposition Temperature	300 °C
Base Pressure	4.0×10^{-7} Torr
Deposition Pressure	2.2 mTorr
Backfill Gas	Argon
Deposition Rate	3 Å/second
Target Composition	$TaSi_{2.4}$

After tantalum silicide deposition, negative photoresist (Eagle NT-90) was coated and oven baked at 85°C for 25 minutes. Spin speed of 5000 rpm gave the thickness of the

negative photoresist approximately 2.8 μm. A summary of the coat and bake for negative photoresist is given in table 7.8 [105]. Mask #1 was used again to pattern the bottom electrodes and wafers were developed in Eagle 2005 developer. A three puddle (the first puddle for 60 seconds, the second puddle for 60 seconds, and the third puddle for 90 seconds) develop process was implemented in order to obtain the best result. Table 7.8 also presents a summary of the Eagle 2005 developer process steps [106].

Table 7.8 Negative photolithography process parameters

Parameter	Value
Photoresist	Eagle NT-90
Spin Speed	5000 RPM
Spin Time	30 seconds
Amount of Photoresist	3 ml
Oven Bake Time / Temperature	25 minutes / 85 °C
Exposure Power Density	25 mW/cm^2
Developer	Eagle 2005 (Diluted)
Develop Time	1st puddle : 60 seconds 2nd puddle : 60 seconds 3rd puddle : 90 seconds
Hard Bake Time / Temperature	60 seconds / 115 °C

The tantalum silicide layer was then plasma etched, and the etch recipe used is given in table 7.9. This etch recipe worked well with an etch rate of approximately 400 Å/minute. The degree of anisotropy of the etch was nearly one, and the selectivity to the negative photoresist was about 2.3:1.

After the plasma etch of tantalum silicide, wafers were piranha striped (to remove negative photoresist) in 5:1 H_2SO_4:H_2O_2 solution at 110°C for 10 minutes and this was followed by a hot deionized (DI) water rinse at 110°C for 10 minutes and a cold DI water rinse for 5 minutes. Wafers were then spin dried.

Table 7.9 Plasma etch parameters for tantalum silicide

Parameter	Value
SF_6 Flow	25 sccm
C_2ClF_5 (Freon 115) Flow	75 sccm
Pressure	150 mTorr
Power	400 Watts
Temperature	25 °C
Etch Rate	400 Å/minute

7.3. Sacrificial Layer Deposition and Patterning

In order to create a sacrificial layer, spin on glass (SOG) was coated on the wafers. The basic requirements for this SOG were that it be etched very fast in HF solution so that the beam structure is not attacked during the final release etch, and the film be uniform over a

wafer in order to give a uniform thickness of the gap distance of the accelerometers. The nominal thickness of Accuglass® 512 SOG furnished by Allied Signal is 5000Å per coating with thickness variation across wafer is less than 2% [107].

Twelve wafers were coated with SOG once and cured at 400°C for 40 minutes. A summary of the coat, bake and curing conditions is given in table 7.10. After cure, the film thickness was measured at 5 points on a wafer using the Leitz MPVSP film thickness measurement system. The average film thickness on the wafer was 5320Å. The standard deviation was 79Å which was about 1.5% of deviation from the average thickness. Eight wafers were coated with SOG for the second time to make the nominal thickness of the wafers become 1μm. Film thicknesses for 5 points on the wafer were measured after cure at 400°C for 40 minutes. The average thickness was 10387Å and the standard deviation was 286Å. Four wafers were coated with SOG for the third time to make the nominal film thickness become 1.5μm. After cure, the 5 point thickness measurement showed the average film thickness and the standard deviation were 14882Å and 688Å, respectively. Fig. 7.3 shows the SOG thickness versus points on a wafer.

Wafers were then coated with negative photoresist. The photolithography at this level became somewhat more difficult than at the previous level, since the photoresist was required to cover steps as high as 1.5μm. However, the thickness of negative photoresist was 2.8μm, and there was no difficulty in covering the topography with the photoresist. A summary of the coat, bake and develop conditions of the negative photoresist is given in table 7.8. The SOG etch was done in a Drytek DRIE-100 plasma etcher with SF_6 and Freon 115 based chemistry. A summary of the etch parameters is given in table 7.11. This etch recipe is exactly the same as that of dry oxide given in table 7.5, but the etch rate of SOG is 737 Å/minute while dry oxide etch rate is 512 Å/minute. The SOG could be wet-etched in HF containing solution, but wet chemical etch of HF solution might cause an isotropic etch of SOG resulting in nonuniform sacrificial layer as illustrated in Fig. 7.4(a).

Table 7.10 Spin on glass (SOG) process parameters

Parameter	Value
SOG	Allied Signal Accuglass 512
Spin Speed	3000 RPM
Spin Time	20 seconds
SOG Amount	2 ml
Hot Plate Bake Time / Temperature	60 seconds / 150 °C
Hard Bake Time / Temperature	40 minutes / 400 °C
Thickness per Coating	5000 Å
Thickness Variation Across Wafer	< 2 %

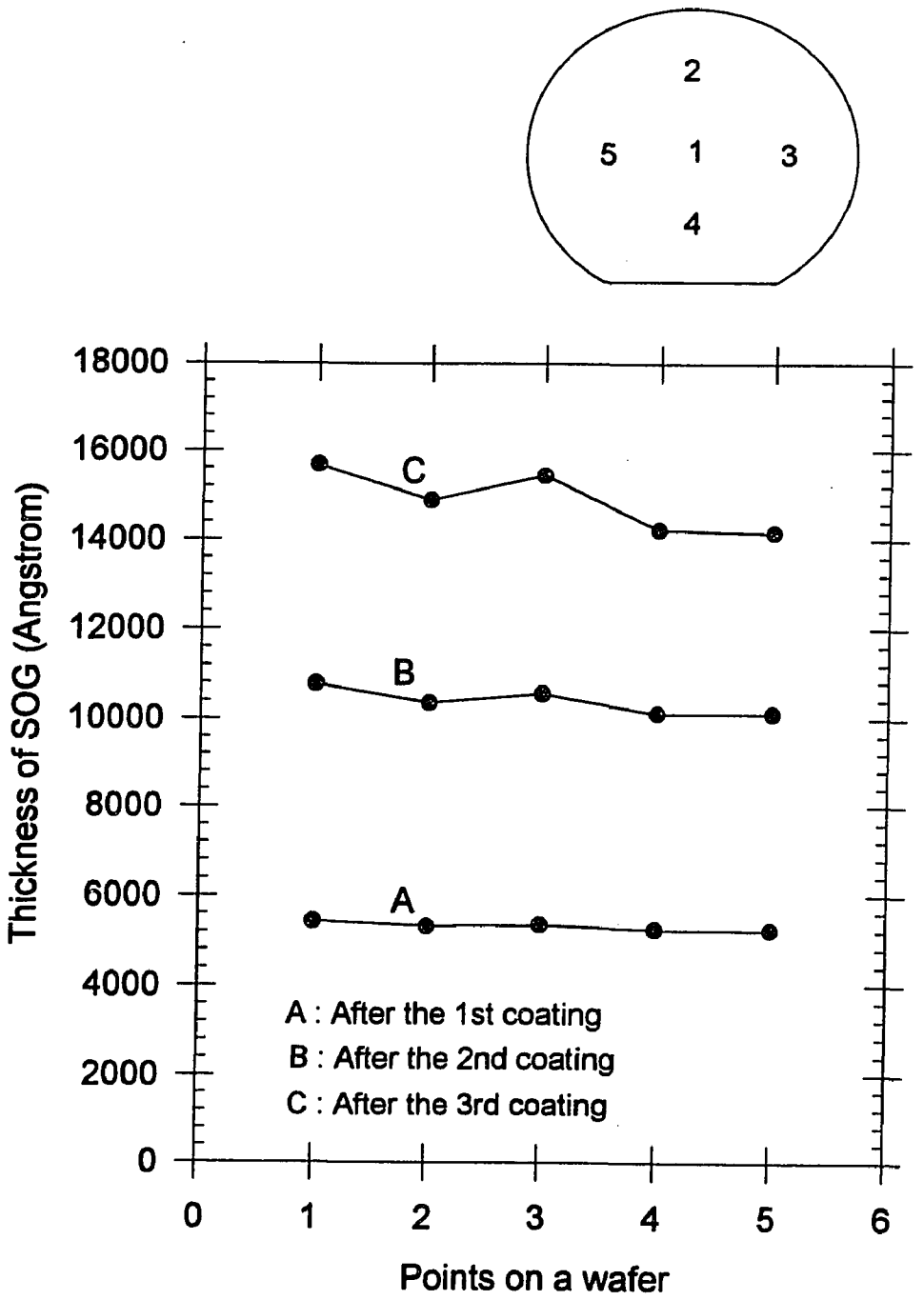

Figure 7.3 SOG thickness versus 5 points on a wafer

The predicted beam structure is shown in Fig. 7.4(b) and it is clear that the beam is not uniform.

7.4 Second Tantalum Silicide Deposition - Defining Beam Structure

After defining the sacrificial layer, a second layer of tantalum silicide was deposited and patterned to make the cantilever beam structure. The deposition conditions and plasma etch parameters used for this process step were exactly the same as those used for the bottom electrode. Since the steps present on the wafer at this level were approximately 2.1μm, a 2.8μm thick negative photoresist was used. Beam structures with three different thicknesses of 4000, 5000 and 6000Å were fabricated. The plasma etch time for the tantalum silicide was 13 to 16 minutes, depending on the thickness of the beam.

Table 7.11 Plasma etch parameters for SOG

Parameter	Value
CHF_3 (Freon 23) Flow	50 sccm
C_2F_6 (Freon 116) Flow	100 sccm
Pressure	150 mTorr
Power	400 Watts
Temperature	25 °C
Etch Rate	737 Å/minute

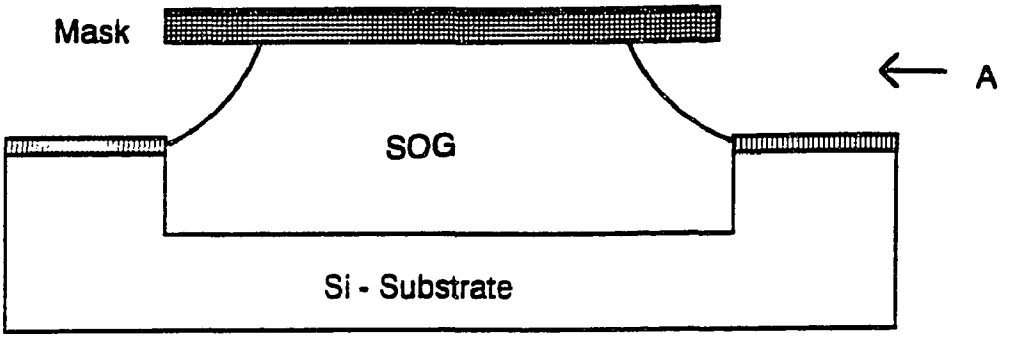

(a)

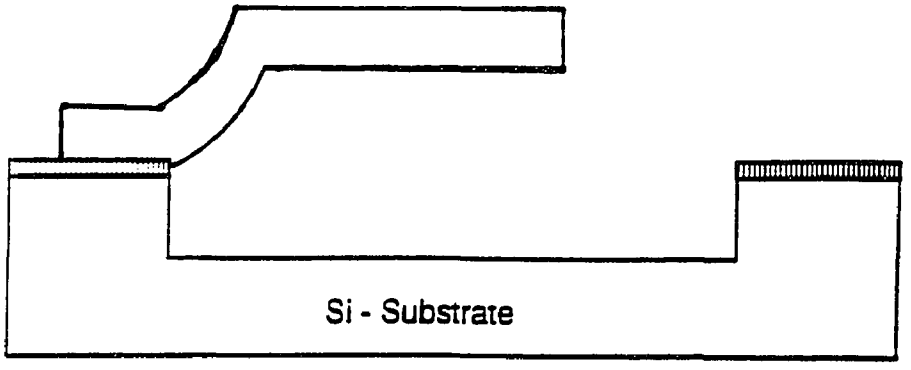

(b)

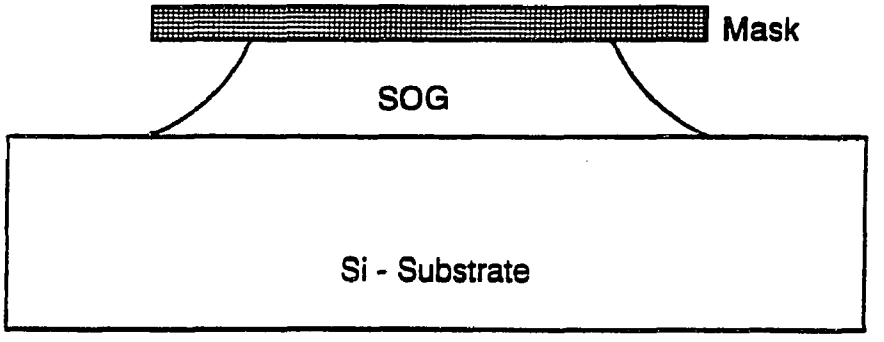

(c)

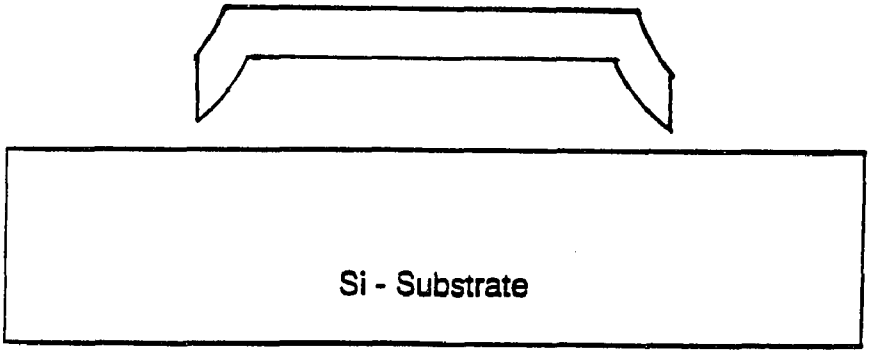

(d)

Figure 7.4 Isotropic etch of SOG resulting in nonuniform sacrificial layer: (a) nonuniform sacrificial layer; (b) predicted beam shape with sacrificial layer shown in (a); (c) nonuniform sacrificial layer seen from A of figure (a); (d) predicted beam shape seen from A of figure (a)

7.5 Metallization

Conductive films are required to provide an interconnection between contacts on devices, and between devices and the outside world. Cantilever beam accelerometers in this research, interconnection between contacts on devices is not required, because each accelerometer has only one individual electrode (which is from the beam) and all the accelerometers in a die have a common electrode at the backside of the die. Therefore, the only metallization needed is to connect the beam electrode to a pin at a package. Also, the backside of the die is to connect to a pin of the package. Aluminum is a viable choice for single-metal interconnections, since it bonds well to the silicon nitride insulating layers by a relatively short heat treatment [108]. The downside is that aluminum is subject to attack by the HF containing solution which is necessary for the sacrificial layer release etch which comes at the very last step of the whole fabrication step. It was necessary to find an alternate source of metallization which is not attacked by the HF containing solution. Tantalum silicide was chosen again as a interconnecting metal layer because it has a good etch resistance in HF and it also satisfies all the desired properties of interconnecting metallization for integrated circuits. These are listed below [109] :

(1) Low resistivity.

(2) Easy to form.

(3) Easy to etch for pattern generation.

(4) Should be stable in oxidizing ambients; oxidizable.

(5) Mechanical stability; good adherence, low stress.

(6) Surface smoothness

(7) Stability throughout processing, including high temperature sinter, dry or wet oxidation, gettering, phosphorous glass passivation, metallization.

(8) No reaction with final metal, aluminum.

(9) Should not contaminate devices, wafers, or working apparatus.

(10) Good device characteristics and lifetimes.

For a metal interconnection layer, a third tantalum silicide of 8000Å was sputter deposited and patterned (mask #3) using the same deposition conditions and plasma etch parameters used for the bottom electrode. Since the steps present at this level were approximately 2.9 μm, a 3.2 μm thick negative photoresist was used. The spin speed was adjusted to 3500 rpm to make the thickness of the negative photoresist 3.2 μm. The plasma etch time for the tantalum silicide was 22 minutes. Fig. 7.5 shows a completed metal interconnection.

7.6 Sacrificial Layer Release Etch

The final process step in the cantilever beam accelerometer was to release the beams by removing the sacrificial layer of spin on glass. The complete unreleased accelerometers were etched in 7:1 static BHF for 5 minutes. With an etch rate of the SOG of approximately 1.1 μm/minute, the 9μm wide beam would be completely released. Some of the wider beams would require more time. After 5 minutes etch and subsequent rinse and dry, the beams were inspected. The beams showed no signs of warpage and were remarkably strong (a beam 126 μm long was bent almost 90°, and sprang back to its original shape with no sign of damage). And beams with identical cross section, but changing lengths, were found to be straight and free of bowing as shown in Fig. 7.6, and Fig. 7.7 shows a complete released cantilever beam accelerometer. However, the tantalum silicide beam edges were eroded a bit since the edges were attacked by BHF. Fig. 7.8 shows eroded beam edges attacked by BHF during the final release etch. Beams etched more than 10 minutes showed serious erosion at the beam edges and some were broken as well.

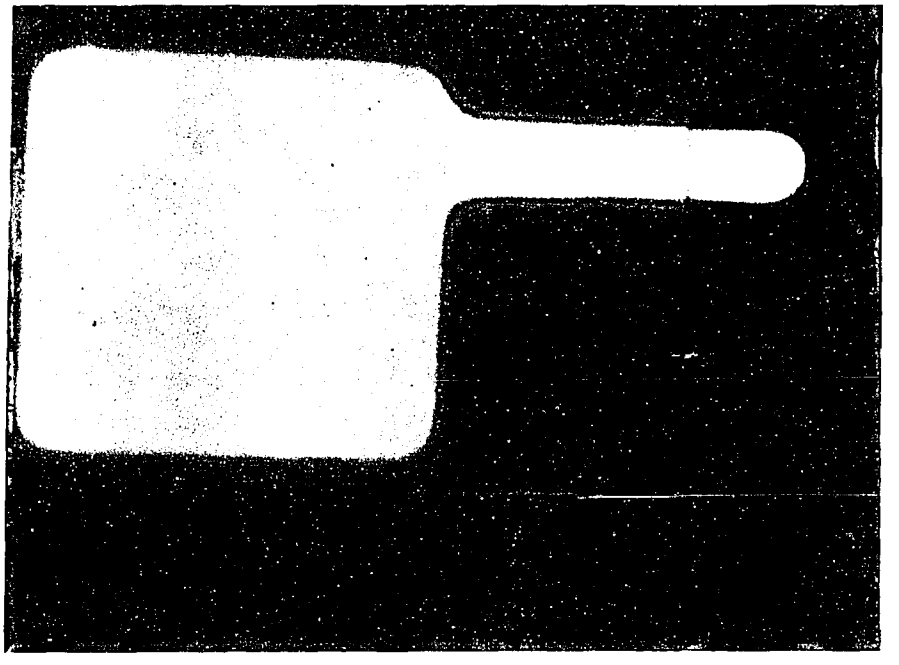

Figure 7.5 Optical micrograph showing the completed metal pad

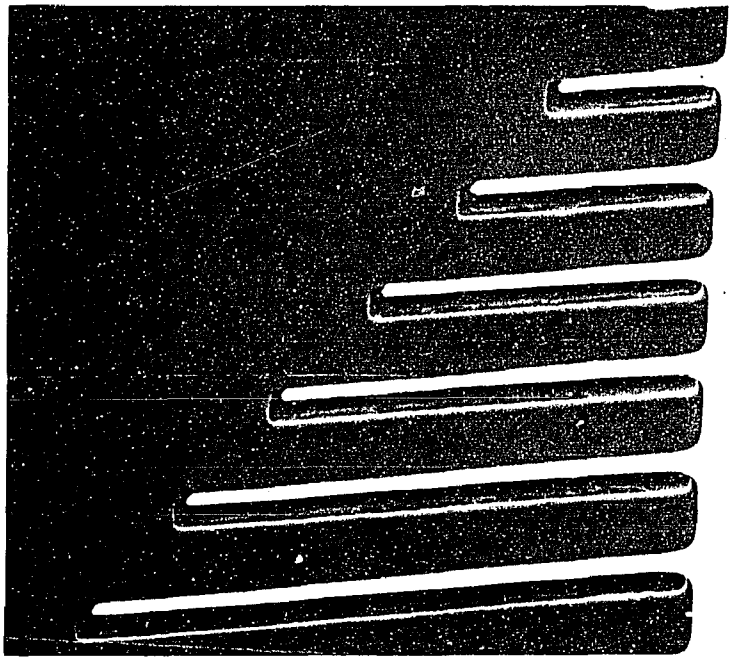

Figure 7.6 Scanning electron micrograph showing the released beam with identical cross section with different lengths. It shows the beams are straight and free of bowing.

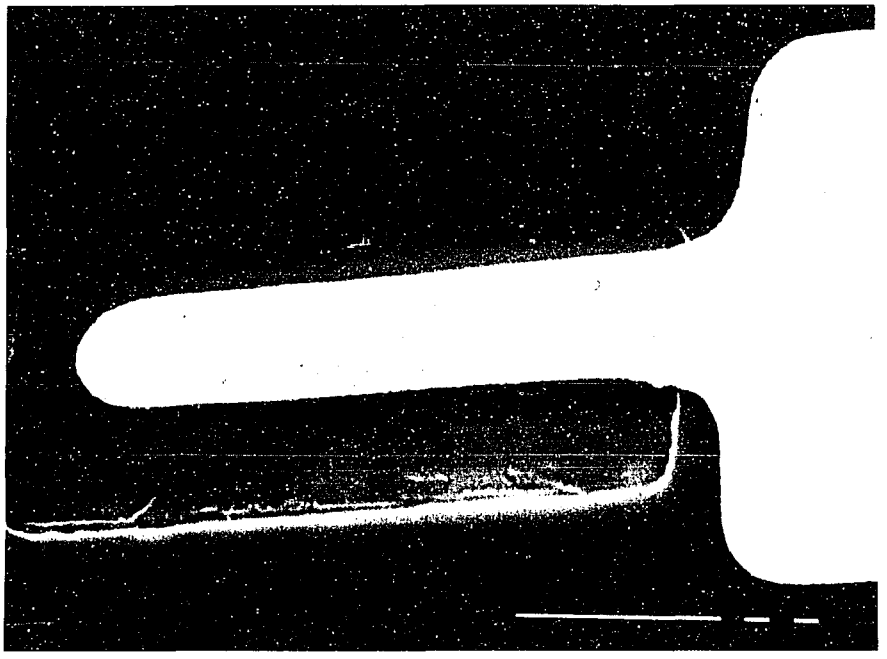

Figure 7.7 Scanning electron micrograph showing a completely released beam

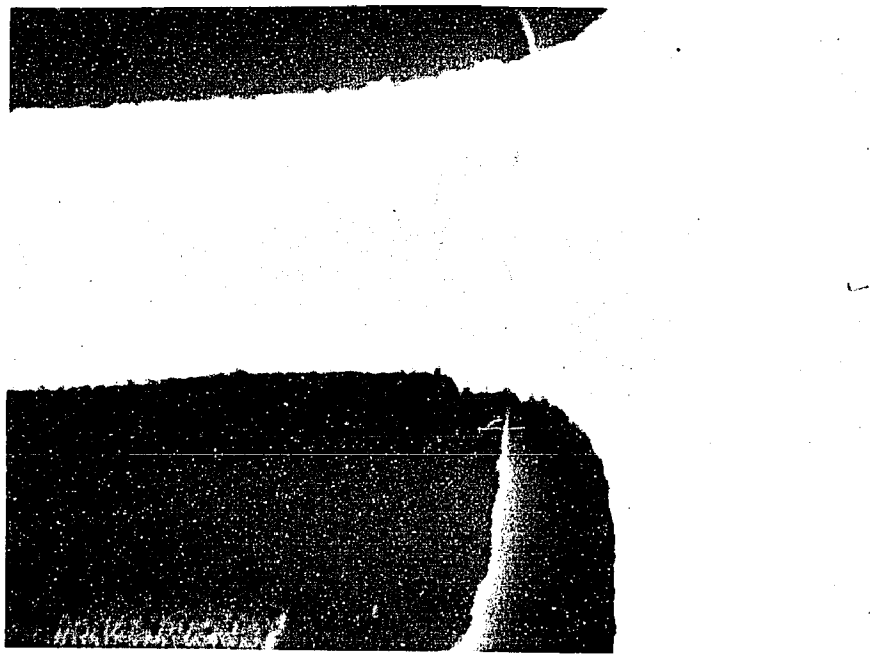

Figure 7.8 Scanning electron micrograph showing eroded beam edges attacked by BHF

CHAPTER 8

TEST OF ACCELEROMETERS

8.1 Electrostatic Attraction Test

After metallization, as described in section 7.5, wafers were diced into individual dies. These dies were then put into the boiling acetone (boiling temperature of acetone is 56.2°C) for approximately 10 minutes to remove the wax which was coated on the top of the wafers. This coating of wax was for the protection of the devices during the wafer dicing procedure. After they were rinsed in cold DI water for 5 minutes, the dies were then put into the methanol and blow dried using nitrogen gas. Dies were then released in the 7:1 BHF for 5 minutes to free the beams, whose widths are 6 μm and 9 μm. Dies were blow dried with nitrogen gas after hot DI water and cold DI water rinses.

Fig. 8.1 shows the overall system configuration used for the electrostatic attraction test. A source measurement unit (Keithley model 236) is connected to the IEEE-488 bus of the computer using a model 7007 IEEE-488 cable. A micro probe station, which is used as a test fixture, is also connected to the model 236 source measurement unit. An electrical equivalent circuit, of this test system, is illustrated in Fig. 8.2. The model 236 source measurement unit generates either a linear or a logarithmic sweep signal which is represented by the variable voltage source in Fig. 8.2. This unit is also equipped with a programmable current limiting circuit to protect the entire system, and this is represented by the resistance in the equivalent circuit. An accelerometer goes into the on position when the applied voltage to the accelerometer reaches the threshold level, and then the circuit makes a closed loop. The current flowing through this closed circuit is measurable with the installed ammeter. Fig. 8.3 shows current versus applied voltage for an accelerometer with T=0.5 μm, L=99 μm, and D=1.0 μm. The onset voltage is 2.2 volts and it reaches the preset current limit of 10 mA at 2.27 V. The resistance of this

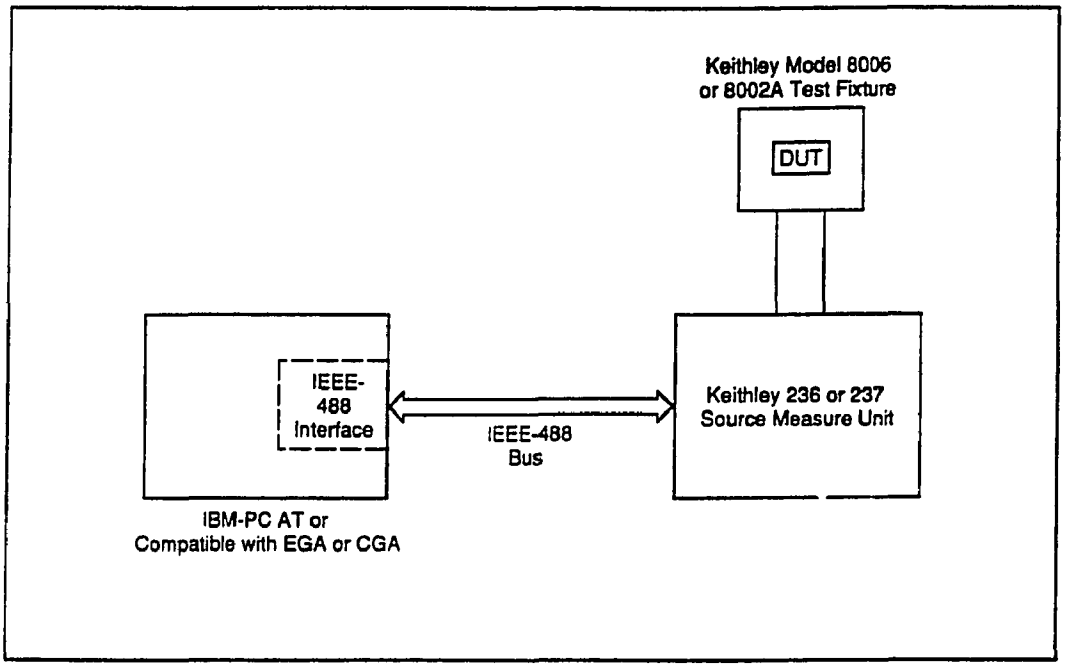

Figure 8.1 Overall system configuration used for the electrostatic attraction test

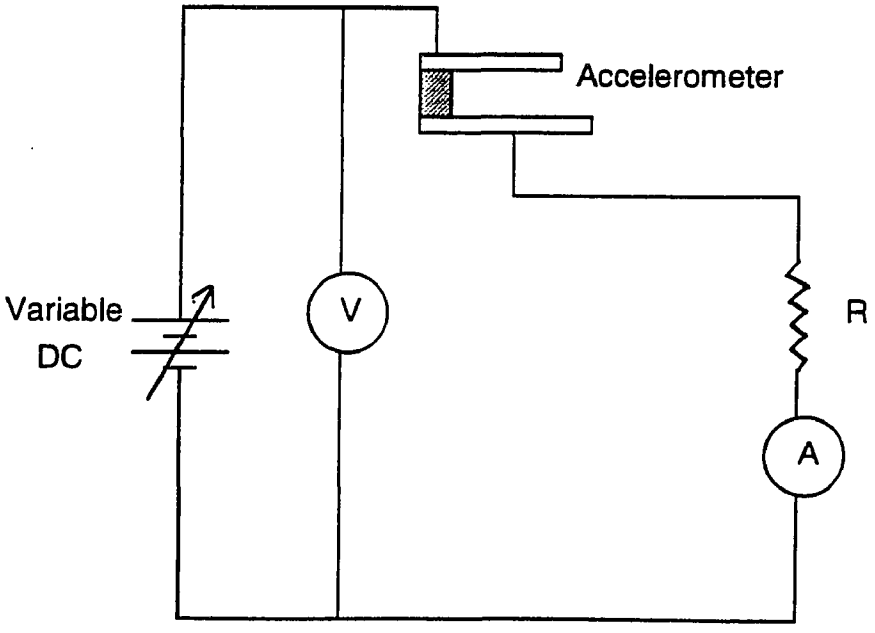

Figure 8.2 Electrical equivalent circuit of Fig. 8.1

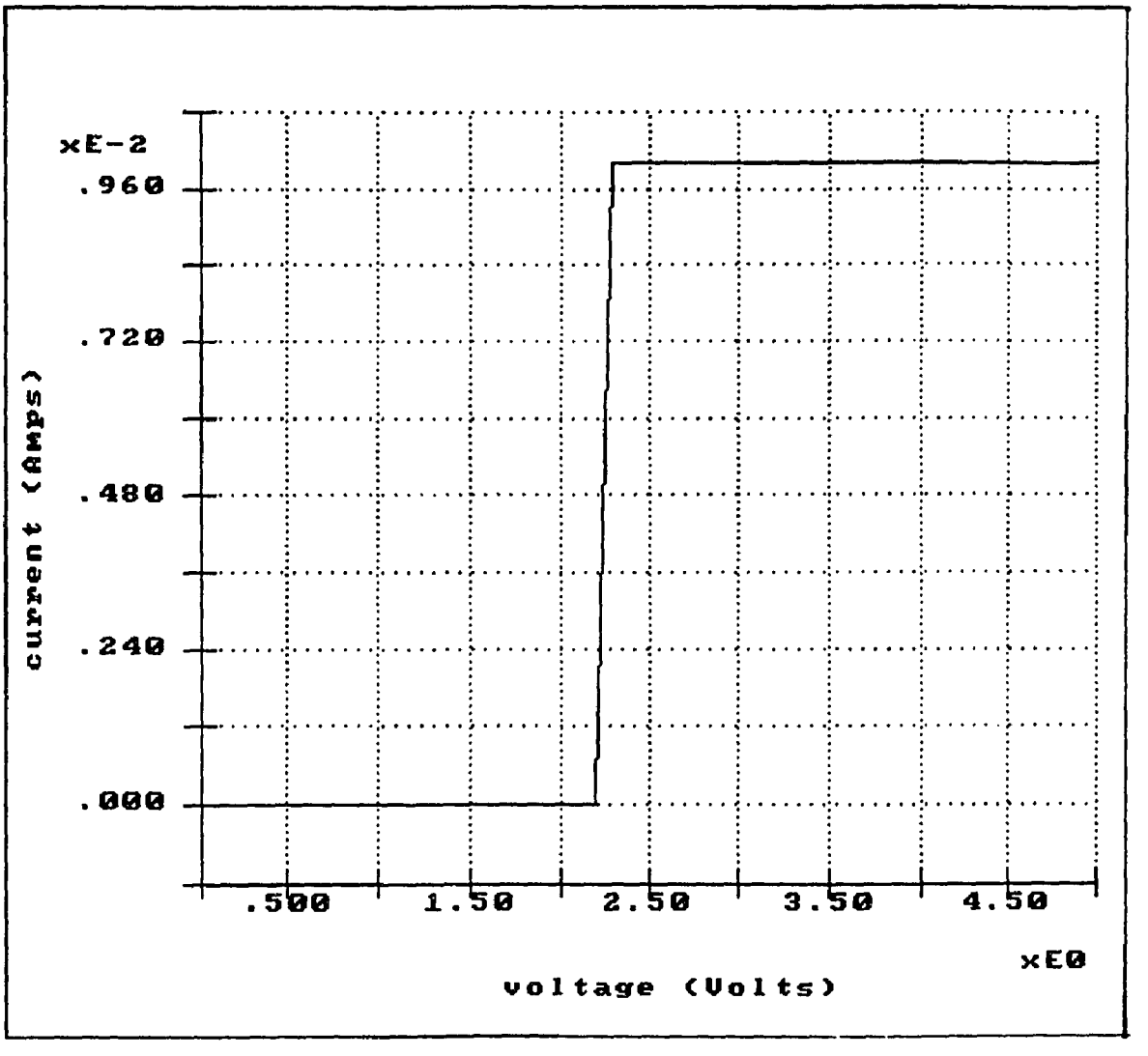

Figure 8.3 Current-voltage (I-V) characteristics of an accelerometer with T=0.5μm, L=99.0μm, and D=1.0μm

accelerometer, obtained by Ohm's law, is 7 ohms. The theoretical threshold voltage of this accelerometer is 1.75 volts from Eqn. (4.21). If the processing tolerances are taken into account, the theoretical threshold voltage ranges from 0.99 to 2.55 volts, and the measured threshold voltage of 2.2 volts resides in this range. The theoretical threshold voltage range is obtained by using the device dimension, with the expected error limits set by the processing parameters as described in table 8.1. For the particular batch of devices tested, variations of 2.8% for the deflection gap is assumed based on the variations of the SOG thickness on the wafer. For the theoretical threshold voltage calculation, the deflection gap is assumed to 2000Å wider than the thickness of the SOG sacrificial layer because, the first and the second tantalum silicide layers are also etched by 7:1 BHF for 5 minutes, and this results in an approximate 1000Å etch for each layer. The thickness of the beam is assumed to have an 1.5% tolerance based on the variation of the tantalum silicide thickness on the wafer. An 11% tolerance is assumed for Young's modulus, since the measured value shows 158.1±16.7 GPa as described in section 6.3.3.

Table 8.1 Tolerances of processing parameters to calculate the threshold voltage range

Parameter	Original value	After release etch	Tolerance
Length	30 - 126 μm	- 1000Å	± 5 μm
Thickness	5120Å	- 2000Å	± 1.5%
Deflection Gap	10472Å	+ 2000Å	± 2.8%
Young's Modulus	158 GPa	158 GPa	± 11%

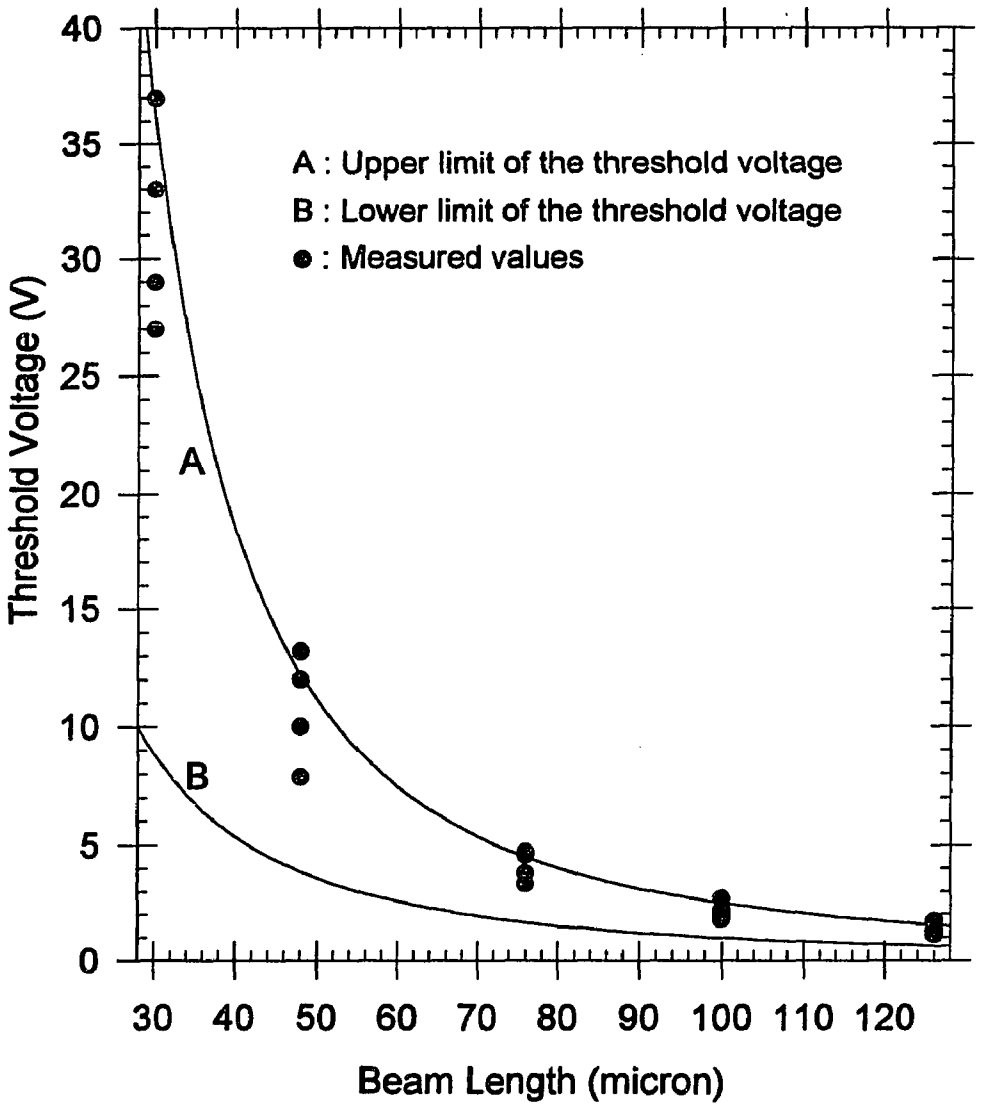

Figure 8.4 Measured threshold voltage for accelerometer closure during electrostatic attraction tests of accelerometers. The solid lines represent theoretical threshold voltages with the processing tolerances taken into account.

Table 8.2 Measured threshold voltage of accelerometers undergone to the electrostatic attraction test

Device #	Lenght (μm)	Width (μm)	Thickness (Å)	Deflection gap (Å)	Measured V_{th} (Volts)	Upper limit V_{th} (Volts)	Lower limit V_{th} (Volts)
1	30	6	5120	10472	27.3	36.16	8.87
2	30	6	5120	10472	33.2	36.16	8.87
3	30	6	5120	10472	36.8	36.16	8.87
4	30	6	5120	10472	28.9	36.16	8.87
5	48	6	5120	10472	7.99	12.22	3.87
6	48	6	5120	10472	13.2	12.22	3.87
7	48	6	5120	10472	10.2	12.22	3.87
8	48	6	5120	10472	11.8	12.22	3.87
9	75	9	5120	10472	4.61	4.48	1.66
10	75	9	5120	10472	3.32	4.48	1.66
11	75	9	5120	10472	3.89	4.48	1.66
12	75	9	5120	10472	4.77	4.48	1.66
13	99	9	5120	10472	2.04	2.50	0.99
14	99	9	5120	10472	2.70	2.50	0.99
15	99	9	5120	10472	1.89	2.50	0.99
16	99	9	5120	10472	2.23	2.50	0.99
17	126	9	5120	10472	1.15	1.54	0.63
18	126	9	5120	10472	1.27	1.54	0.63
19	126	9	5120	10472	1.73	1.54	0.63
20	126	9	5120	10472	1.32	1.54	0.63

The electrostatic attraction test results for 20 beams are shown in Fig. 8.4 and obtained data are given in table 8.2. The majority of the results fall within the expected error limits set by the processing parameters as shown in table 8.1. The electrostatic attraction test involved voltages ranging from 2.2 to 37.0 V, and these correspond to threshold acceleration levels in the 580 to 185000 g region. Despite the current limiter in the model 236 source measurement unit, beams tend to weld shut after the measurement is finished. However, most of the beams can be re-opened by lightly tapping the back of the dies. On-off tests of beams were performed using a circuit similar to Fig. 8.2. In order to limit the current passing through the contact pads after electrically closing the accelerometer, a 1MΩ resistor, in series with the accelerometer, was used as a current limiter. The on and off states of the accelerometer were detected by measuring the voltage across the resistor. When the accelerometer was on, there was a voltage reading across the resistor, and when it was off, there was no voltage reading across the resistor. Beams were closed and opened repeatedly, while the voltage applied to the accelerometers were alternatively increased and decreased. Fig. 8.5 shows the results of the on-off tests of the beams with the lengths of 48 μm, 75 μm, and 99 μm. The on and off voltages for the beam of 48 μm long, are 11±0.6 volts and 10±0.4 volts, respectively. The beam of 75 μm long showed on and off at 4±0.2 volts and 3±0.2 volts, respectively, and the beam of 99 μm long showed on and off at 2±0.3 volts and 1.5±0.2 volts, respectively. The obtained data are given in table 8.3.

8.2 Centrifuge Acceleration Test

After being released in the 7:1 BHF and subsequent rinses and nitrogen gas blow dry, two dies were mounted on to flat dual-in-line packages using epoxy and then wired up. The acceleration test was carried out in a specially designed centrifuge with an acceleration range of 282 through 11200 g's. The test apparatus consisted of a rotating disk powered by an AC/DC motor, a variac to adjust the motor speed, a high speed slip ring which

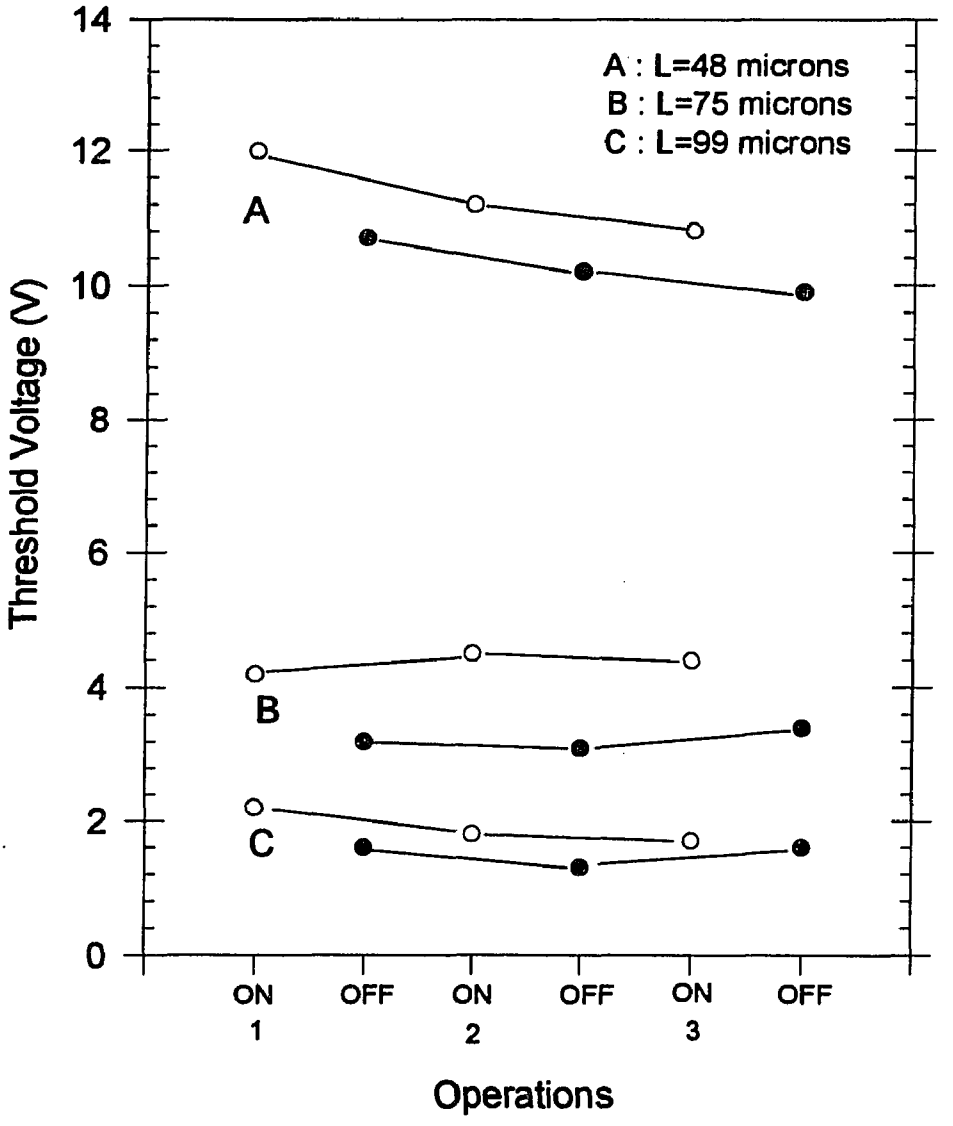

Figure 8.5 Result of repeated electrostatic attraction tests for three different accelerometers

Table 8.3 Result of repeated electrostatic attraction tests

Device ID #	Length (μm)	Width (μm)	Thickness (Å)	Deflection Gap (Å)	Measured Threshold Voltage (Volts)					
					on(1)	off(1)	on(2)	off(2)	on(3)	off(3)
A	48	6	5120	10472	12.04	10.72	11.21	10.22	10.83	9.92
B	75	6	5120	10472	4.21	3.23	4.52	3.11	4.42	3.38
C	99	9	5120	10472	2.08	1.68	1.84	1.42	1.92	1.55

connected the accelerometer to an electrical test circuit as shown in Fig. 8.6. The disk had 5 holes with different radii, 6.1 cm, 8.4 cm, 10.4 cm, 12.8 cm and 17.6 cm, to fasten the accelerometer holder with a screw, and 5 more radially symmetric holes for a weight to balance the whole disk, and to prevent it from wobbling. The electrical test circuit consisted of a DC power supply and a LED indicator. A variable DC power supply was chosen to apply the necessary variable bias voltage to the accelerometer. The motor speed can be controlled by changing the input voltage to the motor through the use of a variac. A transistor circuit for current amplification was also incorporated to lower the switching current of the cantilever to 0.5-1.0 mA. When the test samples were run in the centrifuge, the closing of the switch was indicated by the lighting up of the LED, and the instance of reopening of the cantilever was signaled by the extinguished LED. Six beams were tested and, the test results, together with the expected theoretical threshold acceleration levels with processing tolerances taken into account, are plotted in Fig. 8.7. The tested data are given in table 8.4. The results fall within the expected tolerance range. The processing tolerances are based on the same assumptions as were used for the electrostatic attraction test, and these are discussed in section 8.1. The range of accelerations tested varied from 282 to 11200 g. Beams were re-opened in the centrifuge once the applied acceleration was reduced below its threshold level. This seemed that lower current could alleviate the welding problem but there were no sufficient experimental data to prove this. We experienced some difficulties in bringing the centrifuge back to the previous speed which gave the threshold acceleration to the device. It was because the friction between the rotating and static parts of the slip ring was not constant all the time. An even slightly higher speed did not close the accelerometer again. Therefore, the repeated operation, of the threshold acceleration test, was performed by adjusting the applied voltage, to the device, with the imposed acceleration set to an accelerometer constant. For an accelerometer of 75 μm long, the acceleration of 5000 g was imposed, by setting the motor speed to 5050 rpm and the radius of the disk to 17.6 cm. With these settings, the

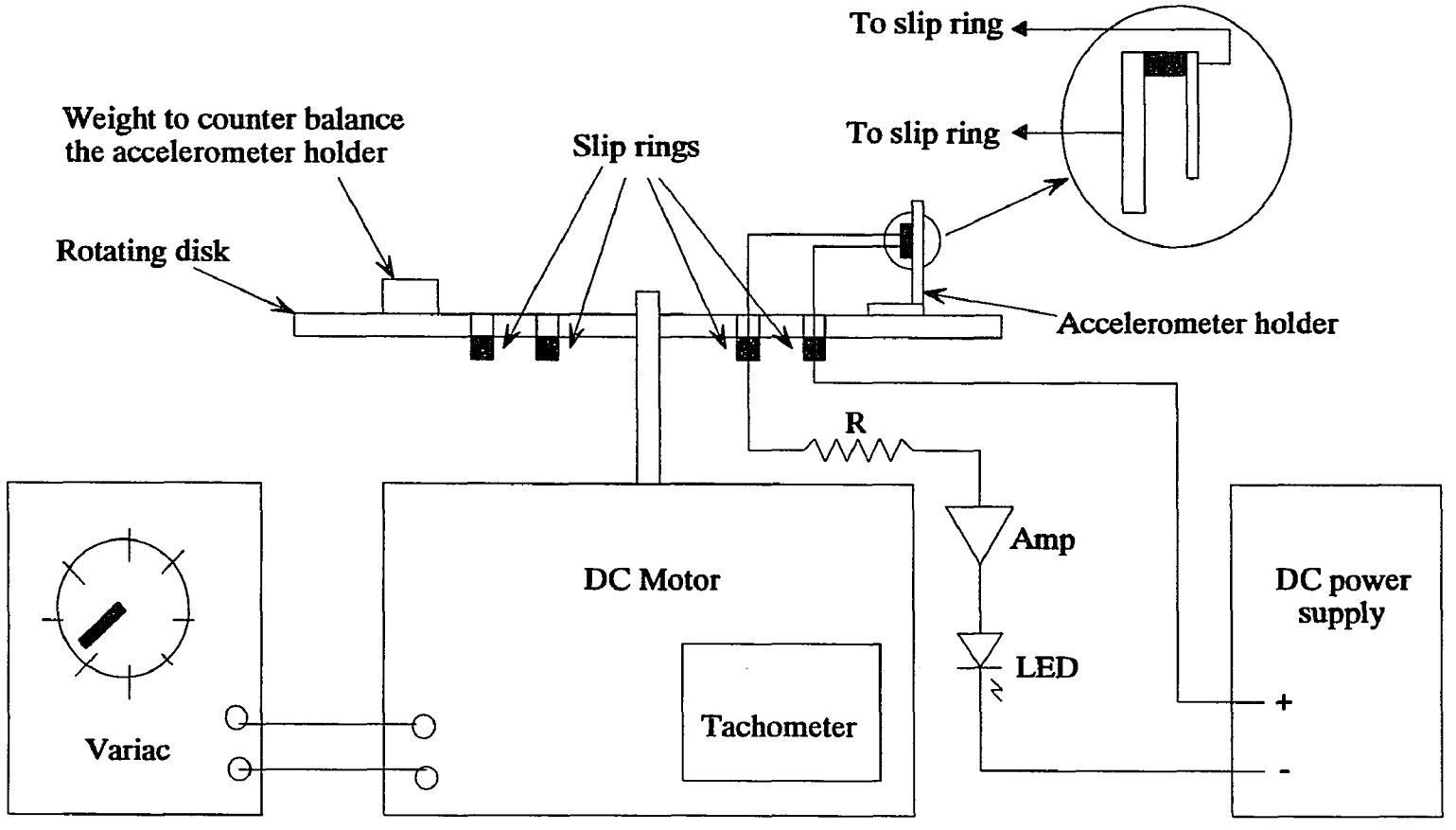

Figure 8.6 Test apparatus used for the centrifuge acceleration test

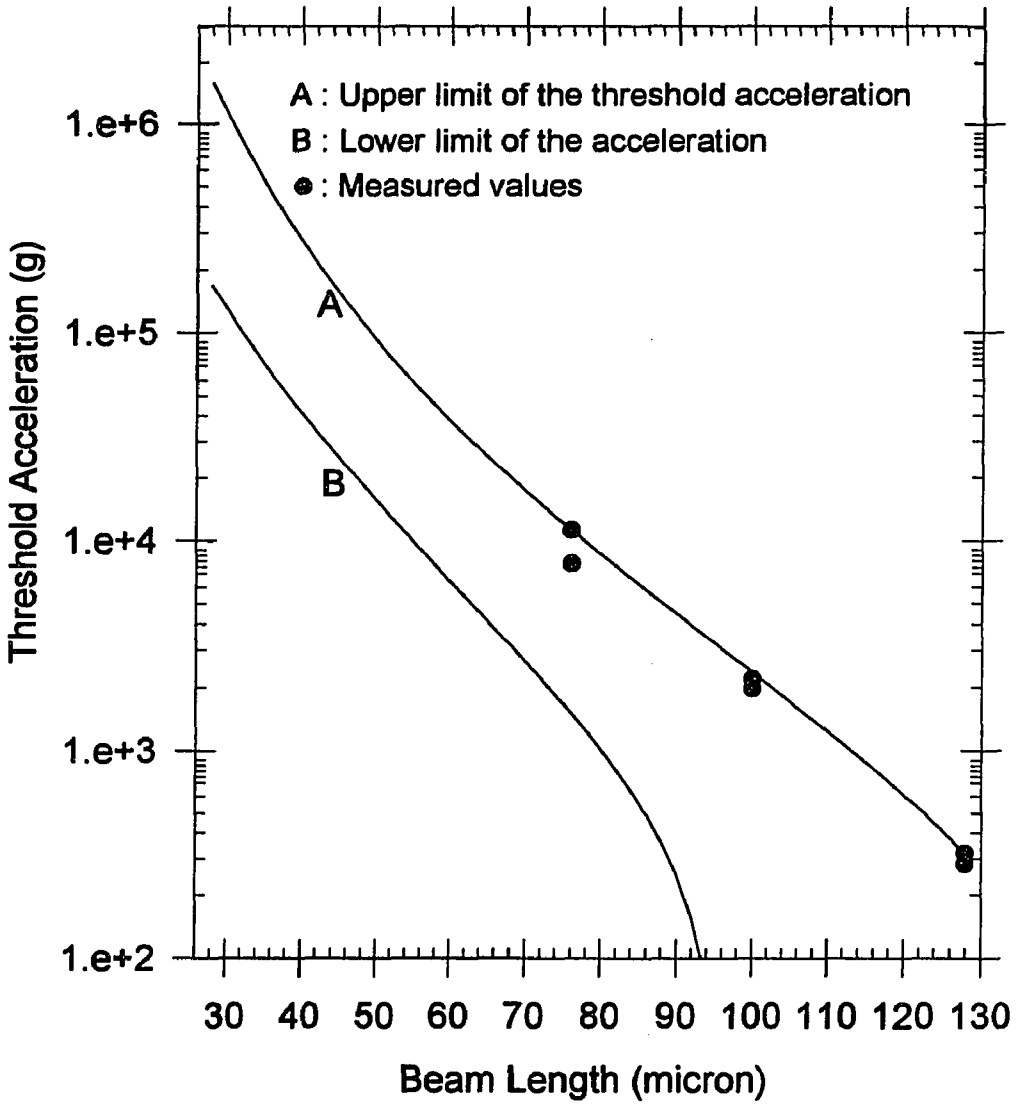

Figure 8.7 Measured threshold acceleration for accelerometer closure during centrifuge attraction tests of accelerometers. The solid lines represent theoretical threshold accelerations with the processing tolerances taken into account

Table 8.4 Measured threshold acceleration of accelerometers undergone to the centrifuge acceleration test

Device #	Lenght (μm)	Width (μm)	Thickness (Å)	Deflection gap (Å)	Measured a_{th} (g)	Upper limit a_{th} (g)	Lower limit a_{th} (g)
A1	75	9	5120	10472	11200	11312	1522
A2	75	9	5120	10472	7800	11312	1522
A3	99	9	5120	10472	2200	2368	0
A4	99	9	5120	10472	1980	2368	0
A5	126	9	5120	10472	320	314	0
A6	126	9	5120	10472	282	314	0

An applied voltage of 3 (volts) was used for all the accelerometers in this test.

applied voltage was increased to close the accelerometer contacts. Fig. 8.8 shows the result of the repeated operation with the fixed imposed acceleration. Graph A is for the beam of 75 μm long, and an imposed fixed acceleration of 5000 g. This beam closed at the applied voltage of 15.2 V, opened at 13.9 V, re-closed at 14.7 V, and re-opened at 13.8 V. Graph B is for the beam of 99 μm long, and an imposed fixed acceleration of 2000 g. This beam closed at the applied voltage of 3.2 V, opened at 2.1 V, re-closed at 3.4 V, and re-opened at 2.2 V. Table 8.5 shows the data obtained from this repeated operation.

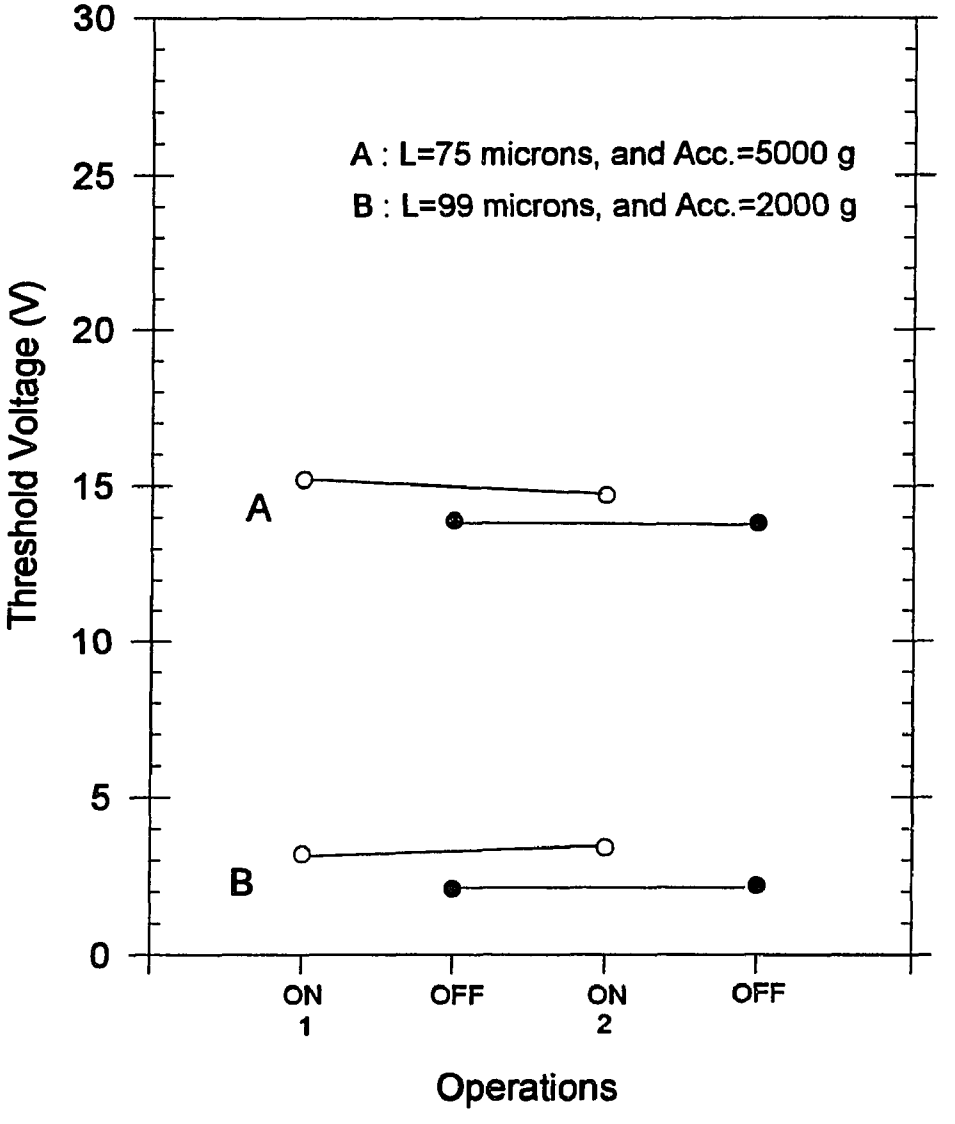

Figure 8.8 Result of repeated centrifuge acceleration tests for two different accelerometers. For these tests, imposed acceleration was fixed to 2000 g for the accelerometers of 99 microns long, and 5000 g for the accelerometers of 75 microns long.

Table 8.5 Result of repeated centrifuge acceleration tests

Device ID #	Length (μm)	Width (μm)	Thickness (Å)	Deflection Gap (Å)	Imposed Acc-eleration (g)	Measured Threshold Voltage (Volts) on(1)	off(1)	on(2)	off(2)
A	75	6	5120	10472	5000	15.2	13.9	14.7	13.8
B	99	6	5120	10472	2000	3.2	2.1	3.4	2.2

CHAPTER 9

SUMMARY AND CONCLUSIONS

Surface micromachined tantalum silicide threshold accelerometers were successfully designed and fabricated in this work. By using tantalum silicide as a beam material, the need of metal contact on the beam or metal line along the beam length was completely eliminated, making the process steps simpler and saving at least one mask level. The use of tantalum silicide prevents the curling of the beam under thermostatically induced stress or warpage of the beam due to differential thermal expansion coefficient between the beam material and metal contact. There had been no previous research on tantalum silicide accelerometers.

The accelerometers were fabricated using a novel surface micromachining process developed in this research. The process involved fewer fabrication steps than other approaches including: (1) accelerometers by Forbenius [18] which utilized electro-deposition and evaporation of three different metals (titanium, gold, and nickel) and require at least 4 mask levels.; (2) Honeywell [19] accelerometers which required along-the-beam metallization on the top of the beams to provide conducting switch contact and also needed field-assisted anodic bonding of the glass plates, which is not suitable for batch fabrication. (Honeywell accelerometers use bulk micromachining processing of silicon substrates and thus require anodic bonding.); (3) Motorola accelerometers [19] which have deposited metal (gold) at the tip of the beam to provide conducting switch contact. (At least 4 mask levels are required to fabricate the devices.); (4) Harry Diamond Laboratories (HDL) accelerometers [19] which require evaporated gold-nickel-gold sandwich beams to provide conducting switch contact of the accelerometer. (At least 4 mask levels are necessary.); (5) accelerometers made by Loke [20] which require evaporated chrome and gold lines running along the beam length to provide the conducting switch contact. Loke's accelerometers use bulk micromachining process which

required anodic bonding of Pyrex glasses and at least 3 mask levels. Table 9.1 compares the result and advantages of cantilever beam accelerometers made in other research. The tantalum silicide accelerometers developed in this research do not require additional metallization because of the low resistivity (270 μΩ-cm for as deposited films at 300°C). Thus they provide for low contact resistance for fast switching and low power consumption at the contact point.

The normal three-mask level process steps required for fabrication of cantilever beam, cavity formation (mask #1), sacrificial layer (mask #2), and beam structure (mask #3), were reduced to a two-mask level process by utilizing both positive and negative photoresists. NJIT's standard photolithography steps were used for positive photoresist; however for the negative photoresist a multi-puddle process was developed to obtain 4 micron resolution.

The electrostatic attraction tests of the fabricated tantalum silicide accelerometers showed that as the beam length varied from 30 to 126 μm the threshold voltage to close the accelerometer switch varied from 2.2 to 37.0 volts, corresponding to threshold acceleration levels from 580 to 18,500 g. Nearly 70 percent of the threshold voltage results fell within the expected error limits set by the accuracy of the device dimensions when processing tolerances (see table 8.2) were taken into account. About 20% of the accelerometers tested were closed and opened up to 3 times. The failure after closure was attributed to the welding of contacts since approximately 1 mA was passed through when contact made. Centrifuge acceleration tests of accelerometers were carried out in a specially designed centrifuge in an acceleration range of 282 to 11,200 g. Nearly 80 percent of the threshold acceleration results fell within the expected error limits set by the accuracy of the device dimensions when processing tolerances (see table 8.2) were taken into account.

It was concluded that the tantalum silicide threshold accelerometers have excellent potential for single acceleration threshold detection because they can be batch fabricated at

Table 9.1 Comparison of recent research on cantilever beam threshold accelerometers

Ref./Year	Material [1]	Dimension [2] (μm)	Test Method	Test Range (g)	Result	Remarks
Frobenius [18] 1972	Au / Au / glass, oxidized Si / Ni	T=1.5 L=10 mil	centrifuge	10 - 8,000	performed well fatigue of gold	evaporation of Au, Ti, Ni
Honeywell [19] 1987	epitax Si / Ti-W, Pd, Au / Pyrex / bulk process	T=15, W=250, L=750-1550	centrifuge	230 - 11,600	50% functioned, higher accel. need for closure	along-the-beam metallization, anodic bonding
Motorola [19] 1987	SiO_2 / Au / Si / N.A.	T=3, W=30, L=150-435, D=1	electrostatic, centrifuge	N.A.	welding of gold higher accel. need for closure	metal deposit
HDL [19] 1987	Au-Ni-Au / Au, Cr / Si / SiO_2	T=1.9, W=50, L=100-235, D=1	centrifuge	380 - 9,600	stuck closed	evaporation of Au-Ni-Au beam
Loke [20] 1991	SiO_2 / Au-Cr / Si, Pyrex / bulk process	T=2.2, W=80, L=120-400, D=2.5	electrostatic, centrifuge	400 - 10,000	performed well minor welding of contacts	along-the-beam Cr, Au evapo., anodic bonding
NJIT 1995	$TaSi_2$ / $TaSi_2$ / Si / SOG	T=0.6, W=9 L=30-126, D=1	electrostatic, centrifuge	280 - 18,500	performed well contact welded	no need of anodic bonding or metallization

[1] (beam / contact / substrate / sacrificial layer)
[2] T=thickness, W=width, L=length, D=deflection gap

low cost and with a variable threshold depending on the selected device dimensions. Applications could include impact acceleration sensors for automobiles and other vehicles or centrifugal force sensors in rotary machines.

It is suggested that the current design and fabrication process need to be improved for better operation and yield. Mask #1, which defines the cavity, needs to be wider to give more room for the beam to be located inside the cavity. Since the same mask was used three times (to define cavity, bottom electrode, and sacrificial layer), a careful mask design and improvement of the negative photoresist resolution are desired.

As described in section 7.2, the etch rate of tantalum silicide in 7:1 BHF is 186±8%. While it takes 5 minutes for complete removal of SOG sacrificial layer, the tantalum silicide beam can be etched by BHF during the time the SOG layer is being etched away. To avoid the variation in the final thickness of the beam due to the 8% of uncertainty in the BHF etch rate of tantalum silicide, the tantalum silicide beam could be protected against etching by BHF by using a polysilicon layer deposited on the tantalum silicide. This could be done with no additional mask.

As shown in Fig. 8.5 on page 109, the accelerometers tended to fail after 3 times of operation due to the contact welding. For a longer life of accelerometers, it is suggested that the test current be limited less than 0.1 mA. The contact forces can be greater with the large end mass, making contact less sensitive to the presence of debris, and the restoring forces of the beams become greater, making it more likely that deflected beam will remain free.

APPENDIX A

DETAIL OF PROCESS SEQUENCE

A.1 Process Flow

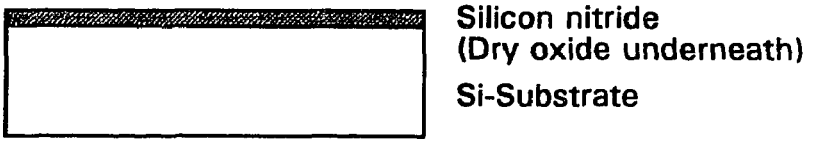

Figure A.1 LPCVD silicon nitride deposition (process steps 1-11)

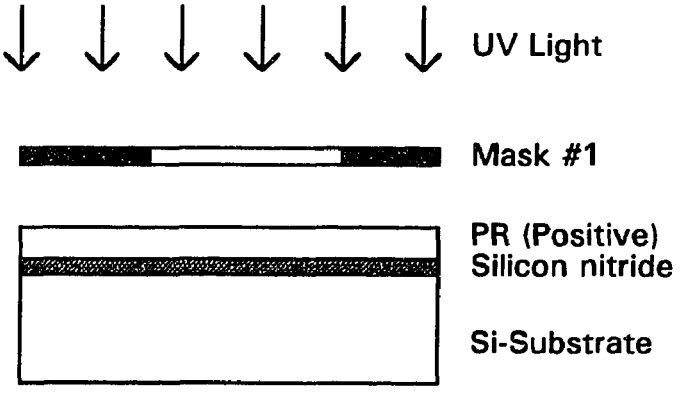

Figure A.2 Pattern definition for cavity (process steps 12-13)

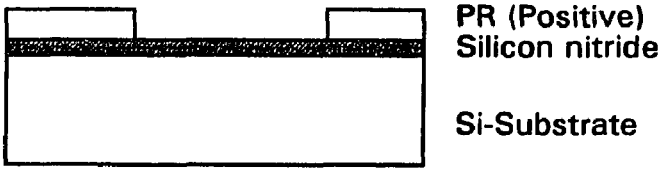

Figure A.3 After development of photoresist (process step 14)

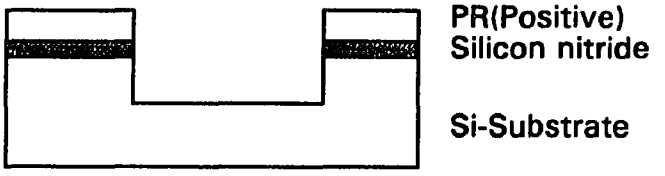

Figure A.4 After plasma etches of silicon nitride, dry oxide and silicon substrate (process steps 15-17)

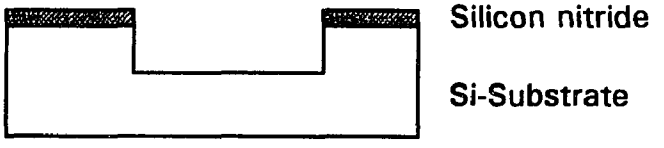

Figure A.5 Patterned silicon nitride and etched cavity in silicon substrate (process steps 18-20)

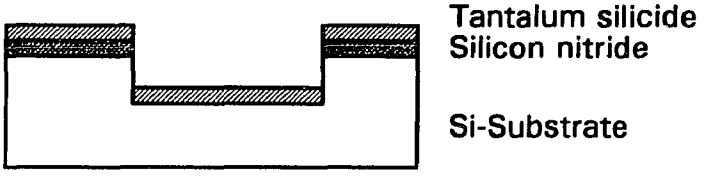

Figure A.6 Deposited tantalum silicide for bottom electrode (process steps 21-27)

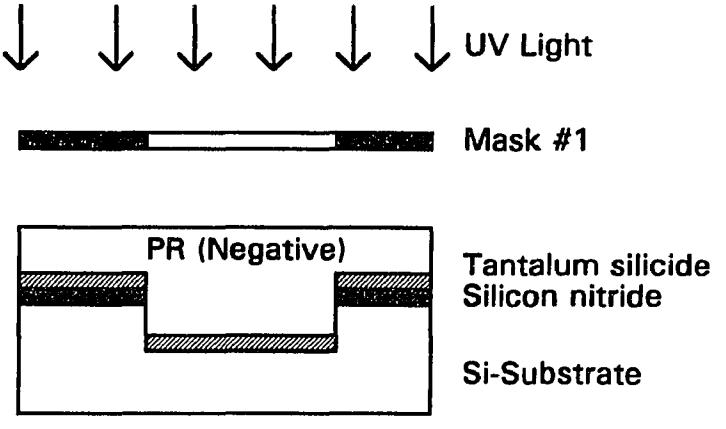

Figure A.7 Pattern definition for bottom electrode (process steps 28-29)

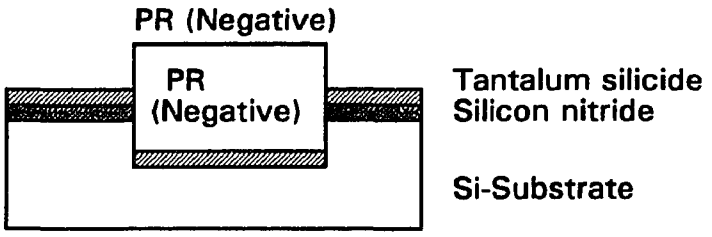

Figure A.8 After development of negative photoresist (process step 30)

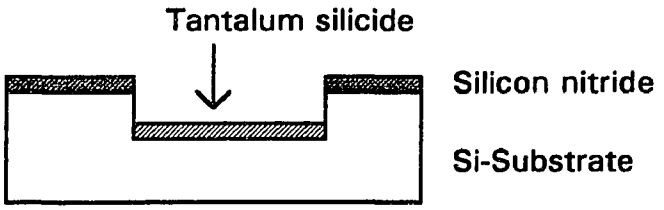

Figure A.9 Defined tantalum silicide bottom electrode (process steps 31-34)

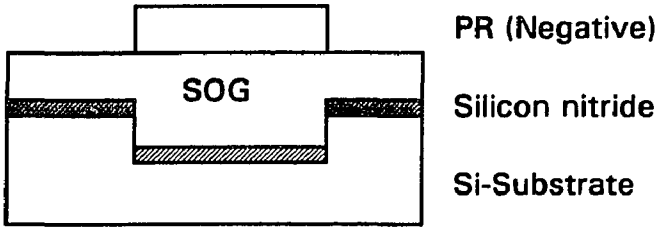

Figure A.10 Deposited SOG and developed negative photoresist (process steps 35-44)

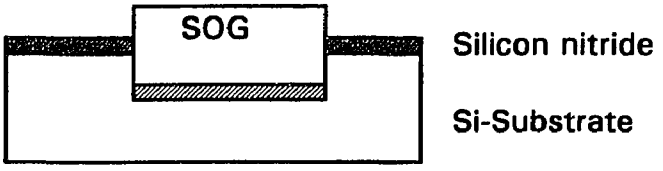

Figure A.11 Patterned SOG sacrificial layer (process steps 45-48)

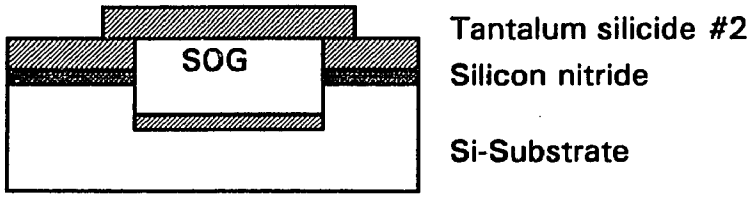

Figure A.12 Deposited tantalum silicide for beam structure (process steps 49-55)

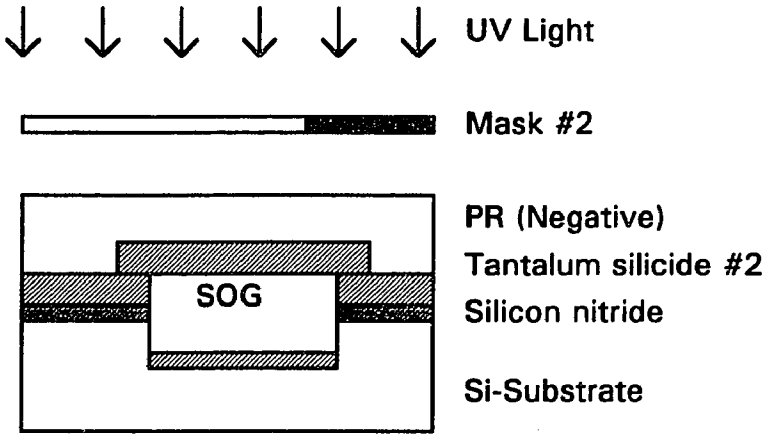

Figure A.13 Pattern definition for beam structure (process steps 56-57)

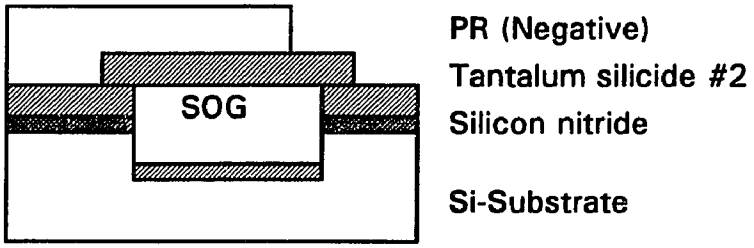

Figure A.14 After development of negative photoresist (process step 58)

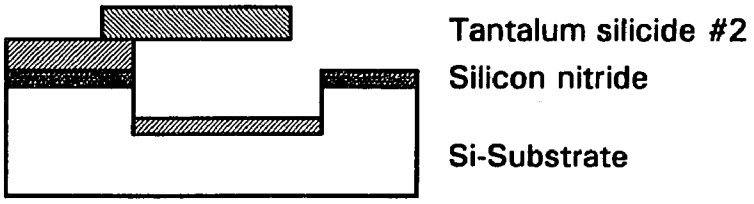

Figure A.15 Completed cantilever beam after BHF release etch (process steps 59-63)

A.2 Process Traveler Steps

1. P-clean, 5:1 H_2SO_4 : H_2O_2, 110 °C, 10 minutes
2. DI rinse, 10 minutes hot, 5 minutes cold
3. Spin dry
4. Furnace pre-clean, 100 : 1 HF Dip, 25 °C, 60 seconds
5. DI rinse, 5 minutes cold
6. Spin dry
7. Dry oxidation, 300 Å
8. Furnace pre-clean, 100 : 1 HF Dip, 25 °C, 60 seconds
9. DI rinse, 5 minutes cold
10. Spin dry
11. Deposit LPCVD silicon nitride, 50 sccm DCS, 120 sccm NH_3 , 400 mTorr, 775 °C 1700 Å
12. Vapor HMDS, chill, coat wafers with Shipley 3813 photoresist, 4500 RPM, soft bake @ 110 °C, 60 seconds (Prog #1)
13. Expose photoresist, 10 seconds, mask #1
14. Develop 45 seconds with Shipley MF319 developer, hard bake @ 115 °C 60 seconds (Prog #2)
15. Plasma etch silicon nitride, 50 sccm SF_6, 150 mTorr, 25 °C, 400 Watts, 388 Å/minute, 5 minutes, then measure and adjust remaining etch time accordingly
16. Plasma etch dry oxide, 50 sccm CHF_3, 100 sccm C_2F_6, 150 mTorr, 25°C, 400 Watts, 512 Å/minute
17. Plasma etch silicon substrate, 50 sccm SF_6, 50 sccm C_2ClF_5, 150 mTorr, 25 °C, 400 Watts, 1572 Å/minute
18. P-strip photoresist, 5:1 H_2SO_4 : H_2O_2, 110 °C, 10 minutes
19. DI rinse, 10 minutes hot, 5 minutes cold

20. Spin dry
21. P-clean, 5:1 H_2SO_4 : H_2O_2, 110 °C, 10 minutes
22. DI rinse, 10 minutes hot, 5 minutes cold
23. Spin dry
24. Furnace pre-clean, 100 : 1 HF Dip, 25 °C, 60 seconds
25. DI rinse, 5 minutes cold
26. Spin dry
27. Sputter deposit $TaSi_2$, 300 °C, 2.2 mTorr, 3 Å/second, 2800 Å
28. Coat wafers with Eagle NT-90 negative photoresist, 5000 RPM, oven bake @ 85 °C 25 minutes
29. Expose negative photoresist, 40 seconds, mask #1
30. Develop using a three puddle method (60, 60 and 90 seconds) with Eagle 2005 developer, hard bake @ 115 °C 60 seconds
31. Plasma etch $TaSi_2$, 25 sccm SF_6, 75 sccm C_2ClF_5, 150 mTorr, 25 °C, 400 Watts
32. P-strip negative photoresist, 5:1 H_2SO_4 : H_2O_2, 110 °C, 10 minutes
33. DI rinse, 10 minutes hot, 5 minutes cold
34. Spin dry
35. P-clean, 5:1 H_2SO_4 : H_2O_2, 110 °C, 10 minutes
36. DI rinse, 10 minutes hot, 5 minutes cold
37. Spin dry
38. Furnace pre-clean, 100 : 1 HF Dip, 25 °C, 60 seconds
39. DI rinse, 5 minutes cold
40. Spin dry
41. Coat wafers with SOG, Allied Signal Accuglass 512, 3000 RPM, bake @150 °C, 60 seconds, hard bake @ 400 °C, 40 minutes
42. Coat wafers with Eagle NT-90 negative photoresist, 5000 RPM, oven bake @ 85 °C 25 minutes

43. Expose negative photoresist, 40 seconds, mask #1
44. Develop using a three puddle method (60, 60 and 90 seconds) with Eagle 2005 developer, hard bake @ 115 °C 60 seconds
45. Plasma etch SOG, 50 sccm CHF_3, 100 sccm C_2F_6, 150 mTorr, 25 °C, 400 Watt
46. P-strip negative photoresist, 5:1 H_2SO_4 : H_2O_2, 110 °C, 10 minutes
47. DI rinse, 10 minutes hot, 5 minutes cold
48. Spin dry
49. P-clean, 5:1 H_2SO_4 : H_2O_2, 110 °C, 10 minutes
50. DI rinse, 10 minutes hot, 5 minutes cold
51. Spin dry
52. Furnace pre-clean, 100 : 1 HF Dip, 25 °C, 60 seconds
53. DI rinse, 5 minutes cold
54. Spin dry
55. Sputter deposit $TaSi_2$, 300 °C, 2.2 mTorr, 3 Å/second, 4000, 5000, 6000 Å
56. Coat wafers with Eagle NT-90 negative photoresist, 5000 RPM, oven bake @ 85 °C 25 minutes
57. Expose photoresist, 40 seconds, mask #2
58. Develop using a three puddle method (60, 60 and 90 seconds) with Eagle 2005 developer, hard bake @ 115 °C 60 seconds
59. Plasma etch $TaSi_2$, 25 sccm SF_6, 75 sccm C_2ClF_5, 150 mTorr, 25 °C, 400 Watts
60. P-strip negative photoresist, 5:1 H_2SO_4 : H_2O_2, 110 °C, 10 minutes
61. DI rinse, 10 minutes hot, 5 minutes cold
62. Spin dry
63. Sacrificial SOG release etch

REFERENCES

[1] K. E. Petersen. "Silicon as a Mechanical Material." *Proc. IEEE*, 70(5), 420-457, May 1982.

[2] H. C. Nathanson, W.E. Newell, R.A. Wickstrome and J.R. Davis, Jr., "The Resonant Gate Transistor." *IEEE Trans. on Electron Devices*, ED-14(4):117-133, 1967.

[3] R. S. Muller. "From ICs to Microstructures : Materials and Technologies." *In Proceedings of the IEEE Micro Robots and Teleoperators Workshop*, Hyannis, MA, November 9-11, 1987.

[4] K. E. Bean. "Anisotropic Etching of Silicon." *IEEE Trans. on Electron Devices*, ED-25:1185-1193, 1978.

[5] H. Guckel and D. W. Burns. "Fabrication Techniques for Integrated Sensor Microstructures." *In Technical Digest, IEEE International Electron Devices Meeting*, pages 176-179, Los Angeles, CA, 1986.

[6] R. T. Howe. *Polycrystalline Silicon Microstructures*. In C. D. Fung, P. W. Cheung, W. H. Ko, and D. G. Fleming, editors, *Micromachining and Micropackaging of Transducers*. pages 169-187. Elsevier, New York, NY, 1985.

[7] K. Najafi, K. D. Wise, and T. Mochizuki. "A High-Yield IC-Compatible Multichannel Recording Array." *IEEE Trans. on Electron Devices*, ED-32:1206-1211, 1985.

[8] H. Tanigawa, T. Ishihara, M. Hirata, and K. Suzuki. "MOS Integrated Silicon Pressure Sensor." *IEEE Trans. on Electron Devices*, ED-32:1191-1195, 1985.

[9] W. Riethmuller, W. Benecke, U. Schnakenberg, and B. Wagner. "A smart Accelerometer with On-Chip Electronics Fabricated by a Commercial CMOS Process." *Sensors and Actuators*, A31:121-124, 1992.

[10] K. Petersen, J. Brown, T. Vermeulen, P. Barth, J. Mallon, Jr., and J. Bryzek. "Ultra-Stable High-Temperature Pressure Sensors Using Silicon Fusion Bonding." *Sensors and Actuators*, A21:96-101, 1990.

[11] B. Morten, G. De Cicco, and M. Prudenziati. "Resonant Pressure Sensor Based on Piezoelectric Properties of Ferroelectric Thick Films." *Sensors and Actuators*, A31:153-158, 1992.

[12] H. Bartelt, and H. Unzeitig. "Design and Investigation of Micromechanical Bridge Structures for an Optical Pressure Sensor with Temperature Compensation." *Sensors and Actuators*, A37-A38:167-172, 1993.

[13] P. W. Barth, F. Pourahmadi, R. Mayer, J. Poydock, and K. E. Petersen. "A Monolithic Silicon Accelerometer with Integral Air Damping and Over-Range Protection." *IEEE Solid-State Sensors and Actuators Workshop*, 35-38, Hilton Head,SC, 1988.

[14] L. M. Roylance, and J. B. Angell. "A Batch-Fabricated Silicon Accelerometer." *IEEE Trans. on Electron Devices*, ED-26:1911-1920, 1979.

[15] S. Terry. "A Miniature Silicon Accelerometer with Built-In Damping." in *Technical Digest of IEEE Conference Solid-State Sensors and Actuators*, 114-116, Hilton Head, SC, 1988.

[16] Endevco General Catalog, Accelerometers, 1992

[17] Motorola Catalog, Pressure Sensors, 1989.

[18] W. D. Frobenius, S. A. Zeitman, M. H. White, D. D. O'Sullivan, and R. G. Hamel. "Microminiature Ganged Threshold Accelerometers Compatible with Integrated Circuit Technology." *IEEE Trans. on Electron Devices*, ED-19(1):37-40, 1972.

[19] C. Robinson, D. Overman, R. Warner, and T. Blomquist. "Problems Encountered in the Development of a Microscale G-Switch Using Three Design Approaches." *Technical Digest, 4th Int. Conf. Solid-Stale Sensors and Actuators (Transducers '87)*:410-413, Tokyo, Japan, June 2-5, 1987.

[20] Y. Loke, G. H. McKinnon, and M. J. Brett. "Fabrication and Characterization of Silcon Micromachined Threshold Accelerometers." *Sensors and Actuators*, A29:235-240, 1991.

[21] S. P. Murarka. *Silicides for VLSI Applications*. Academic Press, New York, NY, 1983.

[22] A. Kelly. *Strong Solids*. 2nd ed. (Monographs on the Physics and Chemistry of Materials). Oxford, England, 1973.

[23] E. B. Shand. *Glass Engineering Handbook*. McGraw-Hill, New York, NY, 1958

[24] *CRC Handbook of Chemistry and Physics*. R.C. Weast, Ed., CRC Publ., Cleveland, OH, 1980

[25] G. L. Pearson, W. T. Reed, Jr., and W. L. Feldman. "Deformation and Fracture of Small Silicon Crystals." *Acta Metallurgica*, vol. 5, 181, 1957.

[26] S. Bouwstra, P. Kemna, and R. Legtenberg. "Thermally Excited Resonating Membrane Mass Flow Sensor." *Sensors and Actuators*, A20:213-224, 1989.

[27] H. Kobayashi, and Y. Hosokawa. "A Study of a Capacitance-Type Position Sensor for Automotive Use." *Sensors and Actuators*, A24:27-34, 1990

[28] M. G. Allen, M. Scheidl, R. L. Smith, and A. D. Nikolich. "Movable Micromachined Silicon Plates with Integrated Position Sensing." *Sensors and Actuators*, A21:211-214, 1990.

[29] S. G. Ferguson, and W. E. Spear. "Temperature Compensation of Amorphous Silicon Strain Gauges." *Sensors and Actuators*, A20:249-252, 1989.

[30] T. Meydan, and G. W. Healey. "Linear Variable Differential Transformer (LVDT): linear displacement transducer utilizing ferromagnetic amorphous metallic glass ribbons." *Sensors and Actuators*, A32:582-587, 1992.

[31] W. C. Tang, T. -C. H. Nguyen, M. W. Judy, and R. T. Howe. "Electrostatic-Comb Drive of Lateral Polysilicon Resonators." *Sensors and Actuators*, A21:328-331, 1990.

[32] R. Legtenberg, S. Bouwstra, and J. H. J. Fluitman. "Resonating microbridge mass flow sensor with low-temperature glass-bonded cap wafer." *Sensors and Actuators*, A27:723-730, 1991.

[33] A. Garcia-Valenzuela, and M. Tabib-Azar. "Fiber-Optic Force and Displacement Sensor Based on Speckle Detection with 0.1 nN and 0.1 Å Resolution." *Sensors and Actuators*, A36:199-208, 1993.

[34] T. A. Kwa, and R. F. Wolffenbuttel. "Optical Angular Displacement Sensor with High Resolution Integrated in Silicon." *Sensors and Actuators*, A32:591-597, 1992.

[35] J. Lammasniemi, and T. Hyvarinen. "Infrared Sensing and Analysis in Industrial Measurements." *Sensors and Actuators*, A37-A38:173-179, 1993.

[36] F. Baldini, S. Bracci, and F. Cosi. "An Extended Range Fiber-Optic pH Sensor." *Sensors and Actuators*, A37-A38:180-186, 1993.

[37] R. J. Hazelden. "Optical Torque Sensor for Automotive Steering System." *Sensors and Actuators*, A37-A38:193-197, 1993.

[38] R. F. Wolffenbuttel, and G. de Graaf. "Performance of an Integrated Silicon Colour Sensor with a Digital Output in Terms of Response to Colours in the Colour Triangle." *Sensors and Actuators*, A22:574-580, 1990.

[39] D. Arn, N. Blom, K. Dobler-Steudle, N. Graber, and H. M. Widmer. "Surface Acoustic Wave Gas Sensors: Applications in the Chemical Industry." *Sensors and Actuators*, A26:395-400, 1991.

[40] M. Lach, and H. Ermert. "An Acoustic Sensor System for Object Recognition." *Sensors and Actuators*, A26:541-548, 1991.

[41] E. S. Ikpe, G. G. Scarrott, J. P. Weight, and K. T. V. Grattan. "Development of an Ultrasonic Transducer Using Long Acoustic Waves for Flow Measurement." *Sensors and Actuators*, A37-A38:403-409, 1993.

[42] R. Schellin, and G. Hess. "A Silicon Subminiature Microphone Based on Piezoresistive Polysilicon Strain Gauges." *Sensors and Actuators*, A32:555-559, 1992.

[43] T. Seitz. "Fluxgate Sensor in Plannar Microtechnology." *Sensors and Actuators*, A22:799-802, 1990.

[44] D. B. Dimitrov. "Low-Power Single FET Frequency-Response Magnetometer." *Sensors and Actuators*, A39:45-48, 1993.

[45] R. Campesato, C. Flores, A. Passaseo, and S. Verni. "GaAs Hall Sensors Made by the MOCVD Technique." *Sensors and Actuators*, A32:651-655, 1992.

[46] P. Thureau. "New Thermal Fluxmeters Using Particular Auxiliary Walls and Zero-Balanced Methods of Measurement." *Sensors and Actuators*, A36:57-64, 1993.

[47] J. P. Herzog, P. Roth, and P. Meyrueis. "Optical Fiber Flowmeter with Temperature Correction." *Sensors and Actuators*, A25:219-226, 1991.

[48] M. Archenault, R. Fouquet, and H. Gagnaire. "Automation of an Optical Fiber Refractometer." *Sensors and Actuators*, A32:701-705, 1992.

[49] Y. Sadaoka, M. Matsuguchi, and Y. Sakai. "Optical-Fiber and Quartz Oscillator Type Gas Sensors: Humidity Detection by Nafion Film with Crystal Violet and Related Compounds." *Sensors and Actuators*, A26:489-492, 1991.

[50] F. Lopez, and J. de Frutos. "Multispectral Interference Filters and Their Applications to the Design of Compact Non-Dispersive Infrared Gas Analyzers." *Sensors and Actuators*, A37:502-506, 1993.

[51] S. Marchetti, and R. Simili. "High Speed Sensitive Thermovoltaic IR Detector." *Sensors and Actuators*, A32:389-392, 1992.

[52] J. Kothe, and W. von Munch. "A UV-Sensitive CCD Detector Array Based on Charge-Induced Depletion Layer." *Sensors and Actuators*, A32:470-475, 1992.

[53] A. W. van Herwaarden, D. C. van Duyn, B. W. van Oudheusden, and P. M. Sarro. "Integrated Thermopile Sensors." *Sensors and Actuators*, A22:621-630, 1990.

[54] A. Kolling, F. Bak, P. Bergveld, and E. Seevinck. "Design of a CMOS Temperature Sensor with Current Output." *Sensors and Actuators*, A22:645-649, 1990.

[55] T. Boltshauser, and H. Baltes. "Capacitive Humidity Sensors in SACMOS Technology with Moisture Absorbing Photosensitive Polyimide." *Sensors and Actuators*, A26:509-514, 1991.

[56] S. J. Martin, A. J. Ricco, T. M. Niemczyk, and G. C. Frye. "Characterization of SH Acoustic Plate Mode Liquid Sensors." *Sensors and Actuators*, A20:253-268, 1989.

[57] Duk-Dong Lee, and Wan-Young Chung. "Gas-Sensing Characteristics of SnO_{2-x} Thin Film with Added Pt Fabricated by the Dipping method." *Sensors and Actuators*, A20:301-306, 1989.

[58] H. Perrot, N. Jaffrezic-Renault, N. F. de Rooij, and H. H. van den Vlekkert. "Ionic Detection Using Differential Measurement between an Ion-Sensitive FET and a Reference FET." *Sensors and Actuators*, A20:293-300, 1989.

[59] M. Mehregany, S. F. Bart, L. S. Tavrow, J. H. Lang, S. D. Senturia, and M. F. Schlecht. "A Study of Three Microfabricated Variable-Capacitance Motors." *Sensors and Actuators*, A21:173-179, 1990.

[60] L. S. Fan, Y. C. Tai, and R. S. Muller. "IC-Processed Electrostatic Micro-Motors." *In 1988 IEEE Int. Electron Devices Meeting*, pages 666-669, San Francisco, CA, December 11-14, 1988.

[61] N. Nakajima, K. Ogawa, and I. Fujimasa. "Study on Microengines: Miniaturizing Sterling Engines for Actuators." *Sensors and Actuators*, A20:75-82, 1989.

[62] C. -J. Kim, A. P. Pisano, R. S. Muller. "Polysilicon Microgripper." *Sensors and Actuators*, A33:221-228, 1992.

[63] K. S. J. Pister, M. W. Judy, S. R. Burgett, and R. S. Fearing. "Microfabricated Hinges." *Sensors and Actuators*, A33:249-256, 1992.

[64] E. Stemme, and G. Stemme. "A valveless Diffuser/Nozzle-Based Fluid Pump." *Sensors and Actuators*, A33:221-228, 1992.

[65] H. -P. Trah, H. Baumann, C. Doring, H. Goebel, T. Grauer, and M. Mettner. "Micromachined Valve with Hydraulically Activated Membrane Subsequent to a Thermoelectrically Controlled Bimorph Cantilever." *Sensors and Actuators*, A39:169-176, 1993.

[66] M. Esashi. "Integrated Micro Flow Control Systems." *Sensors and Actuators*, A21:161-167, 1990.

[67] J. A. Walker, K. J. Gabriel, and M. Mehregany. "Thin-Film Processing of TiNi Shape Memory Alloy." *Sensors and Actuators*, A21:243-246, 1990.

[68] P. A. Neukomm, H. P. Bornhauser, T. Hochuli, R. Paravicini, and G. Schwarz. "Characteristics of Thin-Wire Shape Memory Actuators." *Sensors and Actuators*, A21:247-252, 1990.

[69] F. Rudolph. "A Micromechanical Capacitive Accelerometer with a Two-Point Inertial-Mass Suspension." *Sensors and Actuators*, vol. 4:191-198, 1983.

[70] R. Dell Acqua. "A Bright Future for Thick Film Sensor." *SAE Conference*, 1989, Feb. 27-Mar. 2, Detroit, MI, 1982.

[71] P. L. Chen, R. S. Muller, and A. P. Andrew. "Integrated Silicon PI-FET Accelerometer with Proof Mass." *Sensors and Actuators*, vol. 5:119-126, 1984.

[72] P. Kaufman. "Force Balance Accelerometer for Cost-Sensitive Application." *Sensors*, June:19-21, 1988

[73] G. Delapierre, J. S. Danel, F. Michel, J. L. Bost, A. Boura, and O. Aujay. "A Quartz Micro-Machined Closed Loop Accelerometer." *Proc. Eurosensors '87*, 223-224 Cambridge, U.K., Sept. 22-24, 1987.

[74] B. Sukhov, and M. Lazarou. "Solid State Silicon Servo Accelerometer." *Proc. Int. Electrical Electronics Conference*, vol. 2:312-313, Ontario, Canada, Sept. 26-28, 1983.

[75] D. W. Satchell, and J. C. Greenwood. "A Thermally Excited Silicon Accelerometer." *Sensors and Actuators*, vol. 17:241-245, 1989.

[76] G. A. MacDonald. "A Review of Low Cost Accelerometer for Vehicle Dynamics." *Sensors and Actuators*, A21-A23:303-307, 1990.

[77] S. Timoshenko, and D. H. Young. *Elements of Strength of Materials*. D. Van Nostrand Company, Inc., New York, NY, 5th edn., p. 216, 1968.

[78] S. Timoshenko, and D. H. Young. *Elements of Strength of Materials*. D. Van Nostrand Company, Inc., New York, NY, 5th edn., p. 358, 1968.

[79] M. A. Plonus. *Applied Electromagnetics*. McGraw-Hill, New York, NY, Ch. 5, pp. 186-188, 1978

[80] L. -S. Fan. "Integrated Micromachinery: Moving Structures on Silicon Chips." PhD Thesis. University of California, Berkeley, CA, 1989.

[81] R. T. Howe. "Resonant Microsensors." 4th International Conference on Solid-State Sensors and Actuators, pp. 843-848 Tokyo, Japan, 1987.

[82] R. T. Howe, and R. S. Muller. "Polycrystalline Silicon Microstructures." J. Electrochem. Soc., 130:1420-1423, 1983.

[83] S. M. Sze, Editor. "VLSI Technology." McGraw-Hill Book Company, New York, NY, 1983.

[84] Y. C. Tai. *IC Processed Polysilicon Micromechanics: Technology, Material, and Devices*. PhD Thesis, University of California, Berkeley, CA, 1989.

[85] L. Y. Chen, Z. L. Zhang, J. J. Yao, D. C. Thomas, and N. C. MacDonald. "Selective Chemical Vapor Deposition of Tungsten for Microdynamic Structures." *In Processing of the IEEE Micro Electro Mechanical Systems Workshop*, pp. 82-87, Salt Lake City, UT, February 20-22, 1989.

[86] R. B. Brown, M. -L. Ger, and T. Nguyen. "Characterization of Molybdenum Thin Films for Micromechanical Structures." *In Proceedings of the 3rd IEEE Workshop on Micro Electro Mechanical Systems*, pp. 77-81, Napa Valley, CA, 1990.

[87] K. Hjort, J. -A. Schweitz, and B. Hok. "Bulk and Surface Micromachining of GaAs Structures." *In Proceedings of the 3rd IEEE Workshop on Micro Electro Mechanical Systems*, pp. 73-76, Napa Valley, CA, 1990.

[88] S. P. Murarka. *Silicides for VLSI Applications*. Academic Press, New York, NY, p. 98, 1983.

[89] H. Moissan. *The Electric Furnace*. (English trans. by A. de Mouilpied), Edward Arnold, London, England, 1904.

[90] R. Wehrmann. in *High-Temperature Materials and Technology*. Edited by I. E. Campbell and E. M. Sherwood, p. 399, Wiley, New York, NY, 1967.

[91] B. Aronsson, T. Lundstrom, and S. Rundqvist. *Borides, Silicides and Phosphides*. Wiley, New York, NY, 1965.

[92] A. C. Adams. *Dielectric and Polysilicon Film Deposition*. edited by S. M. Sze in *VLSI Technology*. p. 93, McGraw-Hill, New York, NY, 1983

[93] S. P. Murarka. *Silicides for VLSI Applications*. Academic Press, New York, NY, p. 136, 1983.

[94] S. P. Murarka, M. H. Read, C. J. Doherty, and D. B. Fraser. "Resistivities of Thin Film Transition Metal Silicides." *J. Electrochem. Soc.* 129:293, 1982.

[95] S. P. Murarka. *Silicides for VLSI Applications*. Academic Press, New York, NY, p. 30, 1983.

[96] T. Hara, and M. Murota. "Interfacial Reaction of Ta- and Si-rich Tantalum Silicides with Si Substrate." *J. Appl. Phys.* 68(1):183-188, 1990.

[97] S. P. Murarka. *Silicides for VLSI Applications*. Academic Press, New York, NY, p. 48, 1983.

[98] W. C. Oliver, R. Hutchings, and J. B. Pethica. in *ASTM STP 889* edited by P. J. Blau and B. R. Lawn, *American Society for Testing and Materials*, pp. 90-108, Philadelphia, PA, 1986.

[99] J. B. Pethica. in *Ion Implantation into Metals*. edited by V. Ashworth, W. Grant, and R. Procter, Pergamon Press, Oxford, England, pp. 147-156, 1982.

[100] I. E. Sneddon. "The Relation between Load and Penetration in the Axisymmetric Boussinesq Problem for a Punch of Arbitrary Profile." *Int. J. Eng. Sci.*, 3, 47, 1965.

[101] W. C. Oliver, and G. M. Pharr. "An Improved Technique for Determining Hardness and Elastic Modulus Using Load and Displacement Sensing Indentation Experiments." *J. Mater. Res.*, Vol. 7, No. 6, pp. 1564-1583, 1992.

[102] S. M. Sze, Editor. *VLSI Technology*. McGraw-Hill Book Company, New York, NY, p. 121, 1983.

[103] S. M. Sze, Editor. *VLSI Technology*. McGraw-Hill Book Company, New York, NY, p. 116, 1983.

[104] S. M. Sze, Editor. *VLSI Technology*. McGraw-Hill Book Company, New York, NY, p. 120, 1983.

[105] Shipley Company, Inc., Newton, MA., " User's Manual for Eagle NT-90 and NT-90C Photoresist.", 1991.

[106] Shipley Company, Inc., Newton, MA., " User's Manual for Eagle 2005 Developer.", 1991.

[107] Allied Signal Inc., Milpitas, CA., "Accuglass 512 Spin-On-Glass (SOG) Product Bulletin.", April 1991.

[108] S. K. Ghandhi. *VLSI Fabrication Principles*. John Wiley and Sons, New York, NY, p. 446, 1983.

[109] S. P. Murarka. *Silicides for VLSI Applications*. Academic Press, New York, NY, p. 5, 1983.